ALL-PARTICLE MULTISCALE COMPUTATION OF HYPERSONIC RAREFIED FLOW

by

Eun Ji Jun

A dissertation submitted in partial fulfillment
of the requirements for the degree of
Doctor of Philosophy
(Aerospace Engineering)
in The University of Michigan
2012

Doctoral Committee:

Professor Iain D. Boyd, Chair
Professor Michael R. Combi
Professor Elaine S. Oran
Professor Kenneth G. Powell

To my parents

ACKNOWLEDGEMENTS

Dream but always be awake.

It has been a long journey. My vague dream turned into reality and it would not have been possible without the help and support of the people around me. I would like to take this opportunity to thank all.

First of all, I would like to thank Professor Boyd for his endless endurance, support and belief through all these years. He was not only a supervisor, but also a mentor, supporter and teacher. I must be one of the luckiest students who were able to have him as one's supervisor. I cannot imagine myself being here without his guidance and encouragement. There are some times that the word "thank you" would not be enough, and this is the very moment, but I cannot find any better words. I also deeply appreciate the time, dedication and valuable advices from the rest of my thesis committee, Prof. Oran, Prof. Powell and Prof. Combi. I would also like to thank Dr. Burt for his help and suggestionse. I also like to express my gratitude to our group members in the Nonequilibrium Gas and Plasma Dynamics Laboratory (NGPDL).

I am so sorry that it is not possible to list everyone, but I cannot help to mention the friends here in Ann arbor who shared the up and down times with me, especially Jiwon, Eunjung, Jaeheon, Yongjun. Also to all the other friends who have never stopped to believe in me though we were not able to share the moments here. Lastly and mostly, I would give all the thanks to my parents who have inspired from very beginning. Special thanks to my younger brother, Jaemin.

Financial support for my graduation studies came from NASA grant NNX08AD02A. This support is greatly appreciated.

Every end goes to the next beginning. My school days are finally ended, and it is time to go to the real world where another story is waiting.

TABLE OF CONTENTS

LIST OF FIGURES

Figure

LIST OF TABLES

Table

LIST OF NOMENCLATURE

Acronyms

CFD	Computational Fluid Dynamics
CFL	Courant-Friedrichs-Lewy
DSMC	Direct Simulation Monte Carlo
EDL	Entry, Descent, and Landing
LD	Low Diffusion
LeMans	The Michigan Aerothermodynamics Navier-Stokes solver
NTC	No-Time-Counter
MD	Molecular Dynamics
MONACO	A DSMC code developed at the University of Michigan
MPF	Mars Path Finder
MSL	Mars Science Laboratory
NASA	National Aeronautics and Space Administration
NS	Navier-Stokes
RGD	Rarefied Gas Dynamics
VHS	Variable Hard Sphere
VSS	Variable Soft Sphere

Latin Symbols

A_j	the corresponding Eulerian face area
C_D	the drag coefficient
C_H	the heat coefficient
D	the total drag
D_{cell}	the mixture diffusion coefficient
E	the energy
$\mathbf{F}$	the external force per unit mass
Kn	the Knudsen number
Kn_{GLL}	the gradient-length local Knudsen number
Ma	the Mach number
M	the momentum
N_c	the number of particle pairs in the cell

N_d	the desired number of particles per cell
N_p	the number of particles per cell
N_f	the number of interior faces
N_{sub}	the number of subcycle in the LD algorithm
N_t	the iteration of computation
P	the pressure
P_c	the probability of collisions for each pair
P_{rot}	the probability of rotational energy exchange
P_{vib}	the probability of vibrational energy exchange
Q	some flow quantities of interest such as density, pressure, temperature.
R_u	the universal gas constant
S	the area
T	the temperature
$\vec{U}$	the particle velocity vector
V_{cell}	the computational cell volume
W	the numerical weight
Z_{rot}	the rotational collision number
Z_{vib}	the vibrational collision number

a	the local speed of sound
c_r	the relative speed between colliding particles
$\mathbf{c}$	the molecular velocity vector $\mathbf{c}\,(v_x, v_y, v_z)$
d	the particle diameter
f	the velocity distribution function $f\,(\mathbf{r}, \mathbf{c}, t)$
g	the relative velocity of the molecules
k	the thermal conductivity
k_B	the Boltzmann's constant
l	the distance between two points in the flow field
m	the mass
n	the number density
q	the heat transfer
r_f	the refinement factor
$\mathbf{r}$	the position vector $\mathbf{r}\,(x, y, z)$
t	time
u_f	the Lagrangian cell face velocity

Greek Symbols

α	the diffusive data
β	the characteristic thermal speed
χ	the scattering angle in the VSS model
Δt	the numerical time step interval

Φ_j	the unidirectional incident normal component flux
λ	the mean free path
μ	the dynamic viscosity
ν	the collision frequency
θ_v	the characteristic temperature for vibrations
θ	the relaxation factor for DSMC buffer cell property in LD-DSMC
ρ	the mass density
σ	the collision cross section
$\sigma d\Omega$	the differential collision cross-section
ω	the viscosity temperature exponent
τ_t	the translational relaxation time
τ_{ij}	the viscous stress tensor
ζ_r	the number of rotational degree of freedom
ζ_v	the number of vibrational degree of freedom

Superscripts

$*$	refers to a cell based instantaneous value
0	refers to an initial value

Subscripts

∞	refers to a free-stream quantity
b	refers to a bulk quantity
i	refers to a particle identification
j	refers to a face index
f	refers to a face quantity
ref	refers to a reference quantity

ABSTRACT

ALL-PARTICLE MULTISCALE COMPUTATION OF HYPERSONIC RAREFIED FLOW

by

Eun Ji Jun

Chair: Iain D. Boyd

Hypersonic aerothermodynamics for a probe entering a planetary atmosphere is an important issue in space exploration. The probe experiences various Knudsen number regimes, ranging from rarefied to continuum, due to density variation in the planet's atmosphere. To simulate such multiscale flows, a novel hybrid particle scheme is employed in the present work. The hybrid particle scheme employs the direct simulation Monte Carlo (DSMC) method in rarefied flow regions and the low diffusion (LD) particle method in continuum flow regions. Numerical procedures in the low diffusion particle method are implemented within an existing DSMC algorithm.

The hybrid scheme is assessed by studying Mach 10 nitrogen flow over a sphere with a global Knudsen number of 0.002. Standard DSMC and CFD results are compared with the LD-DSMC hybrid simulation results. The hybrid scheme results show good overall agreement with results from standard DSMC computation, while CFD is inaccurate especially in the wake where a highly rarefied region exists. The LD-DSMC hybrid solution is able to increase computational efficiency by 20% in comparison to

DSMC. Also, sensitivity to numerical parameters of the LD-DSMC method is studied by using Mach 40 carbon dioxide flow over a Mars entry spacecraft. Finally, a module initializing the LD-DSMC hybrid method with a Navier-Stokes solution is studied. The conventional LD-DSMC initializes with standard DSMC until the first continuum breakdown occurs. The main alternative to hybrid LD-DSMC simulation is a CFD-DSMC hybrid simulation that is significantly faster because it initializes the method decomposition by evaluating breakdown based on an initial CFD solution. The initialized solution agrees well with DSMC and the conventional LD-DSMC methods and requires only 56 % of the resources of the conventional LD-DSMC simulation.

CHAPTER I

Introduction

1.1 Motivation

The desire of humans for space exploration was first realized through the success of Sputnik in 1957 and over 200 missions have been completed or have been planned since that time [2]. As we move into the 21st century, planetary missions, especially to the Moon and Mars, have taken center stage in planetary exploration due to the possibility of finding resources and life [35]. The most recent planetary mission is the Mars Science Laboratory (MSL), which is a robotic mission to Mars launched by NASA on November 26, 2011 that successfully landed Curiosity, a Mars rover, on August 6, 2012 [2]. Planetary missions are classified by type of approach to the destination, like orbiters, flybys, hard impactors and landers. The first successful soft landing mission was Luna 9 in 1966; many lander missions have been performed since then [1]. The most challenging part of a landing mission is the entry, descent, and landing (EDL) sequence (Figure 1.1).

To explore a planet possessing an atmosphere, most planetary missions utilize an entry vehicle. As a vehicle enters the atmosphere of a planet, a series of physical interactions ensue between the vehicle and the surrounding atmospheric gas. The vehicle enters the atmosphere at near-orbital velocity relative to the atmosphere. The velocity is much higher than the speed of sound in the atmosphere; hypersonic

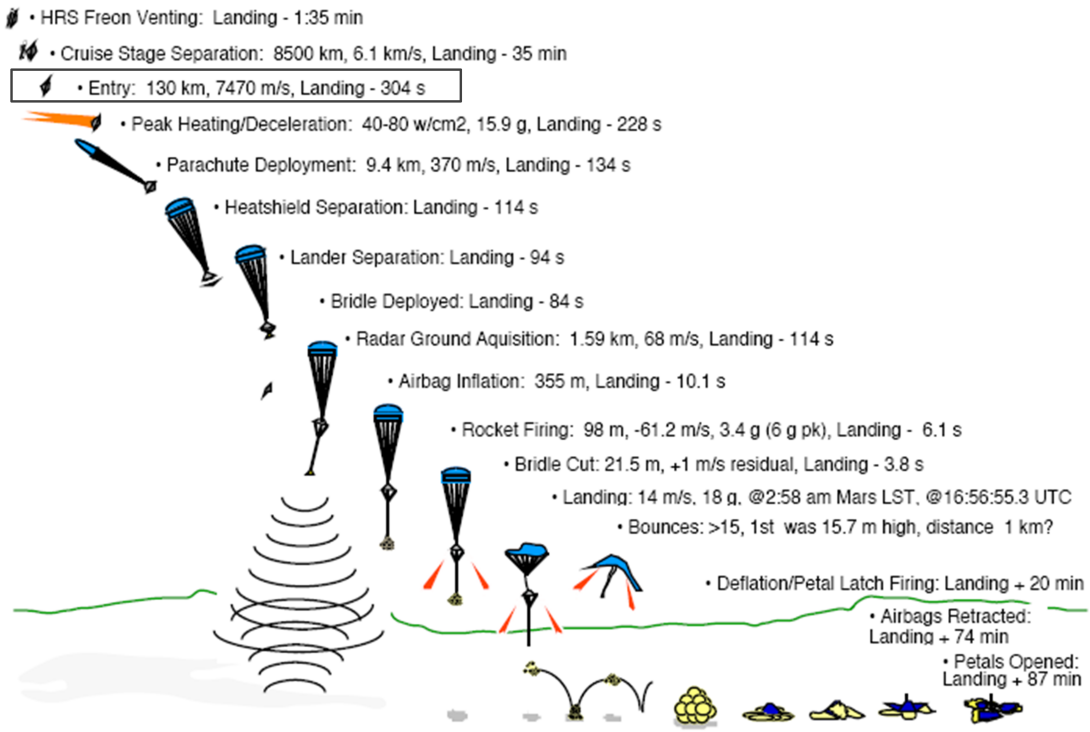

Figure 1.1: Mars Pathfinder EDL sequence of events [65].

Altitude [km]	Times [sec]	V_∞ [m/s]	ρ_∞ [kg/m^3]	Kn_∞
130.9	0.0	7460	1.18×10^{-9}	5.50×10^{1}
110.1	12.1	7470	1.84×10^{-8}	8.47×10^{-1}
90.2	24.6	7480	2.61×10^{-7}	5.98×10^{-2}
65.0	42.3	7450	7.95×10^{-6}	1.96×10^{-3}
56.1	49.3	7430	2.86×10^{-5}	5.60×10^{-4}

Table 1.1: Freestream and surface conditions for Mars pathfinder nominal entry trajectory [45, 46].

Mach numbers greater than 20 are encountered.

The conventional rule of thumb defines hypersonic flow where the free stream Mach number, Ma_∞, is greater than 5. At high Mach numbers, a strong bow shock wave is located close to the vehicle surface. The total energy crossing the bow shock of the vehicle is sufficiently large to excite internal vibrational energy, and to cause dissociation and even ionization. These high temperatures change the gas properties, so it is a dominant effect of hypersonic aerodynamics [4]. For example, the Mars Pathfinder (MPF) entry vehicle entered the Mars atmosphere directly from the interplanetary transfer trajectory with an inertial velocity magnitude of 7,460 m/s at 140 km above the surface. As the vehicle descended deeper into the atmosphere, it experienced an extreme flow condition. The vehicle reached 56 km altitude within 50 sec (Table 1.1). The maximum heat flux at the stagnation point was 20 W/cm^2 before the deployment of a parachute [46, 45]. Figure 1.2 is an illustration of the high temperature shock layer for a capsule moving at hypersonic speed. At 65 km above the Mars surface, MPF enters at about Mach 40 and the temperature rises to 46,000 K (about 8 times the surface temperature of the Sun) in the shock layer. Due to the maximum heating at the stagnation point and the significant deceleration pressure, aerodynamic analysis around an entry vehicle is a significant concern for proper design and operation.

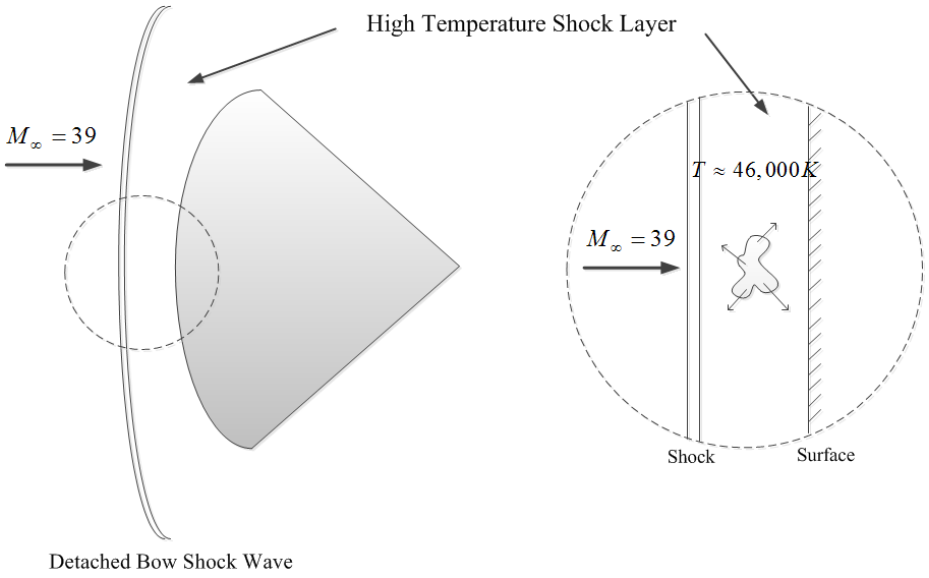

Figure 1.2: Illustration of the high-temperature shock layer on the Mars Pathfinder moving at hypersonic speed.

1.2 Flow Regime Characteristics

In the EDL sequence, the flow experiences a wide range of regimes including both high and low Knudsen number (Equation (1.1)). The flow regime may be classified as free molecular, continuum, and transitional, depending on the Knudsen number [27]. At the highest altitudes, the interaction of the vehicle with the atmosphere is characterized by free molecular flow. In the limit of very few collisions as a molecule traverses the flow field, internal energy modes and chemical composition tend to stay frozen at their initial condition. In the opposite limit of very many collisions as a molecule traverses only a small distance across the flow field, the effects of collisions at previous locations in the flow field are overwhelmed by local collisions. This limiting case is referred to as equilibrium flow; it is usually restricted to flow well within the continuum regime [27, 52]. As the vehicle descends deeper from the free molecular flow regime to the equilibrium flow, the mean free path between atmospheric molecules decreases (the gas becomes more dense). This flow condition defines the transitional regime which represents a transition from free molecular flow to contin-

uum flow. In transitional flow, aerodynamic forces and heating rates start to increase rapidly and are accompanied by chemical reactions. The reactions are the result of energetic, intermolecular collisions. These collisions also serve to distribute energy among the various internal modes (rotational, vibrational, and electronic) of the gas. This state is referred to as a nonequilibrium flow; it is usually encountered in the transition regime between free molecular flow and continuum flow [51]. In the transition regime, the increased contribution of friction force with flight altitude causes considerable changes in aerodynamic characteristics as compared to their continuum behavior. These changes affect the trajectory of the descending spacecraft very slightly during ballistic entry.

The degree of rarefaction and departure from translational thermal equilibrium of a gas is generally characterized through the Knudsen number as given in Equation (1.1) [8]. This is the ratio of the average distance the gas molecules travel between collisions, to a characteristic length-scale of the fluid system.

$$Kn = \frac{\lambda}{L} \tag{1.1}$$

where λ is the mean free path of the gas and L is a characteristic length scale. It is generally accepted that free molecule flow may be assumed for Knudsen numbers larger than 10. If the Knudsen number is much smaller than one, the flow is considered to be continuum. In this case, one can disregard microscopic structure in the gas and consider only macroscopic parameters such as density, velocity, and temperature. A sufficiently large number of collisions occur for the velocity distribution to be characterized by a small departure from equilibrium, and the conventional Navier-Stokes or Euler equations are appropriate models. The Euler equations for inviscid flow assume that the flow is in local thermodynamic equilibrium with the velocity distribution equal to the local Maxwellian. This is the limiting case as the Knudsen

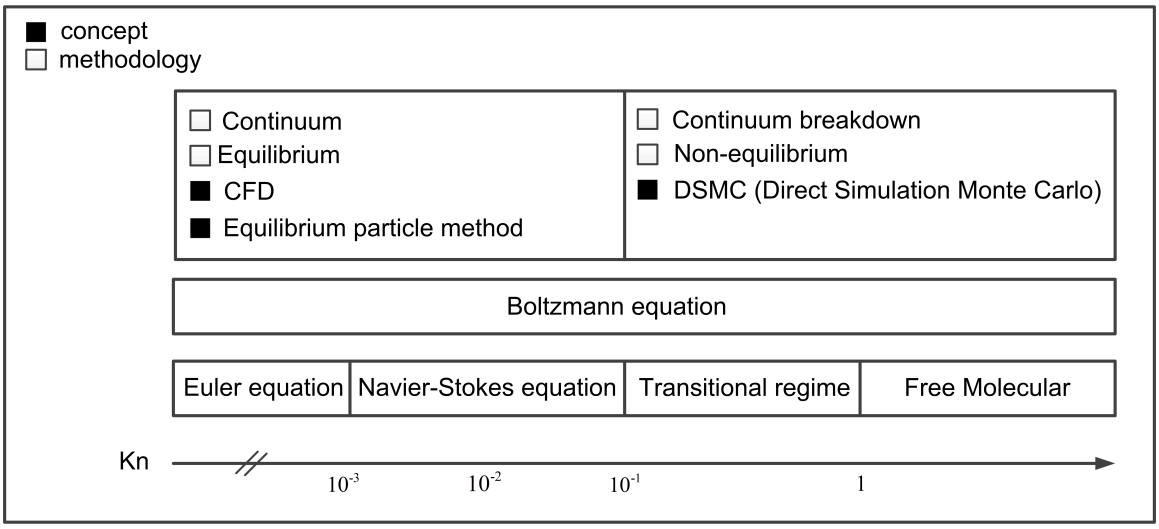

Figure 1.3: Flow regimes and characteristics according to the local Knudsen number [8, 65].

number tends to zero. Computational fluid dynamics (CFD) techniques are used to solve these equations. As the Knudsen number increases and reaches 0.1 or 0.2, the velocity distribution becomes non-Maxwellian, the continuum assumption breaks down due to insufficient collisions. The Navier-Stokes equations become inaccurate. In this regime, the flow is characterized by strong thermal non-equilibrium and the Boltzmann equation is the governing equation which requires a simulation method based on kinetic theory [8]. The most mature and commonly used simulation method for the Boltzmann equation is the direct simulation Monte Carlo (DSMC) method. The flow regimes and characteristics are explained in Figure 1.3 [8].

Even when an entry vehicle as a whole is in the continuum regime, there may exist locally rarefied regions in the hypersonic flowfield such as the interior of shock waves, wall boundary layers or wake regions. In these regions, the numbers of particles and collisions may not be enough to produce a Maxwellian distribution and an equilibrium description is inaccurate. This kind of mixed flow is called a multiscale flow. Thus, a multiscale flow that experiences a wide range of regimes includes both high and low Knudsen number. Figure 1.4 is an example of a multiscale flow. The

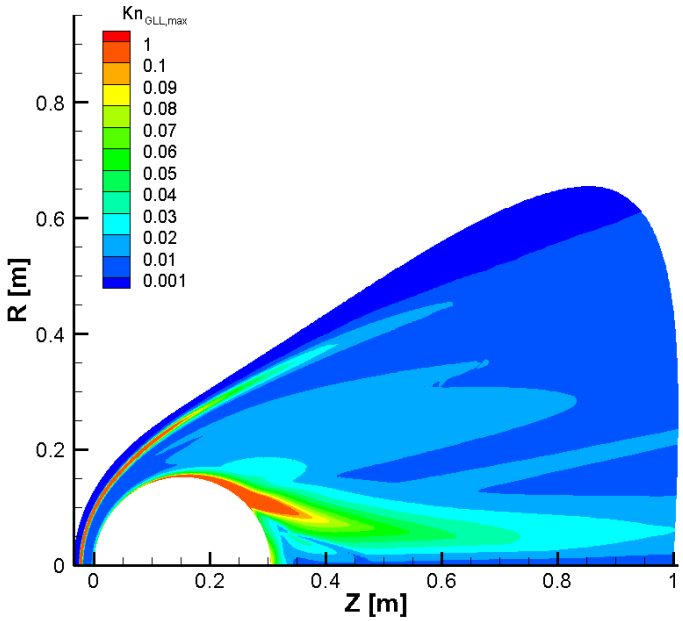

Figure 1.4: An example of multiscale flow mixed with continuum and non-continuum regions.

freestream condition is summarized in Table 5.1 and the contours in Figure 1.4 are of the maximum gradient length local Knudsen number. It shows a wide range of Kundsen number and it might be classified as continuum or non-continuum region based on the gradient-length local Knudsen number. In these types of flows, a near-equilibrium gas velocity distribution may exist through much of the flowfield, as the equilibrating effect of intermolecular collisions dominates over other processes, such as inhomogeneous diffusive transport or gas-surface interaction, which tend to pull the velocity distribution away from equilibrium. However, some flowfield regions may have characteristic length scales comparable to or smaller than the local mean free path, so that the influence of collisions does not dominate and the velocity distribution diverges considerably from the equilibrium limit. In practice, such multiscale flows are usually simulated using a hybrid scheme which includes both an equilibrium gas dynamics method and a RGD method by applying the equilibrium assumption

method in near-equilibrium regions where the Navier-Stokes equations are valid, and using a non-equilibrium method elsewhere in the flow field [36].

1.3 Review and Current Scope of Numerical Scheme

Many numerical approaches for rarefied hypersonic flow exist. For near-continuum flow, it is sufficient to take into account the effects of rarefaction through boundary conditions of slip velocity and temperature jump on the surface. Navier-Stokes equations or viscous shock layer equations are used with these conditions.

Burnett equations based on the second term of the Chapman-Enskog expansion can be used for calculating rarefied hypersonic flows. The theoretical basis of the Burnett equations is the formalism of the Chapman-Enskog expansion and the successive development for the velocity distribution function under the assumption that the particle collision time is small compared with a flow characteristic [23]. With a time-dependent, flux-splitting technique, Fiscko and Chapman found that the Burnett equations provide greater accuracy than the Navier-Stokes equations for one-dimensional shock structure in a monatomic gas [22, 26]. However, the degree of improvement over Navier-Stokes varies depending on the flow quantities of interest. Also, their application has difficulties related to the uncertainty of boundary conditions and linear instability of these equations to short-wave disturbances. The Burnett equations can only make small improvement over the Navier-Stokes equations when the latter are adequate, but the Burnett equations fail when the Navier-Stokes equations become inadequate [77, 66, 36].

If one adopts the idea that flow within shock waves falls within the range of applicability of the Boltzmann equation, then one may attempt solutions of that equation to model shock flow. One particular class of solutions to the Boltzmann equation is that obtained by the momentum method (Grad's 13-momentum equations) [24, 26]. Grad's system of 13-momentum equations is a particular set of velocity moments, the

Maxwell transfer equations in which closure is achieved with the help of an assumed form of the distribution function [23]. These equations do not require small Knudsen number, so may serve as a kinetic theory basis for a viscous shock-layer analysis. Another reason for using the 13-momentum equations is the absence of ambiguity in the type and number of admissible boundary conditions at a body surface. By considering the number of characteristics reaching the boundary, Grad showed that the number and type of needed boundary conditions are the same as for the Navier-Stokes equations [29]. For application to supersonic flows, the 13-moment equations fail to yield a normal shock structure when the free stream Mach number is larger than 1.65, as is well known [30]. Consequently, the system, without modification, cannot provide a foundation for the entire flowfield that includes the shock structure.

When considerable nonequilibrium effects exist, the Boltzmann equation can be considered directly. Direct numerical integration is an approach for numerically solving the Boltzmann equation, and the molecular dynamics (MD) method and the DSMC method model the physics of the gas flow [36, 76, 3, 8]. These will be detailed in Chapter 2.1.

Extended hydrodynamics is another method that uses equations in the form of the standard fluid equations of mass, momentum and energy, but in the momentum and energy equations the stress tensor and the heat flux vector are constructed to be mathematically more applicable to flows with a high Knudsen number [76]. This means that the expressions for the stress tensor and heat flux contain higher order, and typically nonlinear, terms in the gradients of the gas properties than the Navier-Stokes equations. One advantage of these higher-order constitutive relations is that solving them should not be much more computationally expensive than solving the standard Navier-Stokes equations. Another advantage is that the equations of extended hydrodynamics reduce to the Navier-Stokes equations in areas of low Knudsen number. Therefore, the same set of equations can be applied across an

entire mixed-density flow field [52].

To analyze multiscale flow, a hybrid method that includes an equilibrium gas dynamics method and an RGD method are needed together. Roveda et al. (1998) have used an Euler solver for those parts of the flow where an equilibrium gas description is valid and DSMC is too computationally expensive [53]. Wherever flow gradients appear in the solution, the Euler solver displayed numerical dissipation and not the correct Navier-Stokes dissipation. However, provided the Euler solver is invoked in those cells where the flow gradients are small, this is not important: the Euler equations are sufficiently accurate outside regions of large flow gradients such as boundary layers and the interior of shocks. DSMC can be used where flow gradients are large and dissipative effects must be accurately modeled [53].

In efforts to develop hybrid schemes for simulating such multiscale flows, the most widely investigated type of method is the CFD-DSMC hybrid scheme [33, 32]. In this hybrid scheme, CFD is used in the near-equilibrium regions and the direct simulation Monte Carlo (DSMC) method is applied in non-equilibrium regions where the continuum Navier-Stokes equations fail [59, 60]. Among hybrid CFD-DSMC implementations, there are two main types of approaches. In a decoupled approach, CFD calculations are applied only over near-equilibrium regions, and results from this computation are used to define inflow boundary conditions for a DSMC simulation [34]. The coupled approach is more complex and involves a number of challenges [71]. It must integrate two very different methods (CFD and DSMC) into a single numerical framework. In addition, two-way coupled information transfer between CFD and DSMC domains is complex and requires significant algorithm development. The chief difficulty with hybrid continuum/DSMC codes lies in the interface between the two approaches. Information from the continuum solver can easily serve as the boundary conditions for DSMC, but it is more difficult to use the 'noisy' information from the DSMC solution as boundary conditions for the continuum solution method. This

problem seems an inevitable result of the amalgamation of a continuum solver, for which the primitive variables are the continuum flow properties such as density and fluid velocity, and the particle-based DSMC method [61, 62].

Another type of hybrid approach for multiscale flow simulation, termed as an 'all particle' hybrid scheme, employs DSMC type particles throughout the whole simulation domain. This approach uses a particle method which is based on the DSMC in place of CFD [69, 5, 68, 38]. As in DSMC, these continuum particle methods use particles to transfer mass, momentum and energy through a computational grid, and employ temporal decoupling between particle movement and velocity resampling procedures during each simulation time step. Macroscopic flow properties are calculated in both rarefied and continuum regions by averaging quantities among representative particles. Particle velocities are typically redistributed under an assumption of local equilibrium within continuum regions. This method can handle very strong coupling between the two flow regimes. Among other advantages relative to hybrid CFD-DSMC schemes, this approach allows simpler code development, as there is no need to integrate two very different simulation schemes in the same code. However, 'all-particle' hybrid techniques are prone to significant errors associated with numerical diffusion, including effects of artificial viscosity, thermal conductivity, and mass diffusion resulting from free-molecular fluxes between adjacent cells (Figure 2.5) [41, 15, 50, 42].

This numerical diffusion is due to an extreme sensitivity to computational cell size in the equilibrium particle method. Ideally, random molecular motion in continuum flows should be suppressed on length scales comparable to the cell size because the ratio of local mean free path to cell size is typically very small. Over these macroscopic length scales, individual molecules tend to move along smooth trajectories that approximately follow the gas streamlines. In contrast, representative particles in DSMC-based continuum particle methods exhibit random motion on length scales

comparable to the cell size, so that the cell size takes on properties of the local mean free path and becomes a scaling factor for numerical transport coefficients. Because the influence of collisions is neglected in fluxes based on particle motion between adjacent cells, the ratio of numerical transport coefficients (viscosity, thermal conductivity and mass diffusivity) to physical transport coefficients tends to scale with the ratio of the mean free path to the cell size. As a result, both numerical viscosity and thermal conductivity become extremely large when the cell size is much greater that the local mean free path. To avoid this problem, a small cell size is needed, but a prohibitively large number of cells may be required to reach an overall level of simulation accuracy comparable to that of CFD methods on a much coarser grid [15, 40].

1.4 Outline of Thesis

In the present dissertation, a continuum particle method [20, 17, 16] is used as means of low Knudsen number gas flow simulation in a hybrid method. In this method, originally the intended for simulating gas flows near the low Knudsen number limit, a large number of representative particles are tracked through a grid in such a way that every particle maintains a constant relative position within a network of Lagrangian cells. Each Lagrangian cell coincides with a cell in the fixed Eulerian grid at the beginning of each time step, and moves and deforms over the time step interval according to local bulk gas properties. Particles follow the macroscopic motion of Lagrangian cells, and move along trajectories that closely approximate the gas streamlines. Random particle motion associated with thermal energy is therefore greatly suppressed. As a result, numerical diffusion errors, as well as effects of statistical scatter, are generally far smaller than in other equilibrium particle methods. The method employed here significantly reduces both numerical diffusion effects and statistical scatter relative to existing DSMC-based continuum particle methods, and is termed the low diffusion (LD) method.

Chapter II details the microscopic level behavior of gas flow. The Boltzmann equation is provided to describe flows at the microscopic level as the governing equation. The equation is detailed and challenges which are associated with deterministic solution are discussed. After the mathematical description of the Boltzmann equation, numerical methods which are based on the simulation of the physics of the flow provided by kinetic theory are discussed. In Chapter II, two kinds of particle descriptions are discussed. First, the DSMC approach is described for particle description of nonequilibrium gas dynamics. The DSMC method employs simulated molecules; their number is reduced to a manageable level by regarding each simulated molecule as representing a fixed number of real molecules. Other computation approximations, and procedures of DSMC, and physical models of DSMC, are discussed. Chapter II then describes a particle approach for an equilibrium gas: the LD method. The LD method also employs simulated molecules over the computational domain which is divided into a large number of grid cells, but it undergoes an alternative procedure in place of DSMC particle collisions. The alternative procedure of the LD method is also detailed.

Chapter III details the all-particle multiscale computation: the LD-DSMC hybrid method. The LD-DSMC hybrid method employs the DSMC method in the nonequilibrium region and the LD method in the equilibrium region. To employ both LD and DSMC methods as part of a hybrid scheme, it is necessary to determine continuum breakdown to allocate cells to LD and DSMC domains and information must to be transferred across the domain boundaries. These two key components of the LD-DSMC hybrid algorithm are outlined. The LD method needs to have physical models that are consistent with DSMC and must minimize information loss across domain boundaries. Viscous modification, internal energy nonequilibrium, and diffusive transport in the LD method are detailed in Chapter III. Finally, an effort to increase efficiency of the LD-DSMC hybrid method is described. To optimize the

constraint of DSMC, and to increase the LD-DSMC hybrid simulation efficiency, a subcell utility, and numerical weight and timestep adaptation are discussed.

The idea to increase efficiency of the LD-DSMC hybrid simulation is discussed further in Chapter IV. Previous LD-DSMC hybrid simulations have been initialized with standard DSMC until a first continuum breakdown surface is evaluated. After the first continuum breakdown, the computational domain is decomposed into LD and DSMC regions, and then the hybrid simulation starts. The main alternative to the hybrid LD-DSMC simulation is a CFD-DSMC hybrid simulation that is significantly faster because it initializes the method decomposition and flowfield based on an initial CFD solution. Based on the ideas of CFD-DSMC, the LD-DSMC hybrid method is initialized with a Navier-Stokes solution to improve the efficiency. From the CFD solution, the domain is decomposed into LD and DSMC regions. The LD-DSMC method uses the LD method in continuum regions and the DSMC method in non-continuum regions from the startup of the hybrid simulation. The details of initial domain decomposition and mesh refinement are discussed in Chapter IV.

Chapter V describes application of the LD-DSMC hybrid numerical method to several hypersonic flows. Hypersonic flow over a sphere is simulated using standard DSMC, CFD, and the LD-DSMC hybrid method. Hybrid results for flowfield and surface properties are compared with standard DSMC as well as the CFD solution. The computational efficiency of the hybrid method for this hypersonic flow is presented and discussed. Chapter V then describes application of the hybrid method to a hypersonic flow over the Mars Pathfinder. The LD-DSMC hybrid method is sensitive to numerical parameters for the assignment of LD/DSMC domains, and for determination of time step size. This sensitivity to numerical parameters is studied through the hypersonic flow over the Mars Pathfinder. Finally, in Chapter V, LD-DSMC initialized with a Navier-Stokes solution is validated for hypersonic flow over the sphere. The results are compared with the conventional LD-DSMC hybrid

method, and computational efficiency is discussed.

Chapter VI summarizes all conclusions drawn from each chapter and highlights major contributions made by this dissertation to the field of all particle multiscale computation of hypersonic rarefied flow. The chapter and thesis end with discussion for future research in the field.

CHAPTER II

Mathematical and Numerical Modeling of Gas Flow

A macroscopic model describes the flow in terms of spatial and temporal variations of the familiar flow properties such as the velocity, density, pressure, and temperature. The macropic model assumes the system is in equilibrium, which means the flow is continuous. The Navier-Stokes equations provide the conventional mathematical model of a gas as a continuum. The macroscopic view does not sufficiently describe rarefied flow (non-equilibrium flow) where the equilibrium assumption has essentially broken down and the Navier-Stokes equations become inappropriate [8]. To take into account the rarefaction effects, a view at the microscopic level is needed. In the microscopic view, the flow consists of myriad discrete atoms or molecules, and they exchange energies according to the molecular collisions. The flow at the microscopic level is governed by the Boltzmann equation which describes the flow in all regimes from free molecular to continuum [6]. In this chapter, the mathematical background of the Boltzmann equation is explained, and particle descriptions for both nonequilibrium and equilibrium gases are discussed. DSMC and LD methods are used as the nonequilibrium, and equilibrium particle descriptions, respectively.

2.1 Boltzmann Equation of Kinetic Thoery

The fundamental kinetic equation, which describes gas flows in all regimes including both equilibrium and non-equilibrium, is the Boltzmann equation (Figure 1.3). It is a nonlinear integral-differential equation which describes the statistical distribution of particles in the flow [70]. The Boltzmann equation for a simple dilute gas is

$$\frac{\partial (nf)}{\partial t} + \mathbf{c} \cdot \frac{\partial (nf)}{\partial \mathbf{r}} + \mathbf{F} \cdot \frac{\partial (nf)}{\partial \mathbf{c}} = \int_{-\infty}^{\infty} \int_{0}^{4\pi} n^2 (f^* f_1^* - f f_1) c_r \sigma d\Omega d\mathbf{c}_1 \qquad (2.1)$$

where nf is the product of number density, n, and the velocity distribution function, f. This is a probability distribution function that represents the probability that a particle located at a certain spatial position has a certain velocity at a certain point in time. In this equation, $\mathbf{c}$ is the molecular velocity, c_r is, the the relative molecular speed, $\mathbf{F}$ is, the external force per unit mass, the superscript $*$ indicates post-collision values, f and f_1 represent the distribution functions of two different types of molecules of class $\mathbf{c}$ and $\mathbf{c}_1$, respectively, t represents time, $\mathbf{r}$ the physical space, and $\sigma d\Omega$ represents the differential cross-section of the colliding particles [49]. Physically, the Boltzmann equation shows that the rate of change of the number of molecules in a unit element is due to particle movements and collisions. The collision term, on the right-hand side of the equation, is the source of problems in finding a solution. The significance of intermolecular collisions in transitional flow prevents the simplification of the Boltzmann equation by elimination of collision terms. This leaves the full equation to be solved [8].

Even though nf is the only dependent variable, there is no possibility of obtaining general analytical solutions of the Boltzmann equation due to the velocity-space coordinate as the independent variables. The Chapman-Enskog method provides an analytical solution of the Boltzmann equation but, nonetheless, it is restricted to a set of problems in which the distribution function is perturbed by a small amount from

the equilibrium Maxwellian form [8]. While analytical solutions are almost invariably based directly on the Boltzmann equation with strong assumptions, the Boltzmann equation may be solved in general by numerical methods. Numerical methods are based directly on the simulation of the physics of the flow provided by kinetic theory. Numerical methods may be divided into those: 1) take the Boltzmann equation as the starting point, and 2) are based directly on the molecular description provided by kinetic theory [49]. The Boltzmann equation is the starting point in the method of direct numerical integration [76]. It integrates the differential portion of the Boltzmann equation, which is the left side of Equation (2.1), and evaluates the collision term, the right side of Equation (2.1). Direct simulation methods do not solve the Boltzmann equation but rather model the physics of the gas flow. In these methods, the gas is considered as a collection of molecules, and representative samples of molecules are tracked throughout a time period in which molecules collide with each other. The most typical direct simulations are the molecular dynamics (MD) method and the direct simulation Monte Carlo (DSMC) technique [3, 8].

MD is the name given to the method introduced by Alder and Wainwright (1958) [3]. In MD, an initial configuration of molecules is set, and the collisions are deterministic. That is, the trajectory of molecules are computed and intermolecular collisions occur when two trajectories converge to the molecular diameter. For each trajectory, all other molecules are examined as possible collision partners. In DSMC, on the other hand, the collision computations are probabilistic, so relative positions do not affect the collision parameters within each computational cell. DSMC has been found to be less computationally intensive and can be applied to a large number of flow situations. At present, the DSMC method is mainly used for solving rarefied gas dynamics [8, 36].

2.2 Particle Description of Nonequilibrium Gas: The Direct Simulation Monte Carlo Method

In non-equilibrium flow, a gas is completely described by the position, velocity and internal state of every molecule at a particular instant. However, the number of molecules in a real gas is so large that such a description is unthinkable. So, we can use the DSMC method which resorts to a statistical description in terms of probability distributions. The DSMC approach is related to the Boltzmann equation by its restriction to binary collisions in every cell and the treatment of these collisions as instantaneous events [63].

2.2.1 Computational Approximations

The DSMC method employs simulated molecules of correct physical size and their number is reduced to a manageable level by regarding each simulated molecule as representing a fixed number of real molecules. The ratio of the number of real molecules to the number of simulated molecules is called the particle weight. Since, statistical scatter is inversely proportional to the square root of the sample size, each cell should have around 20 particles to reduce statistical scatter [9].

The velocity, position and internal states of simulated molecules are stored and updated with collisions and boundary interactions. The primary approximation of the DSMC method is to decouple the molecular motions which are modeled deterministically, and the intermolecular collisions, which are modeled probabilistically, over time intervals. To decouple accurately, the time step should be less than the mean collision time. If the time step is too large, the molecules will be able to move too far without the opportunity to participate in collisions. This will cause a 'smearing' of properties of the flow, resulting in non-physical results [49, 8].

The whole computational domain in DSMC is sub-divided into cells. Cells are

needed to define the geometry of the body in question, to identify molecular collision partners, and to sample macroscopic quantities used to generate a solution. In the collision process model, the particles within the same cell are allowed to interact, which means they are candidates for collision pairs. The size of the flow field cells are related to the mean free path of the local gas. If molecules which are separated by distances much larger than the mean free path are allowed to collide, it results in a nonphysical transfer of mass, momentum, and energy.

2.2.2 Procedure of DSMC

The DSMC algorithm consists of several primary processes: collisionless movement of particles over the timestep, application of boundary conditions, sorting particles into cells, calculation of collisions, and sampling average particle information for macroscopic flow quantities (Figure 2.1). The fundamental principle of the DSMC method is the splitting of continuous motions and collisions of molecules into two sequential stages: free molecular translation and intermolecular collisions. It corresponds to the solution of the Boltzmann equation (2.1) using the following splitting scheme within the short time-step [54]:

$$\frac{\partial (nf)}{\partial t} + \mathbf{c} \cdot \frac{\partial (nf)}{\partial \mathbf{r}} + \mathbf{F} \cdot \frac{\partial (nf)}{\partial \mathbf{c}} = 0 \tag{2.2}$$

for the collisionless movement of molecules in the first step of the DSMC algorithm, and

$$\frac{\partial (nf)}{\partial t} = \int_{-\infty}^{\infty} \int_{0}^{4\pi} n^2 (f^* f_1^* - f f_1) c_r \sigma d\Omega d\mathbf{c}_1 \tag{2.3}$$

corresponds to the molecular collisions in the third step of the DSMC algorithm.

In the first process, all the molecules are moved through distances appropriate to their velocity components and the discrete time step. Appropriate action is taken if the molecules meet the boundaries: new particles are introduced at inflow bound-

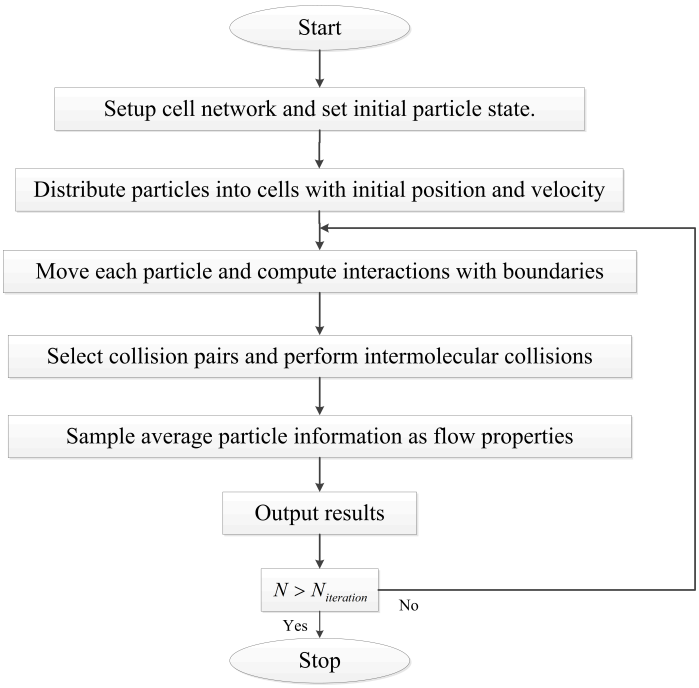

Figure 2.1: DSMC flowchart [75].

aries, particles are removed at outflow boundaries, and particles are reflected at solid boundaries.

In simulating the collisions, a probabilistic process that sets DSMC apart from deterministic simulation methods is used. The probability of a collision between two molecules is proportional to the product of their relative speed and total collision cross-section. The maximum value of the product is calculated for each cell and recorded. The collision pair is then chosen by the 'acceptance-rejection' method; the probability of a particular pair being chosen depends on the ratio of their product to the maximum product. Bird's No Time Counter (NTC) scheme is the most widely used collision scheme [8]. In the scheme, a number of particle pairs in each cell, N_c, are formed, given by:

$$N_c = \frac{1}{2} n \bar{N} \left(\sigma g\right)_{max} \Delta t \tag{2.4}$$

where n is the number density, $\bar{N}$ is the average number of particles in the cell, σ is the collision cross section, and g is the relative velocity. Each of the N_c pairs of

particles is formed at random regardless of position, and then a probability of collision for each pair, P_c, is evaluated using [12]:

$$P_c = \frac{\sigma g}{(\sigma g)_{max}} \tag{2.5}$$

Using a set of randomly generated numbers, every collision pair in a cell is assigned a number. The collision probability is then compared to this random number. If the probability, P_c, is greater than the number, the collision pair is accepted. If the probability, P_c, is less, the molecules will not collide. When a collision occurs, post-collision velocities are calculated using conservation of momentum and energy [8].

The final process is sampling the macroscopic flow properties [6]. The properties of molecules in a particular cell are used to calculate macroscopic quantities. For example, the average mass density, ρ, in a computational cell volume V_{cell} is given by

$$\rho = \frac{\sum_{i=1}^{N_p} m_i}{\mathrm{V}_{cell} \times N_t} \tag{2.6}$$

where m_i is the mass of particle i, N_p is the number of particles that have occupied this cell over N_t iterations of the computation.

The DSMC procedures are performed every timestep. Once a simulation begins from the initial condition, a finite number of iterations are elapsed to reach a steady state. The steady state is detected using the total number of particles and collisions in the whole computation domain. If those are not changed as time goes by, the flow is regarded as having reached the steady state. After the flow reaches the steady state, the sampling procedure begins. The sampling is continued a further number of iterations in order to reduce the statistical error.

2.2.3 Physical Models of DSMC

For sufficiently low densities, the molecular spacing is large compared with the effective molecular diameter. Under these circumstances, only an extremely small proportion of space is occupied by molecules and each molecule will be moving outside the range of influence of other molecules (dilute gas). When a molecule undergoes a collision, it is likely to be a binary collision involving only one other molecule. In DSMC, the flow is handled as a dilute gas, so only elastic binary collisions are considered.

There are many models that attempt to simulate actual collision characteristics. If there is no internal energy exchange or chemical reaction, elastic binary collisions lead only to change in velocity or momentum components. A popular model is the variable hard sphere (VHS) molecular model [7]. In this model, uniform, isotropic scattering is assumed. The molecular diameter, d, is a function of the relative velocities of the molecules, g. The collision cross section, σ, which is proportional to the square of d, is a function of the molecular velocities as follows:

$$\sigma = \sigma_{ref} \left(\frac{g}{g_{ref}} \right)^{-2\omega} \tag{2.7}$$

where the subscript ref is for reference values and ω is related to the viscosity temperature exponent. The viscosity of a dilute gas increases with temperature (Equation (2.8)) [73, 8].

$$\mu = \mu_{ref} \left(\frac{T}{T_{ref}} \right)^{\omega+0.5} \tag{2.8}$$

where μ is the viscosity, and T is the temperature.

The variable soft sphere (VSS) molecular model represents an improvement over the VHS molecular model which allows collision parameters to be determined through comparison with both viscosity and diffusivity data [39]. While the VHS model assumes isotropic scattering, the VSS model considers anisotropic scattering. Therefore,

the VSS model cross section is the same as in the VHS model, but the scattering angle is calculated by Equation (2.9).

$$\chi = 2cos^{-1}\left\{\left(\frac{b}{d}^{1/\alpha}\right)\right\} \tag{2.9}$$

where α is related to diffusivity, b is a distance of closest approach, and d is the collision diameter. Notice that the VSS model is identical to VHS when $\alpha = 1$.

Figure 2.2 shows a simple concept of a diatomic molecule (two atoms) using the 'dumbbell' model. The molecule has several modes of energy. DSMC handles these various modes of energy by assigning rotational and vibrational to each particle. In the DSMC method, each mode of energy is simulated using either a classical physics approach, or quantum mechanics. All modes exchange energy through particle collisions with other particles or surfaces [4].

(a) Diatomic molecule

(b) Translational energy

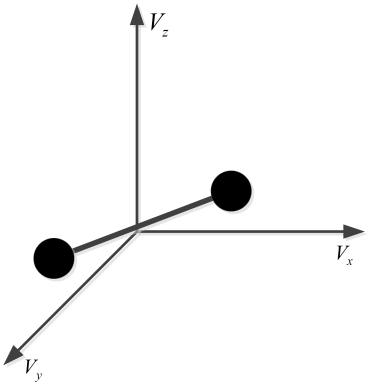

(c) Rotational energy

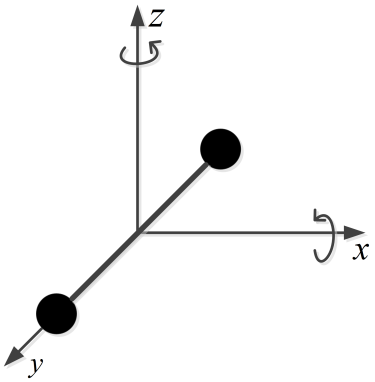

(d) Vibrational energy

Figure 2.2: Modes of molecular energy [4].

Rotational energy is associated only with di-atomic and polyatomic molecules that consist of two or more atoms. The source of the rotational energy is kinetic energy associated with the molecule's angular velocity (Figure 2.2). The energy spectrum of the rotational mode is usually assumed continuous. A particle introduced to a DSMC computational domain is assigned an initial rotational energy which is sampled from the Boltzmann distribution (Equation (2.10)) [12].

$$f\left(\epsilon_r\right) d\epsilon_r = \frac{1}{\Gamma\left(\zeta_r/2\right)} \left(\frac{\epsilon_r}{k_B T}\right)^{\zeta_r/2-1} exp\left(-\frac{\epsilon_r}{k_B T}\right) d\left(\frac{\epsilon_r}{k_B T}\right) \tag{2.10}$$

where ζ_r is the number of rotational degrees of freedom, k_B is Boltzmann's constant, and T is the temperature. Then, the rotational energy of the particle can change through collisions. The collisions that contribute to the exchange of energy are determined by a probability of rotational energy exchange, P_{rot}. It is evaluated using Equation (2.11). In the following, Z_{rot} is the rotational collision number, τ_t is the translational relaxation time that is equal to the inverse of the collision frequency, ν, and τ_r is the rotational relaxational time.

$$P_{rot} = \frac{1}{Z_{rot}} = \frac{\tau_t}{\tau_r} = \frac{1}{\tau_r \nu} \tag{2.11}$$

After evaluation of P_{rot}, acceptance-rejection is used to decide whether the collision leads to energy exchange. If P_{rot} is larger than a random number, then rotational energy exchange occurs. When a collision that induces rotational energy exchange happens, the Larsen-Borgnakke (LB) model is used to assign a new post-collision rotational energy [10]. The LB model assumes local thermodynamic equilibrium to sample the fraction of the total collision energy due to rotation, $\epsilon_{rot}/\epsilon_{tot}$, from the following expression (Equation (2.12)). In the equation, ϵ_{tot} is the total collision

energy, which is the sum of the translational collision energy and the rotational energy.

$$\frac{P}{P_{max}} = \left(\frac{\zeta_r + 1 - \omega}{2 - \omega}\left(1 - \frac{\epsilon_{rot}}{\epsilon_{tot}}\right)\right)^{2-\omega}\left(\frac{\zeta_r + 1 - \omega}{\zeta_r - 1}\left(\frac{\epsilon_{rot}}{\epsilon_{tot}}\right)\right)^{\zeta_r - 1} \tag{2.12}$$

From the $\epsilon_{rot}/\epsilon_{tot}$ ratio, a new post-collision rotational energy is assigned and the remaining energy is the new translational energy. The new translational energy determines the new post-collision relative particle velocity [12, 8].

In a high enthalpy gas, vibrational energy exchange may also take place due to collisions. The LB model can be applied to vibrational energy exchange through either a classical procedure or a quantum approach. When the vibrational energy spectrum is assumed continuous, the probability of vibrational energy exchange, P_{vib}, is in terms of vibrational collision number, Z_{vib}.

$$P_{vib} = \frac{1}{Z_{vib}} \tag{2.13}$$

Z_{vib} may be a constant or depend on energy or temperature [13, 31]. The number of vibrational degrees of freedom, ζ_v, at local temperature T, is determined for a simple harmonic oscillator as:

$$\zeta_v = \frac{2\theta_v/T}{exp\left(\theta_v/T\right) - 1} \tag{2.14}$$

where θ_v is the characteristic temperature of vibration [8]. However, real molecules are characterized by large gaps between the neighboring vibrational energy levels, so the classical assumption of the vibrational energy mode may be inaccurate.

To evaluate a collision averaged vibrational energy exchange probability, a quantum mechanical approach is employed. The vibrational energy based on the harmonic oscillator model is described as Equation (2.15) where ν is the vibrational quantum number.

$$\epsilon_\nu = \nu k_B \theta_v \tag{2.15}$$

The Boltzmann distribution for the vibrational energy level ϵ_ν is written as Equation (2.16)

$$f_{\epsilon_v} \propto exp\left(-\frac{\epsilon_v}{kT}\right)\delta\left(\epsilon_v - \nu k\theta_v\right) \tag{2.16}$$

A quantized vibrational energy exchange model for DSMC was introduced by Bergemann and Boyd [64]. The maximum vibrational quantum level in a collision is

$$\nu_{max} = \left\lfloor \frac{\epsilon_{tot}}{k\theta_v} \right\rfloor \tag{2.17}$$

where ϵ_{tot} is the total collision energy that is the sum of the translational collision energy and the vibrational energy, $\lfloor\rfloor$ means truncation, and θ_v is the characteristic temperature for vibration. Then, the postcollision vibrational level, ν, is determined from (2.18).

$$\frac{P}{P_{tot}} = \left(1 - \frac{\nu k\theta_v}{\epsilon_{tot}}\right)^{1-\omega} \tag{2.18}$$

The most important outcome from DSMC analysis of hypersonic entry flows is the determination of the properties at the vehicle surface, so a proper gas-surface interaction model is needed. The most common gas-surface interaction model used in DSMC is the fully diffuse reflection model, where a particle reflects from the surface with new velocity components that are sampled from Maxwellian distributions characterized by wall temperature. The opposite limit involves the specular reflection model, where the only change to the particle's properties is that it's velocity component normal to the surface is simply reversed in sign. Many DSMC computations use an accommodation coefficient, α, to simulate a combination of diffuse and specular reflections such that $\alpha = 1$ is fully diffuse, and $\alpha = 1$ is fully specular. Real engineering surfaces generally require a value in the range of $\alpha = 0.8 - 0.9$.

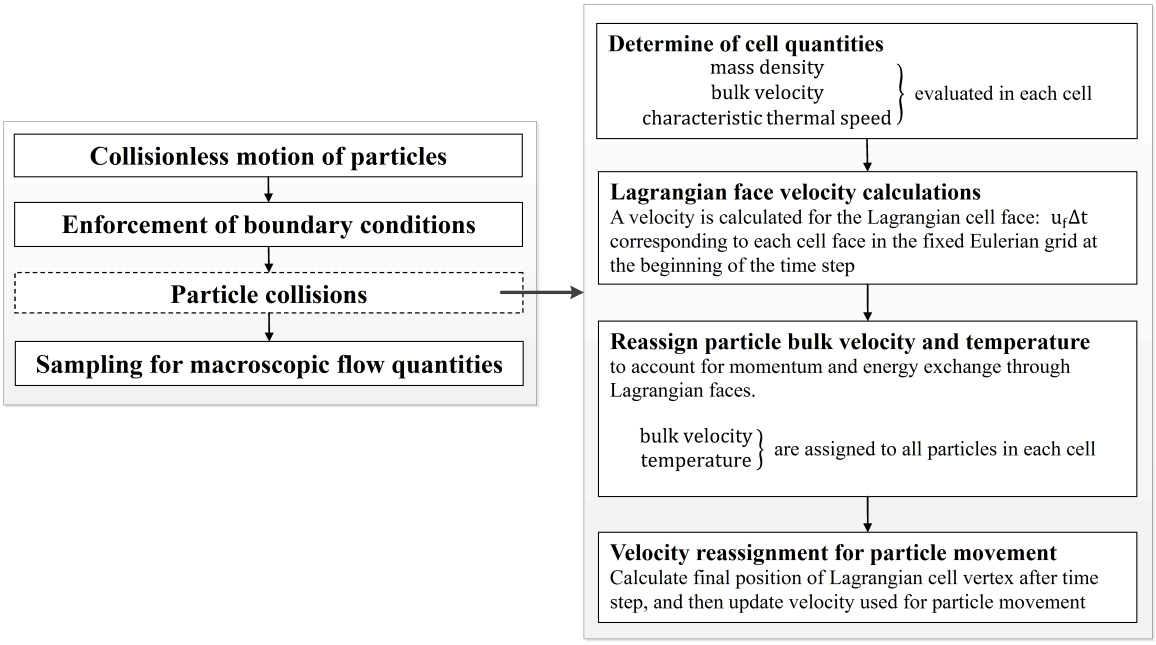

Figure 2.3: Simulation procedures performed during each time step of the LD method.

2.3 Particle Description of Equilibrium Gas: The Low Diffusion Method

A new particle technique, termed the low diffusion (LD) method, to describe equilibrium gas was developed by Burt et al [20, 17, 16]. The numerical procedures in the LD particle simulations are similar to the DSMC technique. Both LD and DSMC divide the computational domain into a large number of grid cells, and representative particles are tracked through the cells. The main difference between LD and DSMC is in dealing with the particle collisions. The LD particles undergo an alternative procedure in place of DSMC particle collisions. The alternate collision procedures enforce equilibrium velocity distributions in each cell. This approach is summarized in Figure 2.3.

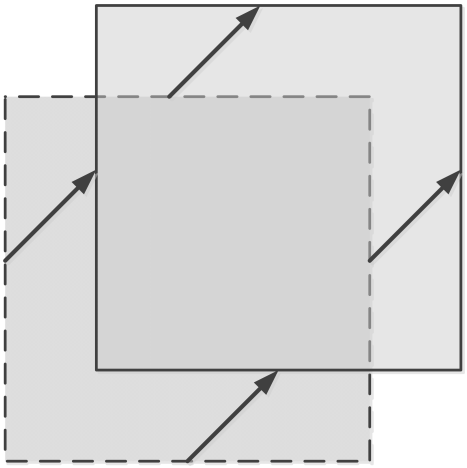

Figure 2.4: Example of change of the Lagrangian cell at the beginning and end of a single time step.

2.3.1 Lagrangian Cell

The LD method simulates the flow as a collection of continuous, finite volume, equilibrium reservoirs, represented by Lagrangian cells. The Lagrangian cells correspond to the Lagrangian flow description, which is a way of looking at fluid motion where the observer follows an individual fluid particle as it moves through space and time. Every particle remains fixed with respect to the assigned Lagrangian cell over the time step interval. Each Lagrangian cell is coincident with a cell in a fixed Eulerian grid at the beginning of each time step, and moves and deforms over the time step interval. Figure 2.4 shows the change of the Lagrangian cell at the beginning and end of a single time step. Particles follow the macroscopic motion of Lagrangian cells, and move along trajectories which closely approximate the gas streamlines. Random particle motion associated with thermal energy is therefore suppressed. As a result, numerical diffusion errors, as well as effects of statistical scatter, are generally far smaller than in other DSMC-based equilibrium particle methods (Figure 2.5).

2.3.2 LD simulation procedure

The procedure, which is illustrated in Figure 2.3, is detailed here.

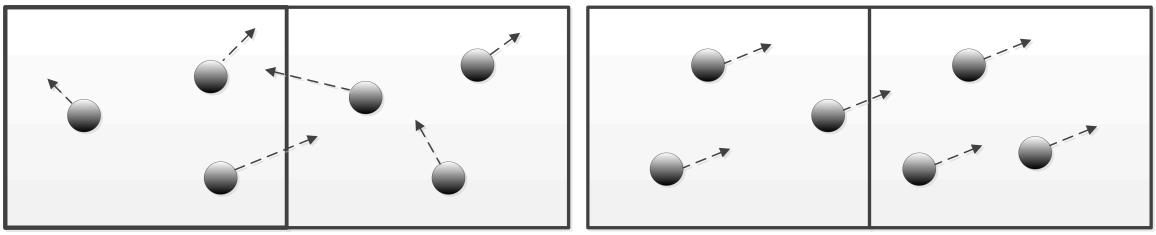

Figure 2.5: Reduction of random particle motions in the Lagrangian cell.

2.3.2.1 Determination of cell quantities

Each LD particle has information about the position, $\vec{X}_i$, velocity, $\vec{U}_i$, and species identifier. LD particles carry a bulk velocity, $\vec{U}_{b,i}$, and a bulk temperature, T_i, as well. The subscript i is the index for particle identification. The goal of the procedure is to update $\vec{U}_i$ for particle movement, and essential LD cell quantities are computed and stored as an initial step of the procedure. One vector and three scalar quantities are assigned to each cell: $\vec{U}_{cell}$ is the mass averaged particle bulk velocity, taken as a mass-weighted average over all particle velocities; ζ is the average number of internal degrees of freedom among all particles in a cell; ρ is the mass density; and β is the thermal speed scale for the cell. That is defined as the most probable thermal speed for a Maxwellian velocity distribution at the cell temperature T_{cell} [16].

$$\beta = \sqrt{\frac{< MW_i >}{2R_u T_{cell}}} \tag{2.19}$$

where

$$T_{cell} =< T_i > + \frac{< MW_i >}{(3+\zeta)R_u} \left(\frac{N_p}{N_p - 1} \right) \left(< \vec{U}_{b,i} \cdot \vec{U}_{b,i} >_m - < \vec{U}_{b,i} >_m \cdot < \vec{U}_{b,i} >_m \right) \tag{2.20}$$

Here, N_p is the number of particles in the cell, MW_i is the molecular weight of the assigned particle species, R_u is the universal gas constant, the operator $<>$ denotes an unweighted average over all particles in the cell, and $<>_m$ denotes a mass-average.

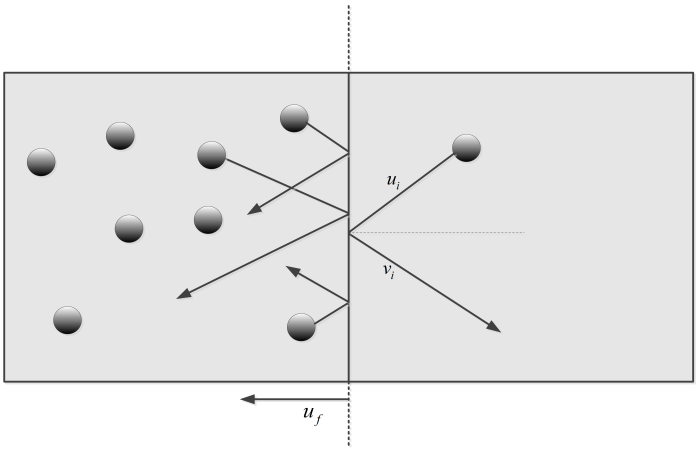

Figure 2.6: Momentum changes of LD particles colliding with a specular reflecting wall.

2.3.2.2 Calculation of Lagrangian cell velocity

To find a final LD particle velocity, the Lagrangian cell velocity must be calculated based on the cell quantities. The Lagrangian cell is bounded by massless, non-porous and specularly reflecting walls corresponding to each Lagrangian cell face. So, mass, net momentum and net energy cannot be transferred across the Lagrangian cell faces, i.e., total momentum and energy are conserved among all colliding gas molecules over time step interval, Δt. In Figure 2.6, the particles experience momentum changes when they collide with a specularly reflecting wall. To conserve the net momentum and energy, the face has a unique velocity, u_f [16].

The uniqueness of the Lagrangian cell face can be shown informally [16]. Imagine the Lagragian cell face moves with velocity u_f and a particle collides with incident velocity u_i. For simplicity, assume a one-dimensional problem with unit cross-sectional area, where v_i is the post-collision molecular velocity. Specular reflection requires that $v_i - u_f = -(u_i - u_f)$, so that $v_i = 2u_f - u_i$. The velocity is physically the ratio of the total incident normal momentum flux to total incident mass flux.

The total incident normal momentum flux to the surface is zero, because the momentum exchange between the face and a colliding gas molecule depends on the

normal component of the incident relative velocity in a coordinate system which moves at constant velocity $u_f\vec{n}$. Here, $\vec{n}$ is the outward normal unit vector with respect to the cell face. In the two neighboring cells (Figure 2.7), a scalar function, $G(u_f)$, can be defined based on the kinetic theory solution for the unidirectional normal momentum flux in an equilibrium flow (Equation (2.21))[8].

$$G(u_f) = \frac{\rho_1}{\beta_1^2}\left[s_1 exp(-s_1^2) + \sqrt{\pi}(1 + erf(s_1))\left(\frac{1}{2} + s_1^2\right)\right] \\ -\frac{\rho_2}{\beta_2^2}\left[s_2 exp(-s_2^2) + \sqrt{\pi}\,(1 + erf(s_2))\left(\frac{1}{2} + s_2^2\right)\right] \tag{2.21}$$

where $s_1 = \beta_1\left(\vec{U}_{cell,1}\cdot\vec{n} - u_f\right)$ and $s_2 = \beta_2\left(\vec{U}_{cell,2}\cdot\vec{n} - u_f\right)$. The Lagrangian face velocity which enforces momentum and energy conservation then corresponds to $G(u_f) = 0$. Equation (2.21) does not have a closed form solution, so an iterative procedure is required to solve for u_f. The secant method is used for initial guesses for u_f [8]. An iterative procedure is then performed on Equation (2.22), that is repeated until $|u_{f,i+1} - u_{f,i}|$ is within some small tolerance. The procedure to find u_f is repeated for all faces of each cell in the computational grid. The momentum flux relation used as a basis for Equation (2.21) is valid only for a simple gas. For a gas mixture, the characteristic thermal speed scale, β, will differ for each species, more massive atoms or molecules tend to have smaller thermal speeds at a given temperature [16].

$$u_{f,i+1} = u_{f,i} + (u_{f,i-1} - uf, i)\left(\frac{G(u_{f,i})}{G(u_{f,i}) - G(u_{f,i-1})}\right) \tag{2.22}$$

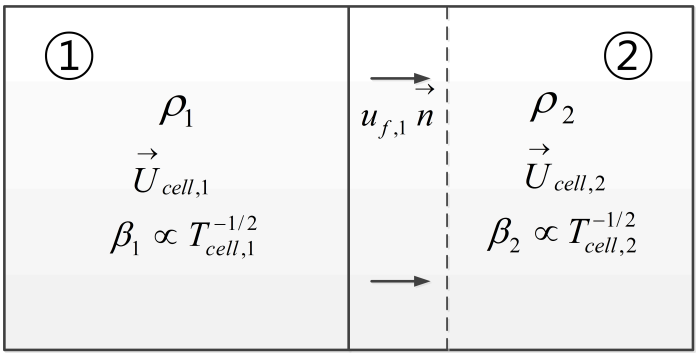

Figure 2.7: Two neighboring LD cells.

2.3.2.3 Reassignment of particle bulk velocity and temperature

While net momentum and energy are conserved, they can be exchanged across the Lagrangian cell face between two neighboring cells. As a simple example, imagine two neighboring cells with zero bulk velocity and equal pressure (Figure 2.7) which means the face is stationary. The normal velocity component of a particle is reversed after colliding with a stationary wall, so the particle will gain momentum in the inward normal direction. This momentum difference has to be transferred from the bordering cell over the face.

To account for momentum and energy exchange through the Lagrangian cell faces, bulk velocity and temperature values for all particles are updated during each time step. Total momentum and energy transferred to the cell through the face are expressed as Equation (2.23) and Equation (2.24) where A_j is the corresponding Eulerian face area, Δt is the time step interval, Φ_j is the unidirectional incident normal momentum flux, and $\vec{n}_j$ is the outward normal unit vector at the face. (The subscript j refers to the face index.). The momentum flux, Φ_j, is determined by equation (2.25) where $s_j = \beta\left(\vec{U}_{cell} \cdot \vec{n}_j - u_{f,j}\right)$.

$$\Delta M_j = -2A_j \Delta t \Phi_j \vec{n}_j \tag{2.23}$$

$$\Delta E_j = -2A_j \Delta t u_{f,j} \Phi_j \vec{n}_j \tag{2.24}$$

$$\Phi_j = \frac{1}{2\sqrt{\pi}} \frac{\rho}{\beta^2} \left[s_j exp(-s_j^2) + \sqrt{\pi}(1 + erf(s_j) \left(\frac{1}{2} + s_j^2 \right) \right] \tag{2.25}$$

Once ΔM_j and ΔE_j have been determined for all faces, particle bulk velocity and temperature values are updated to account for momentum and energy exchange across the Lagrangian faces. Each particle in the cell is assigned a new bulk velocity, $\vec{U}_{b,i}$. In Equation (2.26), V_{cell} is the cell volume, N_f is the total number of faces, and U_{cell}^{final} is the final cell bulk velocity after momentum exchange. Then, each particle is given a new temperature from Equation (2.27) and the initial temperature is Equation (2.28) [16].

$$\vec{U}_{b,i} = \vec{U}_{cell}^{final} = \vec{U}_{cell} + \frac{1}{\rho V_{cell}} \sum_{j=1}^{N_f} \Delta M_j \tag{2.26}$$

$$T_i = T_{cell}^{final} = T_{cell} + \frac{2}{(3+\zeta) n k_B} \left[\frac{1}{V_{cell}} \sum_{j=1}^{N_f} \Delta E_j - \frac{1}{2} \rho \left(\vec{U}_{cell}^{final} \cdot U_{cell}^{final} - \vec{U}_{cell} \cdot \vec{U}_{cell} \right) \right] \tag{2.27}$$

where

$$T_{cell} = \frac{\rho}{2 n k_B \beta^2} \tag{2.28}$$

The newly assigned particle bulk velocity, $U_{b,i}$, and temperature, T_i, will be equal for all particles in the cell.

2.3.2.4 Velocity reassignment for particle movement

To reassign the velocity for each particle movement, the locations of Lagrangian cell vertices at the end of time step interval are needed. Let $\vec{X}_{L,j}$ represent the final location of a Lagrangian cell vertex which is coincident with the Eulerian cell vertex

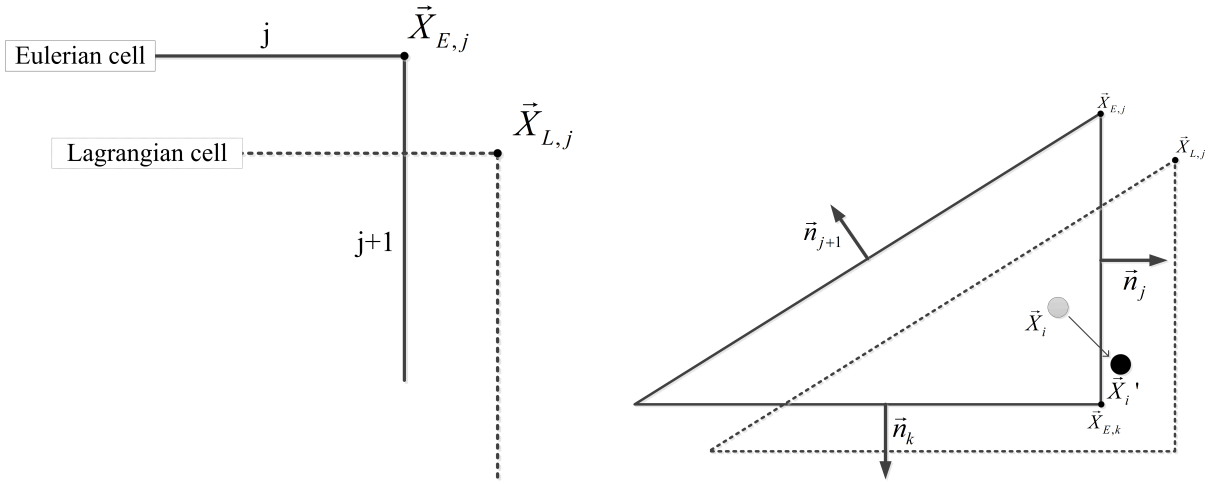

(a) Position of Lagrangian and Euler cells.

(b) Diagram of vectors used in procedures for particle velocity reassignment. Dashed lines represent Lagrangian cell faces at the end of the current time step [16].

Figure 2.8: Position of Lagrangian and Euler cells

$\vec{X}_{E,j}$ at the beginning of the time step. The vertex $\vec{X}_{E,j}$ is the intersection of two cell faces j and j+1 (Figure 2.8(a)). Then, the two unknown coordinates in $\vec{X}_{L,j}$ may be determined as a solution to Equation (2.29).

$$\begin{aligned} \left(\vec{X}_{L,j} - \vec{X}_{E,j}\right) \cdot \vec{n}_j &= u_{f,j}\Delta t \\ \left(\vec{X}_{L,j} - \vec{X}_{E,j}\right) \cdot \vec{n}_{j+1} &= u_{f,j+1}\Delta t \end{aligned} \tag{2.29}$$

Once the $\vec{X}_{L,j}$ values have been computed for all Lagrangian cells, the location of the particle at the end of the time step interval is computed assuming that each particle maintains the same relative position in the Lagrangian cell defined by the vertices $\vec{X}_{L,j}$. The final particle position $\vec{X}_i'$ is computed as a weighted sum of the

three $\vec{X}_{L,j}$ values (Equation (2.30)).

$$\vec{X}_i' = \sum_{j=1}^{N_f} \frac{\left(\vec{X}_i - \vec{X}_{E,k}\right) \cdot \vec{n}_k}{\left(\vec{X}_{E,j} - \vec{X}_{E,k}\right) \cdot \vec{n}_k} \vec{X}_{L,j} \tag{2.30}$$

where N_f is the total number of cell faces, $\vec{X}_i$ is the initial particle position, $\vec{n}_k$ is the outward normal unit vector for the face opposite vertex j, and $\vec{X}_{E,k}$ is the location of an Eulerian cell vertex along this face. Figure 2.8(b) illustrates the process. After the final particle location $\vec{X}_i'$ is determined, the particle velocity is reassigned to a new value as in Equation (2.31) for particle movement.

$$\vec{U}_i = \frac{\left(\vec{X}_i' - \vec{X}_i\right)}{\Delta t} \tag{2.31}$$

CHAPTER III

LD-DSMC Hybrid Numerical Method for Multiscale Flow

For simulation of a multiscale flow that has mixed equilibrium and nonequilibrium regions, a hybrid method provides a numerically efficient approach. The LD-DSMC hybrid method employs the DSMC method in the nonequilibrium region and the LD method in the equilibrium region. To hybridize these two methods, region allocation and information transfer between regions are essential. In addition, the LD method must have physical models that are consistent with DSMC to reduce information loss along continuum breakdown boundaries. These issues are discussed in this chapter.

3.1 Continuum Breakdown Evaluation and Cell Assignment

To employ both LD and DSMC methods as a part of the hybrid scheme, it is necessary to determine continuum breakdown to allocate cells to LD and DSMC domains. This is an area of current research, and Boyd et al. proposed the use of the gradient-length local (GLL) Knudsen number [14, 72].

$$Kn_{GLL} = \frac{\lambda}{Q}\left|\frac{dQ}{dl}\right| \tag{3.1}$$

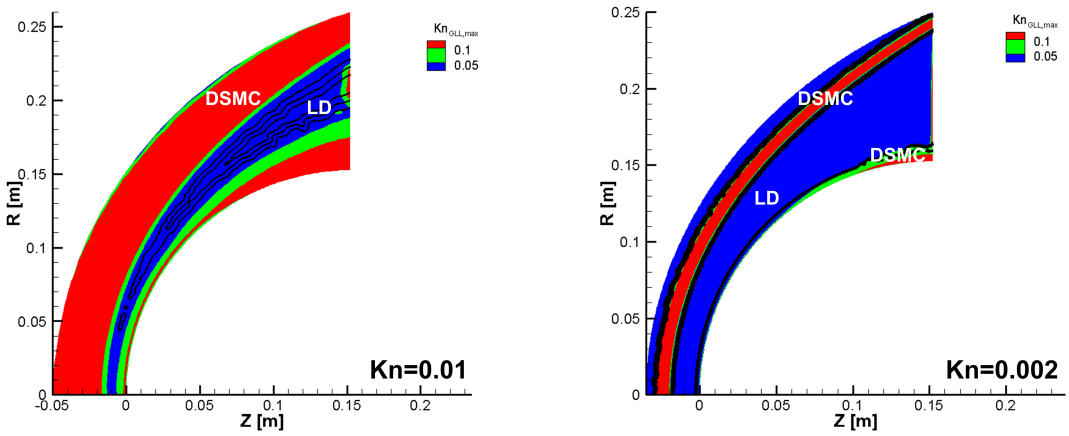

Figure 3.1: Continuum breakdown domain boundaries (Left: Kn=0.01, Right Kn=0.002).

where λ is the mean free path, l is some distance between two points in the flow field and Q is some flow quantity of interest, such as density, pressure, temperature, or velocity magnitude. Wang and Boyd found that representative hypersonic flows may be assumed sufficiently close to equilibrium to justify near-equilibrium assumptions when $Kn_{GLL,max} < 0.05$, where gradient length Knudsen numbers based on density, temperature, and bulk velocity were all considered [72]. So, LD-DSMC domain decomposition is determined based on the following GLL Knudsen number.

$$Kn_{GLL,max} = max\left(\frac{\lambda}{\rho}\left|\nabla\rho\right|, \frac{\lambda}{T}\left|\nabla T\right|, \frac{\lambda}{a}\left|\nabla u\right|\right) \tag{3.2}$$

where ρ is the density, T is the translational temperature, u is the bulk velocity magnitude, and a is the local speed of sound. Regions for which $Kn_{GLL,max}$ is larger than 0.05 are assigned to a DSMC/nonequilibrium domain, and all other regions are assigned to a LD/equilibrium domain. Domain decomposition is performed periodically once every few thousand time steps.

Figure 3.1 (left) shows the LD-DSMC domain decomposition for a Kn = 0.01, fore-

body sphere case. At this relatively high Knudsen number, most of the computational domain is simulated by the DSMC method and the LD region is confined to a thin layer downstream of the shock. This is a flow that is best computed fully using DSMC. To see potential advantages of the LD-DSMC hybrid simulation, a lower Knudsen number case is more appropriate. Figure 3.1 (right) shows contours of $Kn_{GLL,max}$ and the method domain boundaries for the case where Kn = 0.002. Here, the DSMC regions are confined to the shock wave and the boundary layer due to steep flow field gradients, and all other regions are assigned to LD.

3.2 Information Transfer at LD-DSMC Boundaries

After assigning LD and DSMC domains, information must be transferred across each domain boundary. Two layers of overlapping cells are employed along the boundary between DSMC and LD domains, and are designated as buffer regions A and B. These buffer regions are used for information exchange between the DSMC and LD domains. Each buffer region is positioned along the boundary between DSMC and LD domains, such that a line drawn from a DSMC cell to a nearby LD cell will pass through at least two cells in buffer region A, and then through at least two cells in region B. The relative locations of these buffer regions are illustrated in Figure 3.2 and Figure 3.3. In buffer region A, adjacent to the DSMC domain, all simulation procedures are carried out as in the DSMC cells, while in buffer region B, adjacent to the LD domain, the LD calculations are performed. In other words, the DSMC calculations are used for any cells in the DSMC domain. Note that a DSMC collision limiter is employed in place of the DSMC collision calculation for any cell in buffer region A. The LD calculations are applied in place of the DSMC collision calculation for all cells in the LD domain and in buffer region B. In the LD-DSMC hybrid simulation procedures, all cells in the fixed computational grid are periodically assigned one of four integer values, corresponding to the DSMC domain, the LD domain, or

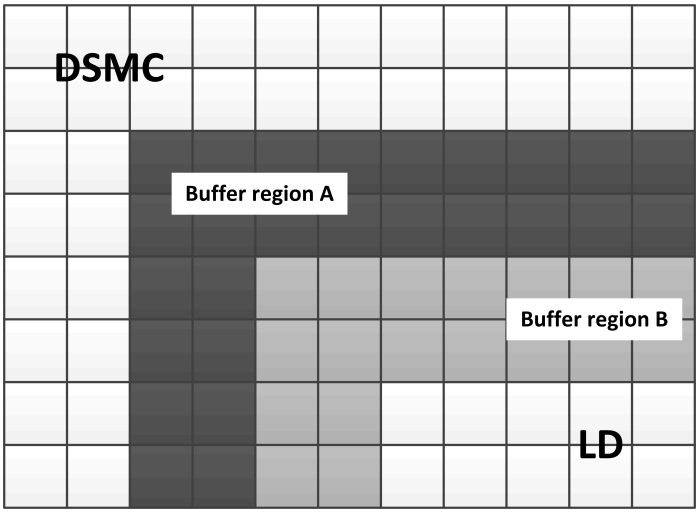

Figure 3.2: Schematic location of buffer regions.

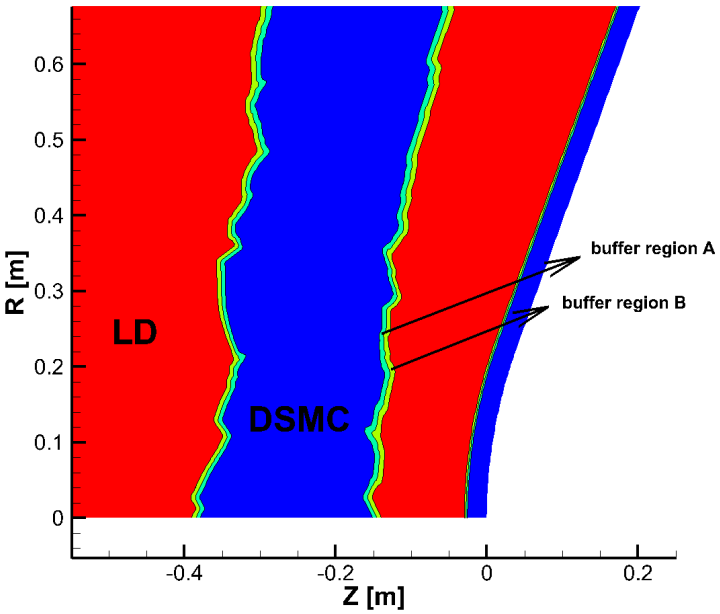

Figure 3.3: Location of buffer regions in a hybrid simulation.

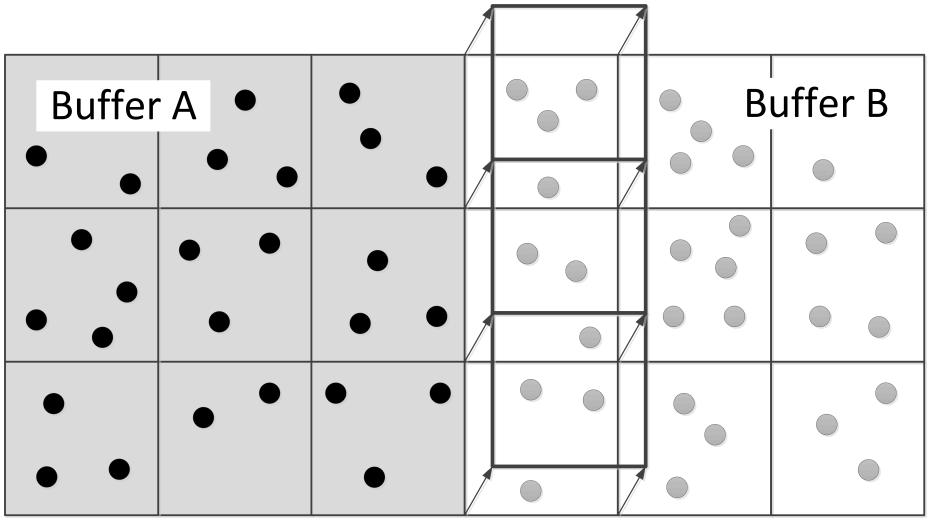

Figure 3.4: Bordering cells at the boundary of buffer region A and B.

one of the two buffer regions. This provides a simple and effective means of strongly coupled information transfer between LD and DSMC domains.

3.2.1 Determination of flow properties in buffer cells

At a boundary between LD and DSMC domains, a cell in buffer region B includes the faces bordering a cell in buffer region A (Figure 3.4). To handle this kind of bordering cell in buffer region A, cell averaged mass density, bulk velocity, and characteristic thermal speed must be evaluated as for LD cells. Also, the Lagrangian face velocities, u_f, are calculated for all faces of each cell in buffer region B which include the faces bordering a cell in buffer region A. From Equations (2.21) and (2.22), cell averaged density, bulk velocity, and characteristic thermal speed are needed to calculate the Lagrangian face velocities for any face between buffer regions A and B [16]. While the determination of cell properties in buffer region A could be carried out in a similar manner as the LD calculations, the large scatter associated with instantaneous cell-averaged properties in DSMC may introduce considerable unphysical fluctuations in flowfield properties computed using the LD method. To reduce these, a sub-relaxation procedure is used [67]. By using a sub-relaxation procedure,

the cell based instantaneous density, ρ^*_{cell}, and the mass-averaged bulk velocity, $\vec{U}^*_{cell}$, are calculated in each cell within buffer region A, using all particles in the cell during the current time step. Here, the bulk velocity, $\vec{U}^*_{cell}$, is a function of velocities used for DSMC particle movement, not bulk particle velocities used to assign momentum in the LD method. The characteristic thermal speed of cells in buffer region A is calculated as in Equation (3.3) which is the same as Equation (2.19) in the LD procedure.

$$\beta^*_{cell} = \sqrt{\frac{\langle MW_i \rangle}{2R_u T^*_{cell}}} \tag{3.3}$$

where the instantaneous cell-averaged temperature, T^*_{cell}, is calculated as in Equation (3.4).

$$T^*_{cell} = \frac{1}{(3 + \langle \zeta_i \rangle) R_u} \left[2 \langle E_i \rangle + \left(\frac{N_p}{N_p - 1} \right) \langle MW_i \rangle \left(\left\langle \vec{U}_i \cdot \vec{U}_i \right\rangle_m - \left\langle \vec{U}_i \right\rangle_m \cdot \left\langle \vec{U}_i \right\rangle_m \right) \right] \tag{3.4}$$

Here R_u is the universal gas constant, N_p is the number of particles, i is the particle index, and $\vec{U}_i, MW_i, \zeta_i$, and E_i are the velocity, molecular weight, number of internal degrees of freedom, and internal energy, respectively, for each particle in a cell of buffer region A. The operator $\langle\rangle$ denotes an unweighted average among all particles in the cell, while $\langle\rangle_m$ denotes a mass-weighted average such that $\langle U \rangle_m = U^*_{cell}$. Finally, these instantaneous density, velocity, and thermal speed scale values are used to update cell averaged properties as in Equation 3.5.

$$\begin{aligned} \rho_{cell} &= \theta \rho^*_{cell} + (1 - \theta) \rho^{n-1}_{cell} \\ \vec{U}_{cell} &= \theta \vec{U}^*_{cell} + (1 - \theta) \vec{U}^{n-1}_{cell} \\ \beta_{cell} &= \theta \beta^*_{cell} + (1 - \theta) \beta^{n-1}_{cell} \end{aligned} \tag{3.5}$$

where the superscript $n - 1$ denotes a value at the previous time step and θ is a relaxation factor for the DSMC buffer cell properties. For larger θ, the time lag in

averaged values is reduced but the scatter associated with instantaneous fluctuations in cell averaged quantities may increase.

3.2.2 Particle cloning and removal in buffer cells

For the strongly coupled means of exchanging information between rarefied and continuum flowfield regions, particle cloning and removal occur immediately before and after the particle movement procedures in buffer regions A and B. Immediately before the movement routines, every particle in both buffer regions A and B is cloned, so that two particles are located in each occupied position in each buffer cell. In buffer region A, where all particles are initially of DSMC type, each newly generated clone is treated as an LD type particle. The newly generated LD type clone has a new velocity used for movement procedures and a bulk velocity used to allocate momentum so that both velocities are equal to the cell velocity, $\vec{U}_{cell}$, as calculated in Equation 3.5. Each clone is also assigned a temperature, T_{cell}, which is computed as a function of β_{cell} and the cell averaged molecular weight $\langle MW_i \rangle$.

$$T_{cell} = \frac{\langle MW_i \rangle}{2R_u \left(\beta_{cell}\right)^2} \tag{3.6}$$

In buffer region B, where all particles are initially of LD type, a newly generated clone is treated as a DSMC type particle. The newly generated DSMC type clone has a new velocity based on probabilistic sampling procedures to have consistency with an equilibrium velocity distribution at the cell-averaged bulk velocity and temperature [8]. The new temperature of the DSMC type clone is set to zero. From the probabilistic sampling procedures, the DSMC type clone particle velocity component, $U_{i,j}$, in the j direction for a particle with index i is calculated as Equation (3.7).

$$U_{i,j} = \vec{U}_{cell} \cdot \vec{n_j} + \frac{sin\left(2\pi R_1\right)}{\beta_{cell}} \sqrt{-\frac{\langle MW_k \rangle}{MW_i} lnR_2} \tag{3.7}$$

where R_1 and R_2 are random numbers in the range $(0, 1]$

Immediately after particle movement procedures during each time step, any LD type particles in buffer regions A and any DSMC type particles in buffer regions B are removed. Therefore, only LD particles which have moved into buffer regions B are retained, and any LD particles which pass from buffer region B into a cell in buffer region A are destroyed. In the same way, only DSMC particles which have moved into buffer region A are retained, and any DSMC particles which pass to a cell in buffer region B are destroyed. The procedure enforces mass, momentum, and energy conservation when the number of particles per cell approaches infinity ($\theta = 1$) or enforces only mass conservation when $\theta = 0$. $\theta \in (0, 1)$ provides some balance between enforcing instantaneous momentum and energy conservation.

3.3 Physical Model Features of LD

3.3.1 Viscous Modification

The LD method for inviscid flow cannot properly resolve boundary layers or other regions involving large transverse gradients because the equilibrium assumption underlying the LD method makes it incapable of modeling physically realistic diffusive transport. To model viscous flow effects, the diffusive terms in the Navier-Stokes equations are evaluated in each cell during each time step. The diffusive term is used to modify particle velocity and temperature values in a manner consistent with DSMC transport coefficients at the near equilibrium limit. To account for viscous flow effects, diffusive momentum and energy transport are considered in the LD simulation procedure. Diffusive momentum and energy transport as well as momentum and energy transfer across the Lagrangian cell faces are accounted for in the reassignment of particle bulk velocity and temperature.

Diffusive transport contributions are determined through an explicit finite volume

solution to the viscous portion of the compressible Navier-Stokes equations. For a simple gas, the viscous transport equation can be written as Equation (3.8) assuming a Newtonian fluid using Stokes' hypothesis with all time independent advection terms removed [56].

$$\begin{aligned} \frac{\partial}{\partial t}\left(\rho u_i\right) - \frac{\partial}{\partial x_j}\tau_{ij} &= 0 \\ \frac{\partial e}{\partial t} - \frac{\partial}{\partial x_i}\left(k\frac{\partial T}{\partial x_i} + \tau_{ij}u_j\right) &= 0 \end{aligned} \tag{3.8}$$

where

$$\tau_{ij} = \mu\left(\frac{\partial u_j}{\partial x_i} + \frac{\partial u_i}{\partial x_j}\right) - \frac{2}{3}\mu\left(\nabla\cdot\vec{u}\right)\delta_{ij} \tag{3.9}$$

Here, τ_{ij} is the viscous stress tensor, $\vec{u}_i$ is the bulk velocity component in the x_i direction, μ is the dynamic viscosity, and k is the thermal conductivity. The specific total energy per unit volume, e, is $\rho c_v T + \frac{1}{2}\rho u_i u_i$, where c_v is the specific heat at constant volume.

By integrating Equation (3.8) over the cell volume, applying the divergence theorem and discretizing time derivatives over Δt, the momentum change, ΔM_i, and energy change, ΔE, in the cell due to diffusive transport in a two-dimensional simulation are as follows [43].

$$\begin{aligned} \Delta M_i &= \Delta t\sum_f^{N_f} A_f\left(\frac{4}{3}\mu\frac{\partial u'}{\partial x'}n_i + \mu\frac{\partial v'}{\partial x'}t_i\right)_f \\ \Delta E &= \Delta t\sum_f^{N_f} A_f\left(k\frac{\partial T}{\partial x'} + \frac{4}{3}\mu\frac{\partial u'}{\partial x'}n_i u_i + \mu\frac{\partial v'}{\partial x'}t_i u_i\right)_f \end{aligned} \tag{3.10}$$

where N_f is the total number of interior faces, A_f is the area of face f, n_i is the face outward-normal unit vector, t_i is the face tangent unit vector, u_i is the bulk velocity, u',v' are the bulk velocity components normal, and tangent to each face, and $\frac{\partial}{\partial x'}$ is the spatial derivative in the face outward normal direction. Face normal derivatives

$\frac{\partial}{\partial x'}$ are calculated by dividing the difference in a given quantity between neighboring cells by the dot product of n_i and the vector difference between cell center locations. μ, k, u_i are computed as unweighted averages among cell-based values for the cells on either side of the face. For consistency with DSMC in the LD-DSMC hybrid method, μ is determined as a power-law function of cell temperature using the VHS model.

$$\mu = \mu_{ref} \left(\frac{T}{T_{ref}} \right)^{\omega} \tag{3.11}$$

where

$$\mu_{ref} = \frac{15\sqrt{\pi m k_B T_{ref}}}{2\pi d_{ref}^2 \left(5 - 2\omega\right)\left(7 - 2\omega\right)} \tag{3.12}$$

where d_{ref} is the reference VHS collision diameter at T_{ref}, and m is the molecular mass. The thermal conductivity, k, is in turn calculated from μ using Eucken's relation [70].

$$k = \frac{1}{4}\left(15 + 2\zeta\right) R\mu \tag{3.13}$$

For further consistency with DSMC in a hybrid scheme, velocity slip and temperature jump along wall boundaries are employed [25]. These are based on a model developed specially for application to hybrid continuum-particle algorithms involving DSMC and are based on the standard DSMC treatment of gas-wall interactions. They have better consistency with DSMC than traditional gradient-based slip models, and are easier to implement and less prone to instabilities due to a lack of dependence on cell gradient evaluations. The net tangential momentum flux, f_{t-M}, and energy flux, f_E, onto a wall boundary are given as a function of the specific gas constant, R, specific heat ratio, $\gamma = \frac{(\zeta+5)}{(\zeta+3)}$, tangential bulk velocity, u_t, wall temperature, T_w, and

wall thermal accommodation coefficient, σ_w.

$$f_{t-M} = \sigma_w u_t \rho \sqrt{\frac{RT}{2\pi}}$$
$$f_E = \frac{1}{2}\sigma_w \left(\frac{\gamma+1}{\gamma-1}\right) \rho R \left(T - T_w\right) \sqrt{\frac{RT}{2\pi}} \tag{3.14}$$

A wall boundary face is treated in a similar manner to a symmetry boundary face, for which the corresponding Lagrangian face will have zero normal velocity but no limitations are set on the cell temperature or bulk velocity. However, additional momentum and energy transport to the cell will occur along a wall boundary face. Given a wall temperature, and thermal accommodation coefficient, specified as simulation input parameters, the following expressions are used to determine the viscous contributions to changes in cell momentum and energy, ΔM_i and ΔE, respectively, at wall boundary face, f, over the time step interval, Δt.

$$\Delta M_i = -\sigma_w \Delta t A_f \left(t_i t_j\right)_f u_j \rho \sqrt{\frac{RT}{2\pi}}$$
$$\Delta E = -\frac{1}{2}\sigma_w \Delta t A_f \left(\zeta + 4\right) \rho R \left(T - T_w\right) \sqrt{\frac{RT}{2\pi}} \tag{3.15}$$

For a cell that borders a wall boundary, the total viscous changes in cell momentum and energy are calculated as a summation of Equations (3.10) and (3.15). The total momentum and energy transfer due to the viscous flow effects are used to update cell-based velocity and temperature values.

3.3.2 Rotational and Vibrational Nonequilibrium

In some cases, we can assume thermal equilibrium with full accommodation of internal energy modes to the translational temperature and a fixed number of internal degrees of freedom. This is quite accurate for low temperature and very low Knudsen number, but both thermal nonequilibrium and vibrational energy effects

may become significant at higher temperature and higher Knudsen number. Also, rotational nonequilibrium could be important at higher Knudsen number. Both rotational temperature lag and nonequilibrium rotational energy distributions can be observed within shocks or regions of rapid expansion. So, rotational and vibrational nonequilibrium models need to be included in the continuum region when significant internal energy nonequilibrium effects exist. This improves consistency with the DSMC method and reduces information loss along continuum breakdown boundaries. Here, two different approaches are discussed [21].

Particles that move between rarefied and continuum regions may carry their assigned rotational/vibrational energies across the boundaries between the two regions. Then, information loss regarding the shape of the internal energy distribution functions is reduced, and non-equilibrium energy distributions can be maintained in a continuum region through the same efficient Monte Carlo representation as in standard DSMC. In the equilibrium LD region, frequent intermolecular collisions tend to force the internal energy distributions toward an equilibrium Boltzmann distribution with redistribution of energy between internal and translational modes to enforce energy equipartition. Energy redistribution between different modes and between different levels within each internal mode should be included in calculation procedures. The assignment of a temperature value to each particle makes such energy redistribution procedure particularly simple in the LD method.

There are two different approaches for modeling rotational/vibrational nonequilibrium in the LD method. Here, a rotational energy, ϵ_r, and a vibrational energy, ϵ_v, are assigned to each newly generated particle along inflow boundaries exactly like DSMC and these values are sampled from equilibrium distributions at the imposed inflow temperature. The temperature value, T, assigned to each particle represents only the translational temperature, and the cell-averaged temperature is independent of any internal degrees of freedom. During particle cloning procedures related to in-

formation exchange between LD and DSMC, ϵ_r, ϵ_v from parent particles are assigned to the newly generated clones. The first approach has greater efficiency and reduced sensitivity to time step size, while the second approach is easier to implement in an existing standard DSMC code [21].

3.3.2.1 First Approach

In the first approach, we can express the rate of relaxation toward the internal energy, e^*, which is related to the instantaneous translational thermal energy, e_t, given an internal energy mode with an average energy value, e, and number of degrees of freedom, ζ.

$$\frac{de}{dt} = \frac{e^* - e}{\tau} \tag{3.16}$$

where τ is the characteristic internal energy relaxation time. If ζ is assumed constant then e^* and e_t may be related by $\frac{e^*}{e_t} = \frac{\zeta}{3}$. If e and e_t are the average internal energy and translational energy, and e^0 and e_t^0 indicates their initial values, then $e + e_t = e^0 + e_t^0$ by energy conservation. Then e^* can be written as:

$$e^* = \frac{\zeta}{3}\left(e^0 + e_t^0 - e\right) \tag{3.17}$$

Substitute Equation (3.17) into Equation (3.16)

$$\frac{de}{dt} = \frac{C}{\tau}\left(\frac{\zeta\left(e^0 + e_t^0\right)}{3C} - e\right) \tag{3.18}$$

where $C = 1 + \frac{\zeta}{3}$. If τ is assumed constant, Equation (3.18) can be integrated over a finite time interval, Δt, to express e as a function of e^0 and e_t^0.

$$e\left(\Delta t\right) = \frac{\zeta}{3C}\left[1 - exp\left(-C\frac{\Delta t}{\tau}\right)\right]e_t^0 + \left[1 - \frac{1}{C}\left(1 - exp\left(-C\frac{\Delta t}{\tau}\right)\right)\right]e^0 \tag{3.19}$$

If we denote $(e^*)^0$ as the average internal energy at equilibrium with the initial translational energy e_t^0, $\frac{(e^*)^0}{e_t^0} = \frac{\zeta}{3}$. Substitute this into Equation (3.19).

$$e\left(\Delta t\right) = P\left(e^*\right)^0 + \left(1 - P\right)e^0 \tag{3.20}$$

where

$$P = \frac{1}{C}\left[1 - exp\left(-C\frac{\Delta t}{\tau}\right)\right] \tag{3.21}$$

P is the fractional contribution of $(e^*)^0$ to internal energy, e, after an elapsed time, Δt. Average energy, e, can be found at Δt by resampling a fraction P of gas molecule internal energy value from an equilibrium distribution at the initial translational temperature. For LD particles, ϵ_r, ϵ_v and T are updated every time step before determining the cell quantities.

Rotational-translational energy exchange occurs when the probability of rotational-translational energy exchange, P_{rot}, is larger than a random number, R, between 0 and 1, in which case the particle rotational energy is resampled from an equilibrium distribution at temperature, T.

$$P_{rot} = \frac{1}{C_r}\left[1 - exp\left(-C_r\frac{f\Delta t}{Z_{rot}}\right)\right] \tag{3.22}$$

where f is the collision frequency using the VHS model of Bird.

$$f = \sum_j \frac{T}{2}\left(d_i + d_j\right)^2 n_j \left[2\pi k_B T_{ref}\left(\frac{m_i + m_j}{m_i m_j}\right)\right]^{0.5}\left(\frac{T}{T_{ref}}\right)^{1-\omega} \tag{3.23}$$

where d_j is the reference collision diameter, m_j is the molecular mass, n_j is the cell-based local number density, T_{ref} is the VHS reference temperature, and ω is the VHS

temperature exponent for viscosity.

$$Z_{rot} = \frac{Z_{max}}{1 + \frac{1}{2}\pi^{\frac{3}{2}} \left(\frac{T^*}{T}\right)^{\frac{1}{2}} + \left(\pi + \frac{1}{4}\pi^2\right) \frac{T^*}{T}} \tag{3.24}$$

where T^* is the reference temperature and Z_{max} is the maximum rotational collision number using the model of Parker [48].

Next, vibrational-translational energy change will occur when the probability of vibrational-translational energy exchange, P_{vib}, is larger than some random number, R, between 0 and 1.

$$P_{vib} = \frac{1}{C_v}\left[1 - exp\left(-C_v \frac{\Delta t}{\tau_v}\right)\right] \tag{3.25}$$

where τ_v is the total vibrational relaxation time. An initial relaxation time τ_{MW} is found using the correlation of Milikan and White [44].

$$\tau_{MW} = \frac{exp\left(AT^{-1/3} + B\right)}{P} \tag{3.26}$$

where $A = 0.00116\left(\frac{1}{2}N_A m_i\right)^{\frac{1}{2}}\theta_i^{\frac{4}{3}}$ and $B = -0.015A\left(\frac{1}{2}N_A m_i\right)^{\frac{1}{4}} - 18.42$. Here P is the cell-based local pressure, θ_i is the characteristic vibrational excitation temperature, N_A is Avogadro's number, m_i is the species mass and τ_{MW} is the relaxation time in sec. To improve accuracy, the correlation of Park is used at high temperature [47].

$$\tau_{vib} = \tau_{MW} + \frac{1}{\sigma_v n_{tot}}\left(\frac{\pi m_i}{8k_B T}\right)^{1/2} \tag{3.27}$$

where n_{tot} is the total cell-based number density, and σ_v is the reference collision cross-section.

Finally, once both rotational-translational and vibrational-translational energy exchange have been considered for each particle, the particle temperature is updated

to enforce conservation of total energy.

$$T \longleftarrow T + \frac{\epsilon_r^0 + \epsilon_v^0 - \epsilon_r - \epsilon_v}{\frac{3}{2}k_B} \tag{3.28}$$

where ϵ_r^0, ϵ_v^0 are the initial rotational and vibrational energy values before the internal energy exchange operations.

3.3.2.2 Second Approach

The second approach is simpler and easier to implement than the first, and uses the same energy exchange routines already employed in a pre-existing DSMC code. For all particles in a given cell, velocity components in the particle data structure used for particle movement are resampled from a Maxwellian distribution at the translational temperature, T_c, assigned to the cell.

$$u_k = \left(-ln\left(R_1\right)\frac{2k_BT_c}{m_i}\right)^{1/2} sin\left(2\pi R_2\right) \tag{3.29}$$

where R_1, R_2 are two random number and m_i is the molecular mass for particle i. Then, the average translational energy, e_t^0, associated with particle velocities in the cell is as follows.

$$e_t^0 = \left\langle \frac{1}{2}m_i u_k u_k \right\rangle \tag{3.30}$$

Collision partners are then assigned among all particles in the cell. The only difference with respect to traditional collision selection is that each collision probability is multiplied by a factor P_{max} between 0 and 1 which is unique to this cell. At simulation startup, P_{max} is initialized for all cells at a small positive value much less than one and is subsequently increased to match the maximum inelastic collision probability in each cell. In the collision operation, the velocity components, u_k, and the internal energies, ϵ_r and ϵ_v, may be modified for each colliding particle. The probabilities P_{rot} and P_{vib}

of rotational-translational and vibrational-translational energy exchange during each collision are divided by the factor P_{max}. In most cases, $P_{rot} >> P_{vib}$ due to differences between rotational and vibrational collision numbers. We ensure that the conditions $\frac{P_{rot}}{P_{max}} \leq 1$ and $\frac{P_{vib}}{P_{max}} \leq 1$ are both generally satisfied by setting $P_{max} = min\{P_{rot}, 1\}$ if $P_{rot} > P_{max}$ for any collision in this cell. Then, an updated average translational energy, e_t, in the cell is found by repeating Equation (3.30) with post collision particle velocity, u_k. The change in translational energy, $e_t - e_t^0$, is then incorporated into the cell temperature as:

$$T_c \longleftarrow T_c + \frac{2}{3k_B}\left(e_t - e_t^0\right) \tag{3.31}$$

The LD-DSMC hybrid approach including viscous and internal energy effects is summrized in Figure 3.5.

3.3.3 Diffusive transport

3.3.3.1 Diffusive Mass transport

Accurate simulation of flows involving a gas mixture may require that diffusive mass transport be considered. In collision cross-section models, the variable soft sphere (VSS) is considered to be more effective to take more accurate diffusive mass transport into account [39]. Basically, the VSS model is used to calculate binary collision cross sections in DSMC, and assumes that the viscosity is proportional to the temperature raised to a constant power, $0.5+\omega$, in near equilibrium flow, like the VHS model. While the VHS model assumes isotropic scattering, however, the VSS model considers anisotropic scattering. The details of the VHS and the VSS models are discussed in section 2.2.3.

Based on the VSS collision model, the cell based mixture dynamic viscosity, μ_{cell}, and the cell-based mixture thermal conductivity, k_{cell}, are found [74]. The cell based dynamic viscosity and thermal conductivity are functions of viscosity, μ_s, and thermal

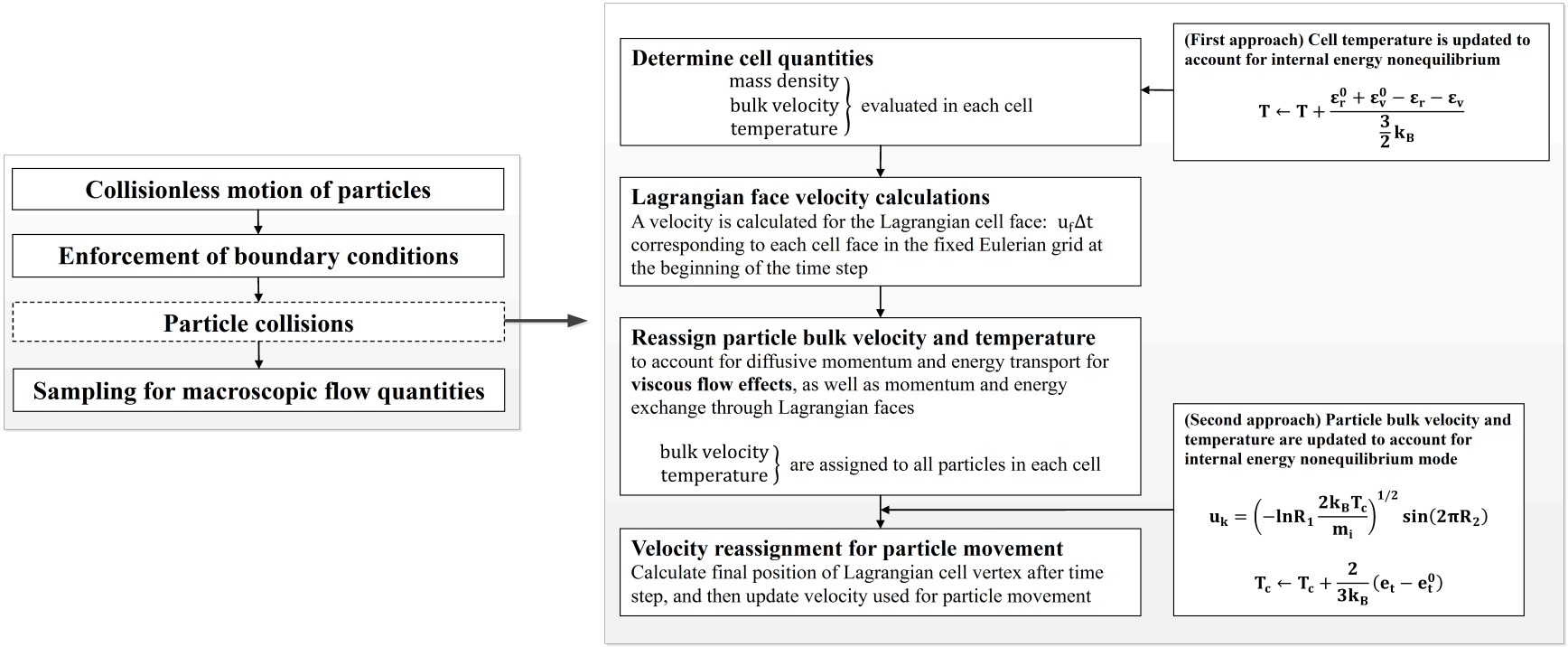

Figure 3.5: Simulation procedure performed during each time step of the LD method which includes viscous effects and internal energy nonequilibrium.

conductivity, k_s, for each species. The viscosity, μ_s, for species s in a given cell is:

$$\mu_s = \mu_{ref,s} \left(\frac{T_{cell}}{T_{ref}} \right)^{\omega_s + 0.5} \tag{3.32}$$

where T_{cell} is the cell-averaged temperature during current time step, T_{ref} is the reference temperature, ω_s is the species-specific constant used in the collision cross section model (VSS) and $\mu_{ref,s}$ is the species viscosity at the reference temperature. The reference viscosity is calculated for each species as a function of mass per molecule, m_s, species-diffusive data, α_s, and VSS collision diameter, $d_{ref,s}$, at the reference temperature, T_{ref}.

$$\mu_{ref,s} = \frac{5\left(\alpha_s + 1\right)\left(\alpha_s + 2\right)\sqrt{m_s k_B T_{ref}/\pi}}{4\alpha_s\left(5 - 2\omega_s\right)\left(7 - 2\omega_s\right) d_{ref,s}^2} \tag{3.33}$$

Based on the species transport coefficients, μ_s and k_s, cell-based mixture transport coefficients, μ_{cell} and k_{cell}, can be found using Wilke's semi-empirical mixing rule [74]. Mixture transport coefficients are evaluated as weighted sums over the species values (Equation (3.34)).

$$\begin{aligned} \mu_{cell} &= \sum_s \frac{N_s \mu_s}{\phi_s} \\ k_{cell} &= \sum_s \frac{N_s k_s}{\phi_s} \end{aligned} \tag{3.34}$$

where N_s is the number of particles of species s in the current cell and ϕ is evaluated as:

$$\phi_s = \sum_r N_r \frac{\left[1 + \sqrt{\frac{\mu_s}{\mu_r}} \left(\frac{m_r}{m_s}\right)^{0.25}\right]^2}{\sqrt{8\left(1 + \frac{m_s}{m_r}\right)}} \tag{3.35}$$

Finally, a mixture diffusion coefficient, D_{cell}, is computed as a function of the VSS

self-diffusion coefficient for each species (Equation (3.36)). All mixture properties are updated during each time step and stored in the cell data structure [19].

$$D_{cell} = \frac{1}{\rho_{cell}} \sum_{s} \frac{N_s}{\phi_s} \left[\frac{3\alpha_s}{5} \left(\frac{7 - 2\omega_s}{2 + \alpha_s} \right) \mu_s \right] \tag{3.36}$$

Diffusive momentum and energy transport are modeled to consider viscous flow effects in the LD method by modifying the procedure in updating cell-based bulk velocity and temperature. To account for mass transport due to molecular diffusion in the viscous flow, a cell-based approach which includes adjustments to particle trajectories is required. In the LD simulation procedure which is described in section 2.3.2, the updated particle velocity is determined by $\frac{\left(\vec{X}_i' - \vec{X}_i\right)}{\Delta t}$ (Equation (2.31)) which corresponds to the Lagrangian face movement distance, $u_f \Delta t$. To include mass diffusion effects, the final particle position, $\vec{X}_i'$ is changed using weighted sums of species-specific Lagrangian vertex coordinates. This corresponds to movement of each Lagrangian cell face over distance, $(u_f + u_{f,ds})\,\Delta t$, instead of $u_f \Delta t$ as used previously. $u_{fd,s}$ is the Fick's law diffusion velocity for species s at the face f. It is computed during every time step for all simulation species using the following expression.

$$u_{ds,f} = -\frac{D_f}{Y_{f,s}} \frac{\partial Y_s}{\partial n} \tag{3.37}$$

Here D_f is the diffusion coefficient evaluated at the face f, $Y_{f,s}$ is the mass fraction of species s at the face, and $\frac{\partial Y_s}{\partial n}$ is the gradient of $Y_{f,s}$ in the direction of the outward normal unit vector $\vec{n}_f$ at the face. The effect of mass diffusion on the motion of an individual particle is dependent on the relative position of that particle with respect to its assigned cell. Therefore, diffusive mass transport can occur in multiple directions, and particle trajectories effectively reproduce the large scale bulk motion of particles in the presence of a concentration gradient.

3.3.3.2 Diffusive Internal Energy Transport

In section 3.3.3.1, diffusive mass transport is detailed for a gas mixture. In the same manner, diffusive transport may need to be considered in the internal energy nonequilibrium. Without considering this transport, nonphysical transverse gradients or discontinuities can exist in vibrational or rotational temperature.

To account for vibrational energy diffusive transport, a vibrational temperature T_v is included in the cell data structure and stored separately for every cell. During each time step, T_v is updated using an exponential moving average to reduce scatter relative to the instantaneous cell-based temperature [67].

$$T_v = (1-\alpha)\, T_v^* + \frac{\alpha\theta_v}{ln\left(k_B\theta_v / \langle e_v \rangle\right)} \tag{3.38}$$

where T_v^* is the vibrational temperature of the cell at the previous time step, $\langle e_v \rangle$ is the average vibrational energy in the cell, θ_v is the characteristic vibrational temperature for the gas species, and α is the relaxation parameter. Once T_v has been updated for all cells during the current time step, a finite volume procedure is performed to determine the total change in vibrational energy, ΔE_v. This value should be added to each cell over each timestep interval to account for diffusive transport.

$$\Delta E_v = \Delta t \sum_{f=1}^{N_f} A_f \left(k_v\right)_f \left(\frac{\partial T_v}{\partial n}\right)_f \tag{3.39}$$

where N_f is the total number of cell faces, A_f is the face area, $\left(k_v\right)_f$ is the unweighted average of vibrational thermal conductivity values for cells on either side of a face, and $\left(\frac{\partial T_v}{\partial n}\right)_f$ is the normal gradient in T_v along the face. The vibrational thermal conductivity, k_v, of each cell is evaluated through Eucken's relation as a function of

the dynamic viscosity, μ, and molecular mass, m [70].

$$k_v = \frac{\mu k_B}{m} \frac{\theta_v / T_v}{exp\left(\theta_v / T_v\right) - 1} \tag{3.40}$$

Once the total vibrational energy has been computed for a given cell, particle vibrational energy values in the cell are modified to account for the addition or removal of energy due to vibrational energy diffusive transport. To enforce energy conservation, all particle vibrational energy values, e_v, are multiplied by a factor F_v.

$$F_v = 1 + \frac{\Delta E_v}{W\left(\Delta t / \Delta t_{ref}\right) N_p \left\langle e_v \right\rangle} \tag{3.41}$$

where W is the cell numerical weight, Δt_{ref} is the global reference time step, and N_p is the number of particles per cell.

3.4 Efficiency Study

For accurate simulation, the standard DSMC method requires a large enough computational grid, a small enough time step, and a large enough number of particles per cell. At a minimum, the DSMC cell size should be smaller than the mean free path, and the DSMC time step interval should be smaller than the mean collision time, to obtain valid results. However, the LD method is relatively independent of such requirements. Therefore, we need to optimize the requirement in the LD-DSMC hybrid simulation. In this chapter, an effort to optimize the numerical constraints and to increase the LD-DSMC hybrid simulation efficiency is discussed.

3.4.1 Subcell Utility for DSMC Collision Calculation

In the LD-DSMC hybrid simulation, an LD cell does not need to satisfy the guideline of DSMC that the cell size should be smaller than the mean free path. This means

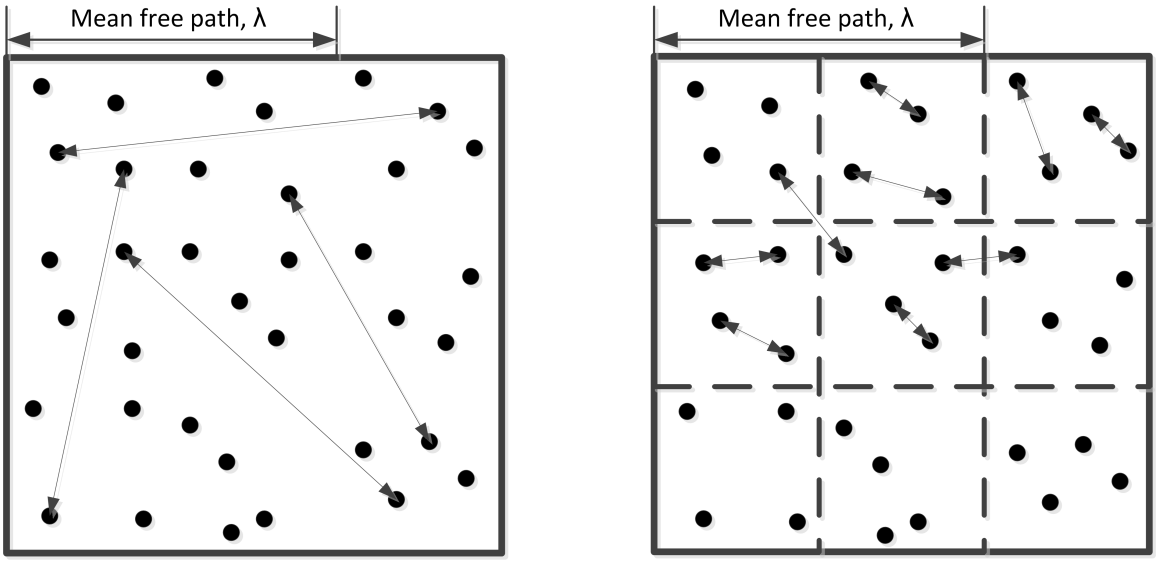

Figure 3.6: Cell configuration with and without subcells.

LD cells can be larger compared with DSMC cells and the relatively larger LD cells may increase the efficiency of the LD-DSMC hybrid simulation. Hybrid simulations are performed on a mesh which is sufficiently coarse for mesh independence in LD calculations, but coarser than necessary to meet DSMC guidelines. The DSMC cells are ,therefore, divided into subcells with subcell dimensions set to approximately half the mean free path. Collision partners are then selected from particles located in either the same subcell or neighboring subcells. This procedure can reduce the mean collision separation between two molecules that are selected as collision partners. Figure 3.6 conceptually describes a cell with and without subcells.

Even though subcells promote nearest neighbor collisions and minimize mean collision separation, the collision rate depends on the number density that is resolved by the collision cell. An insufficient number of particles per collision cell along with inappropriate temporal and spatial discretization are sources of stochastic errors, which violate the accuracy of the binary collision procedure. The stochastic errors result in an unacceptable increase in the number of repeated collisions in a cell and unrealized potential for collision between particles at small separation distance situated in neigh-

boring cells. Therefore, a DSMC collision cell needs a sufficient number of subcells to avoid such problem [9]. In the current LD-DSMC algorithm, a DSMC cell is divided into subcells if it does not satisfy the DSMC requirement and each subcell is forced to have a certain number of particles. Otherwise, all other cells have the 'desired number of particles'. This promotes uniform and sufficient numbers of particles per cell. In this research, the desired number of particles per cell is 30, the maximum number of subcells in each direction is 20, and the desired number of particles per subcell is 4.

3.4.2 Numerical Weight and Time Step Adaptation

Although the subcell utility is used to satisfy the DSMC guidelines on a much coarser mesh, larger cells may induce too many particles per cell. The DSMC technique usually requires at least 20 particles per cell to reduce statistical noise; too many particles per cell may decrease computation efficiency. To control this, an adaptive numerical weight scale factor which contributes to the number of particles per cell, and time step scale factor adaptation are used. In the DSMC or LD simulation, many real particles are treated as one simulation particle. The numerical weight is a parameter used to represent how many real particles are treated as one simulation particle. Thus, a cell with a weight scale factor of 0.5 will have a particle weight of one half the reference values. The weight scale factor is declared in each cell of the domain, and helps to maintain an appropriate number of particles per cell.

Immediately after domain decomposition, additional procedures are performed to optimize the time step interval, Δt, and the numerical weight, W, for each cell. At first, Δt is calculated in both LD and DSMC regions. In the LD domain, Δt is calculated to give a desired Courant number while Δt is set to 0.2 times the local mean collision time in the DSMC domain. This allows a relatively large time step interval in the LD regions and may contribute to increased computational efficiency

with similar level of accuracy. Next, the minimum desired number of particles, N_d, is determined in each cell. In the LD domain, a uniform N_d value of 20 or 30 is used, while N_d varies as a function of the ratio of cell size to mean free path, in order to fix the expected number of particles per subcell, in the DSMC domain.

Once both Δt and N_d have been determined for a given cell, the cell numerical weight is updated. The new weight is a power of two and is set such that the expected number of particles in the cell is between N_d and $2N_d$. This new weight is calculated as $W = 2^P$ where

$$P = \left\lfloor \frac{1}{ln2} ln \left(W^* \frac{\langle N_p \rangle \, \Delta t^*}{N_d \Delta t} \right) \right\rfloor \tag{3.42}$$

where the superscript $*$ represents values at the previous time step, the operator $\lfloor \rfloor$ rounds to the nearest smaller integer, and $\langle N_p \rangle$ is the time averaged number of particles in the cell. Finally, a smoothing operation to provide more uniform integer values for P among nearby cells is performed [20].

Once the numerical weight, W, is determined, all particles in the cell are considered for cloning or removal. Particles are cloned or removed to correct for cell-based variations in numerical weight, so that the current number of particles N_p in the cell will change on average by the factor $\frac{W^* \Delta t^*}{W \Delta t}$. Time averaged quantities (such as T_v and $\langle N_p \rangle$) stored in the cell data structure are multiplied by this same factor.

The above procedures are intended to allow appropriate Δt and W assignment within the LD domain, while enforcing requirements for timestep and mean collision separation in the DSMC domain. Far more particles may be located in each DSMC cell than in each LD cell, and the primary means of efficiency gains of the hybrid method over standard DSMC will be through a large reduction in the particle population within the continuum regions. The procedure is described as a flowchart in Figure 3.7

Due to spatial variation in the numerical weight, some particles must be cloned or destroyed when they pass between neighboring cells with different numerical weights.

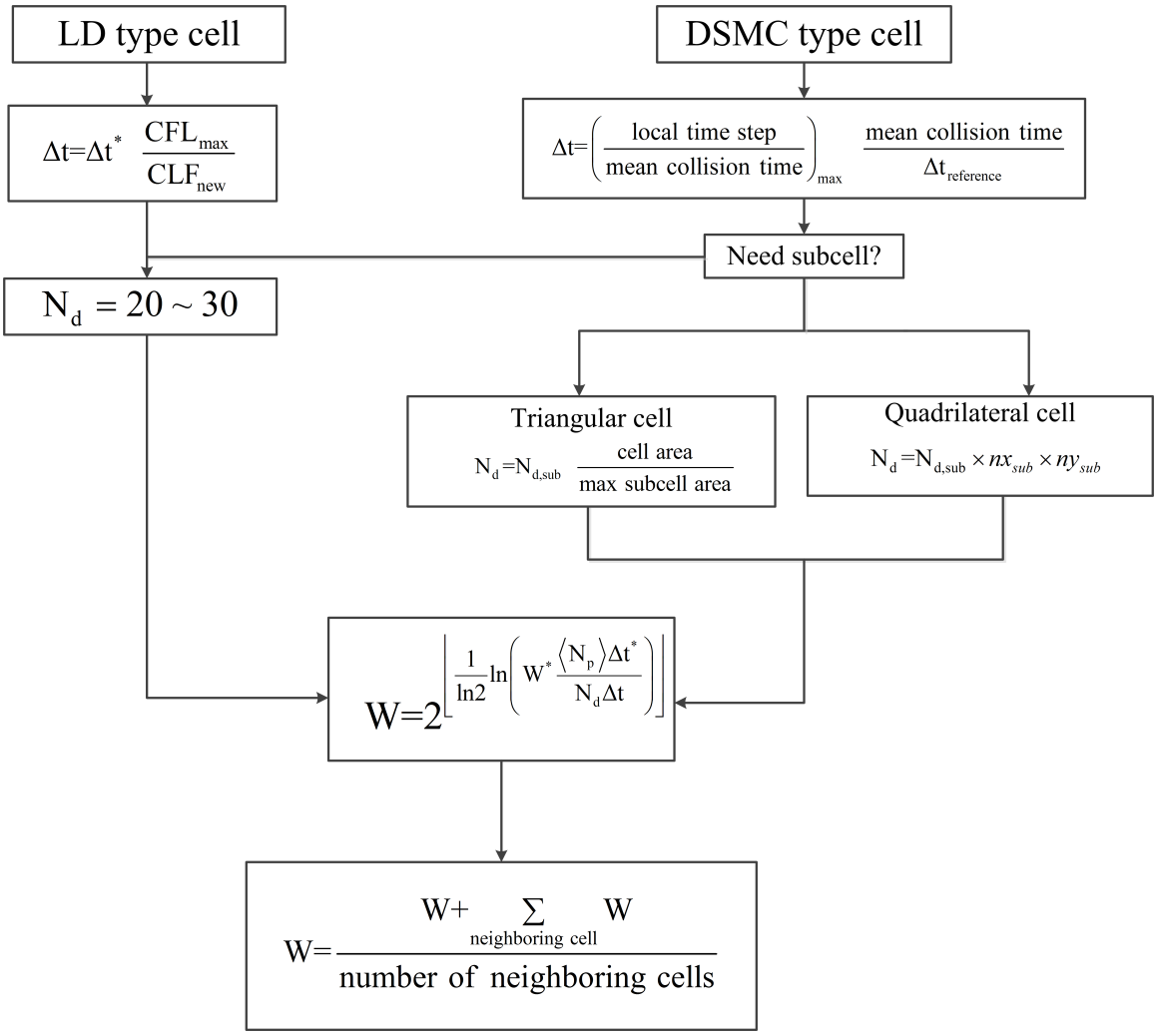

Figure 3.7: Numerical weight and time step adaptation in the LD-DSMC algorithm.

To avoid accuracy loss due to particle cloning or removal, values of the numerical weight are restricted to powers of 2. This tends to produce large regions of the mesh within which all cells are assigned to the same weight. This dramatically reduces the frequency of particle cloning and removal, which should in turn reduce the errors associated with these processes. Also, buffers are used to delay the introduction of clone particles. Each newly generated clone particle is placed in a cell-based link buffer list for the following ten time steps, before being released and allowed to participate in moving and colliding operations [8].

CHAPTER IV

Initialization with Navier-Stokes Solver

The LD-DSMC hybrid simulation has been initialized with standard DSMC until the first continuum breakdown. After the first continuum breakdown, the computational domain is decomposed into LD and DSMC regions, and the hybrid simulation starts. The main alternative to hybrid LD-DSMC simulation is a CFD-DSMC hybrid simulation that is significantly faster because it initializes the method decomposition by evaluating breakdown based on an initial CFD solution. Therefore, a Navier-Stokes solution is employed to initialize the LD-DSMC hybrid simulation to increase computational efficiency. It also helps to assign effective cell sizes for each LD and DSMC region. In this chapter, detailed investigation of initialization and the process of cell refinement are presented.

4.1 Equilibrium Gas - Continuum Description

If the particles of the gas are in a state of 'maximum disorder', the gas will be in equilibrium. The equilibrium gas description is only valid in the regions where the continuum flow assumption applies. If the local velocity distribution function, f, is assumed to be a slightly perturbed Maxwellian (termed a Chapman-Enskog velocity distribution), the result of taking the zeroth, first, and second moments of the Boltzmann equation are the well known Navier-Stokes equations [8, 28]. Therefore,

the Navier-Stokes equations provide the conventional mathematical model of a gas as a continuum. This work uses CFD techniques to solve the Navier-Stokes equations. The NS equations become unsuitable for studying rarefied flows with finite Knudsen numbers where the distribution function, especially in shock waves, becomes strongly non-equilibrium. The 2D Navier-Stokes equations can be written as [73]:

$$\frac{\partial \tilde{U}}{\partial t} + \frac{\partial \tilde{F}}{\partial x} + \frac{\partial \tilde{G}}{\partial y} = 0 \tag{4.1}$$

where $\tilde{U}$ is the vector of state quantities and $\tilde{F}, \tilde{G}$ are the flux vectors.

$$\tilde{U} = \begin{pmatrix} \rho \\ \rho u \\ \rho v \\ \rho E \end{pmatrix}$$

$$\tilde{F} = \begin{pmatrix} \rho u \\ p + \rho u^2 - \tau_{xx} \\ \rho uv - \tau_{xy} \\ \rho uH - (\tau_{xx} u + \tau_{xy} v) + q_x \end{pmatrix}$$

$$\tilde{G} = \begin{pmatrix} \rho v \\ \rho uv - \tau_{yx} \\ p + \rho v^2 - \tau_{yy} \\ \rho vH - (\tau_{yy} v + \tau_{yx} u) + q_y \end{pmatrix}$$

where $H = E + p/\rho$, the viscous stresses, τ, are modeled assuming a Newtonian fluid using Stokes's hypothesis as [73]:

$$\begin{aligned} \tau_{xx} &= 2\mu \left[\frac{\partial u}{\partial x} - \frac{1}{3} \nabla \cdot \vec{V} \right] \\ \tau_{yy} &= 2\mu \left[\frac{\partial v}{\partial y} - \frac{1}{3} \nabla \cdot \vec{V} \right] \\ \tau_{yy} &= 2\mu \left[\frac{\partial u}{\partial y} - \frac{\partial v}{\partial x} \right] \end{aligned} \tag{4.2}$$

where $\vec{V}$ is the bulk fluid velocity vector, μ is the coefficient of viscosity, q is the heat flux term which are modeled by Fourier's law as [73]:

$$\begin{aligned} q_x &= -k \frac{\partial T}{\partial x} \\ q_y &= -k \frac{\partial T}{\partial y} \end{aligned} \tag{4.3}$$

where k is the thermal conductivity which is determined from Eucken's relation as [70]:

$$k = \mu \left(\frac{5}{2} C_V^{tra} + C_V^{rot} \right) \tag{4.4}$$

where $C_V^{tra} = \frac{3}{2} R_{gas}$ and $C_V^{rot} = R_{gas}$ are the translational and rotational contributions to the specific heat of the gas at constant volume. Equations (4.1) to (4.2) are closed using the perfect gas equation of state,

$$p = \rho R_{gas} T \tag{4.5}$$

The Navier-Stokes equations are solved using the Michigan Aerothermodynamics Navier-Stokes (LeMANS) solver [56, 57]. LeMANS solves the laminar, compressible, Navier-Stokes equations using a finite volume method. LeMANS is able to simulate 2D, axi-symmetric and 3D flows on parallel computing architectures. Time integration of the governing equations uses a point-implicit method [55].

4.2 Initialization of the LD-DSMC Hybrid Simulation

A CFD-DSMC hybrid simulation starts its calculation from an initial CFD solution that provides the starting domain decomposition. By comparison, the LD-DSMC hybrid approach currently relies on a very expensive initial DSMC simulation to provide prediction of continuum breakdown. It means the whole computational domain is simulated by standard expensive DSMC until a first continuum breakdown can be evaluated. For the hypersonic flow studied here, the pure LD method is numerically unstable, so it does not provide a reliable way to initialize the computational domain. When a multiscale flow is simulated only with the DSMC method, the continuum regions will have many particles and collisions per cell. This is computationally expensive. Generally, several thousand steps are required until a first continuum breakdown evaluation can be performed. After initial continuum breakdown, the LD method is used for continuum cells and DSMC is used elsewhere. A more efficient way to operate the LD-DSMC hybrid method is to use the LD method in continuum regions from the startup of the simulation. To do this, an initial domain decomposition is needed and a CFD simulation is used to obtain it. CFD is not an adequate method to analyze multiscale flow which includes both equilibrium and nonequilibrium flow regions. However, it may provide the continuum regions correctly and give an approximate domain decomposition. The concept of initialization of various hybrid simulations is shown in Figure 4.1.

From the CFD solution, the domain is decomposed based on the gradient length local Knudsen number, $Kn_{GLL,max}$, which is explained in Equation 3.2. The local mean free path is calculated using the macroscopic properties in each cell as:

$$\lambda = \frac{2\left(5-2\omega\right)\left(7-2\omega\right)}{15}\sqrt{\frac{m}{2\pi kT}}\left(\frac{\mu}{\rho}\right) \tag{4.6}$$

where μ is the local viscosity computed using Equation (2.8). 0.05 is the reference

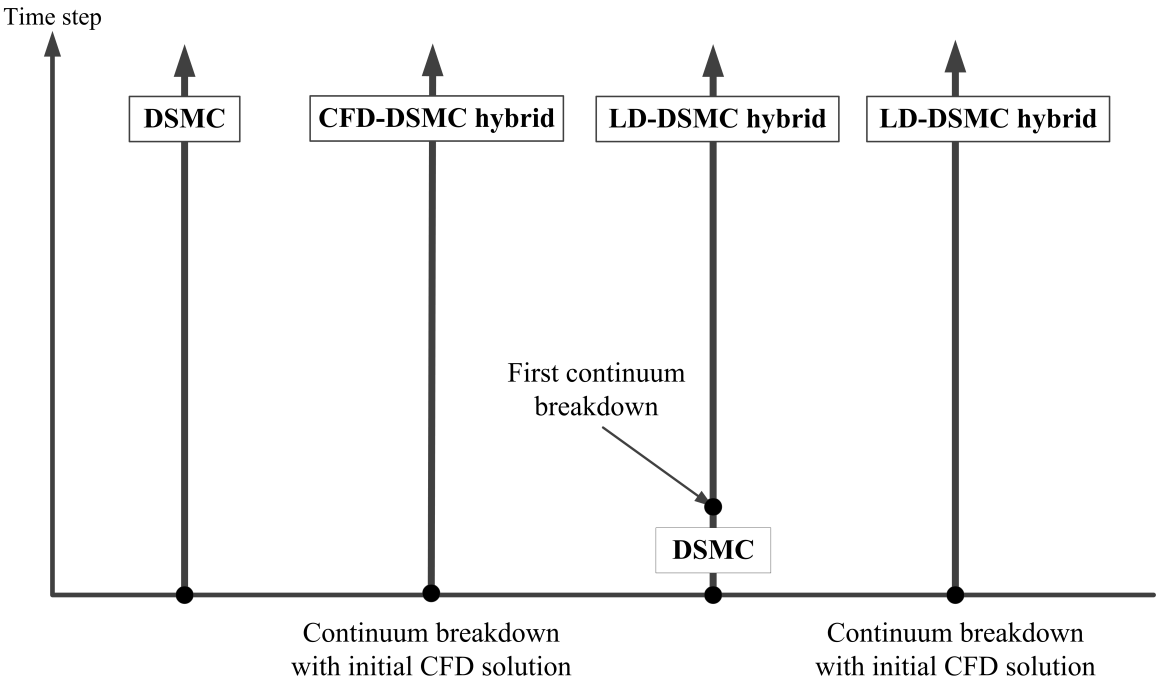

Figure 4.1: Concept of simulation procedures.

value of $Kn_{GLL,max}$ used to classify continuum or non-continuum cells. Regions for which $Kn_{GLL,max}$ is larger than 0.05 are assigned as a DSMC domain, and all other regions are assigned as LD domains. In the DSMC domain, a conventional CFD cell may be too large to satisfy the DSMC guideline that the cell size should be smaller than the mean free path. After LD/DSMC domain decomposition based on the CFD solution, therefore, the DSMC cells may need to be refined.

4.3 Mesh Refinement

After LD/DSMC domain decomposition, every quadrilateral CFD cell is classified as a DSMC or LD cell. Within the DSMC domains, the non-continuum cell-centered value of mean free path, λ, is compared to the length of each cell face in order to determine the refinement required in each cell of the initial CFD mesh. The mesh refinement restricts the cell size to λ in the direction of the flow gradient while 4λ

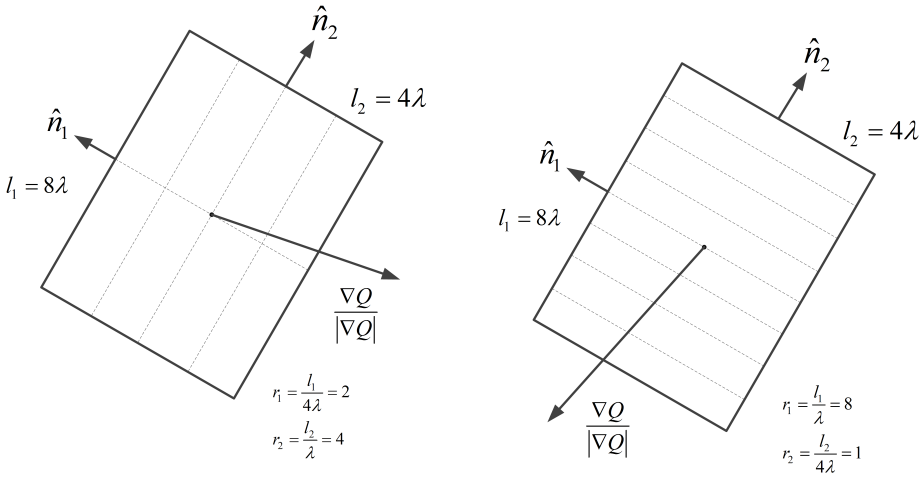

Figure 4.2: Mesh refinement procedure for each DSMC cell.

is allowed in the direction normal to the flow gradient. Figure 4.2 shows the mesh refinement according to the direction of the gradient [58].

The refinement factor, r_f, of each cell face is calculated as:

$$r_f = \left\lfloor l_f \times \left[F\lambda \left(3 \left| \hat{n}_f \cdot \frac{\nabla Q}{|\nabla Q|} \right| + 1 \right) \right]^{-1} \right\rceil \tag{4.7}$$

where l_f is the length of the cell face, $\frac{\nabla Q}{|\nabla Q|}$ is the unit gradient vector, and the dot product determines the alignment of the cell face with the direction of the gradient. For consistency with continuum breakdown, Q is calculated with the same flow quantities $\rho, T_{tra}, or\, |V|$ which are used for domain decomposition in Equation 3.2. F is the scaling factor used as a multiple of the local mean free path, λ. $\lfloor \rceil$ rounds to the nearest integer. Each non-continuum quadrilateral cell has two refinement factors, r_1, r_2, and the opposite faces should have the same refinement factor. Due to the fact that each cell face borders with another cell, the refinement factors must be consistent with the refinement in each neighboring cell.

Figure 4.3 shows a conceptual procedure of cell refinement. From the initial CFD structured grid, the cells are classified as continuum (LD) or non-continuum (DSMC) cells. Then, the DSMC cells are refined to satisfy DSMC guidelines. LD cells are left

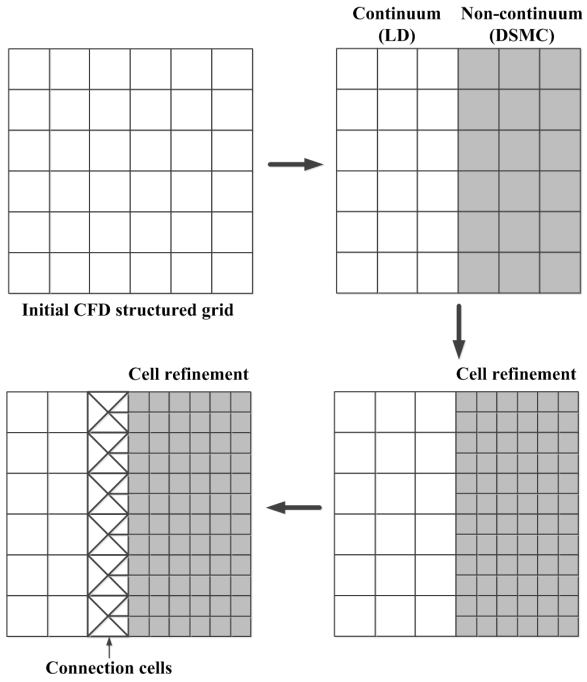

Figure 4.3: Procedure of cell refinement.

without refinement. After the cell refinement in the DSMC cells, connection cells are needed to connect to the LD cells. The connection cells consist of triangular cells, and the number of triangular cells in each connection cell depends on the refinement factor of the border face of the DSMC cell. The connection cell may have from 1 to 3 border faces. If the connection cell has 4 border faces, it automatically belongs to a DSMC region. The refinement of connection cells is depicted in Figure 4.4. The connection cells are assigned as LD cells.

Figure 4.5 shows the refined mesh for a LD-DSMC hybrid simulation. The region near the bow shock belongs to the non-continuum region, and it is refined to small cells while continuum regions are left as the initial LD cells. The cell refinement is based on the Navier-Stokes solution that cannot give an exact solution for the non-equilibrium region. So, during the hybrid LD-DSMC simulation, domain decomposition is re-evaluated periodically until a steady state is reached. Figure 4.6 shows an example of the initial domain decomposition based on CFD and the final domain decomposition based on LD-DSMC.

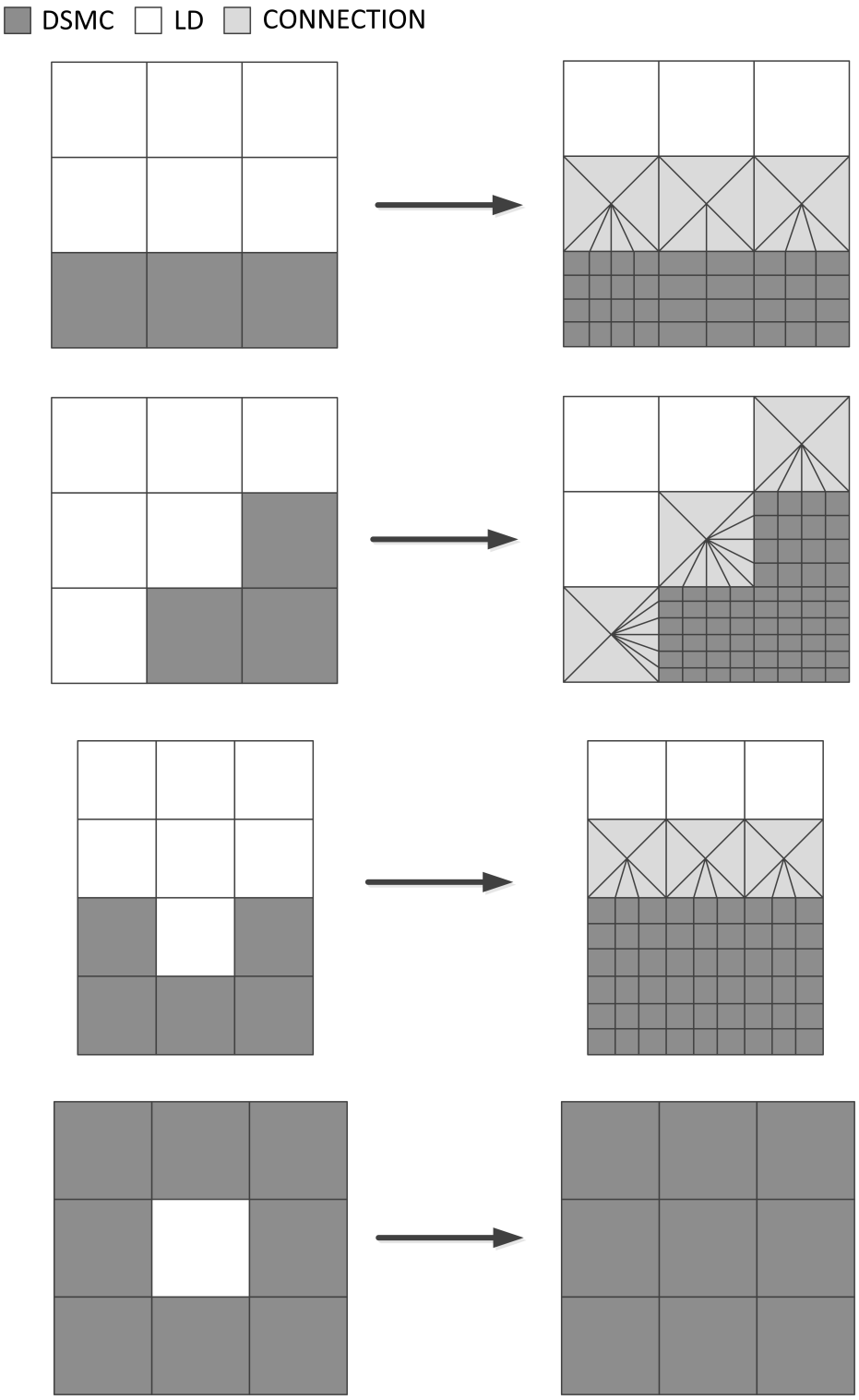

Figure 4.4: Connection cells between DSMC and LD.

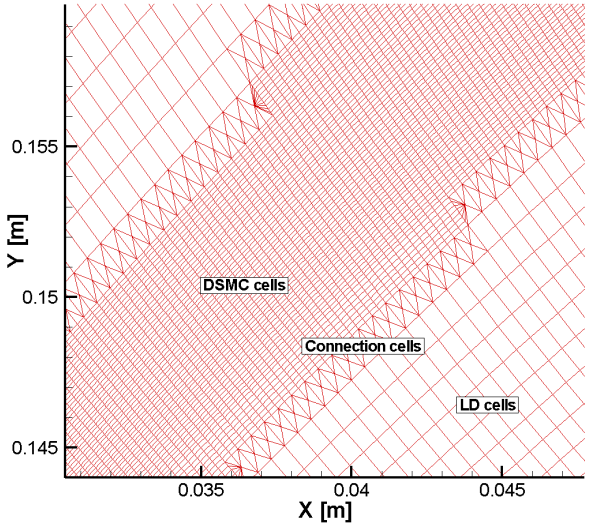

Figure 4.5: Refined mesh for the LD-DSMC hybrid simulation.

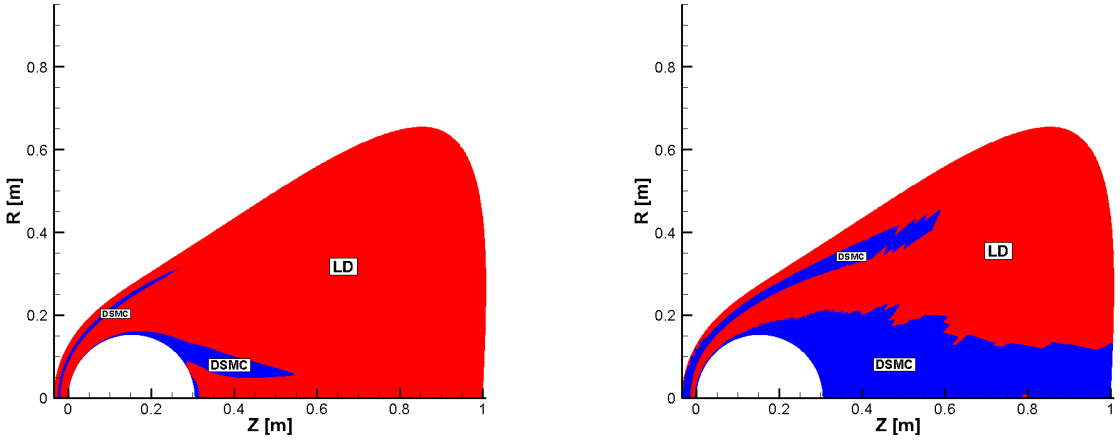

(a) Initial domain decomposition based on CFD.

(b) Final domain decomposition based on LD-DSMC.

Figure 4.6: Initial and final domain decomposition when the LD-DSMC hybrid simulation is initialized with CFD.

CHAPTER V

Application to Hypersonic Blunt Body Flows

As mentioned in the motivation, the LD-DSMC hybrid scheme is useful to analyze multiscale flows involving a wide range of Knudsen number. In this chapter, the LD-DSMC hybrid method is used to analyze flows around hypersonic blunt bodies. The LD method is used in continuum flowfield regions and the DSMC method is employed in nonequilibrium regions. The ultimate goal of this chapter is to validate the LD-DSMC hybrid method. First, the hypersonic flow over a sphere is simulated using standard DSMC, CFD, and the LD-DSMC hybrid method. The LD-DSMC results are compared with DSMC as well as CFD. The hybrid simulation is performed using a modified version of the DSMC code MONACO [11], and CFD flow simulation is performed using the LeMANS code developed at the University of Michigan [55]. Next, the hypersonic entry flow over the Mars Pathfinder (MPF) is simulated. The numerical sensitivities of the LD-DSMC hybrid method are discussed. Finally, LD-DSMC initialized with a Navier-Stokes solution is validated for hypersonic flow over the sphere. The results are compared with the conventional LD-DSMC hybrid method, and computational efficiency is discussed.

5.1 Hypersonic Flow over a Sphere

Standard DSMC, LD-DSMC, and CFD calculations are performed for pure nitrogen hypersonic flow over a 12 inch diameter sphere including the wake region. The purpose of this study is to validate the LD-DSMC method by comparing it to two other methods. Flowfield contours, and surface properties are used to validate the LD-DSMC method. Profiles of flow properties along extracted lines and wake rarefaction effects are also discussed.

5.1.1 Flow Conditions and Grid Configurations

Kn_∞	Mass Density $[Kg/m^3]$	Number Density [particles/m^3]	Mean Free Path [m]
0.002	9.875×10^{-5}	2.214×10^{21}	6.096×10^{-4}

Table 5.1: Simulation flow properties for N_2 hypersonic flow over a sphere.

Nitrogen flow over a 12 inch diameter sphere at Mach number 10 is studied. The free stream temperature is 200 K giving a free stream velocity of 2880 m/s. The surface of the sphere has a fixed temperature of 500 K. The mass density, number density and mean free path are given in Table 5.1. The Knudsen number is calculated using the sphere diameter as the characteristic length and the hard sphere model is used to determine the mean free path. For both standard DSMC and the LD-DSMC simulations, the same physical models are employed. Molecular collisions are simulated using the variable hard sphere (VHS) model with a reference temperature of 273 K and a viscosity temperature exponent of 0.75. The no-time-counter (NTC) scheme of Bird is used to select DSMC collision pairs during each time step. Translational-rotational energy exchange during simulated DSMC collisions is determined using the Larsen Borgnakke statistical model along with the total collision energy model of Boyd [10, 64]. The current solutions are obtained without chemical reactions.

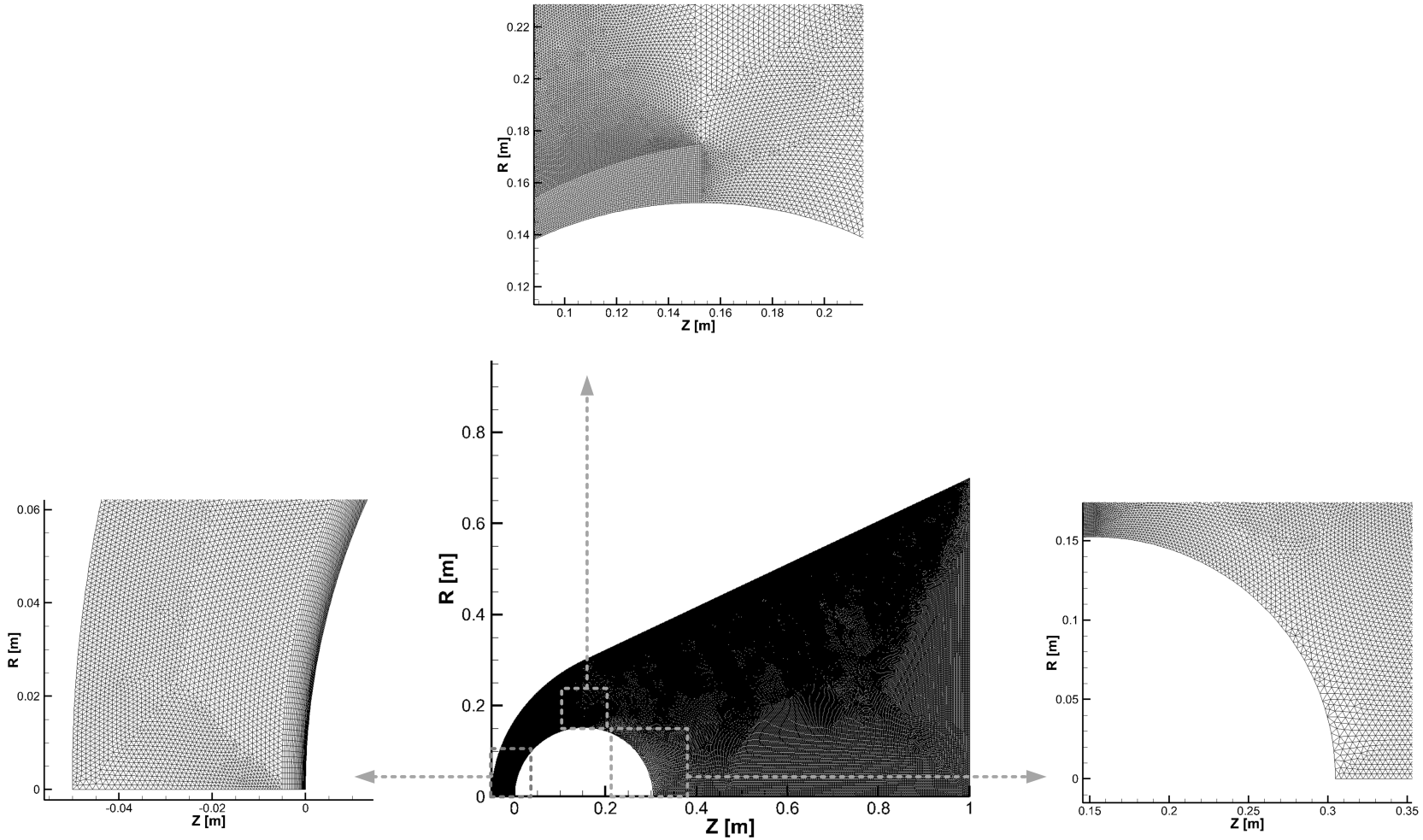

Figure 5.1: Grid configuration for hypersonic flow over a sphere.

Cases	Total cells	Representative method according to the regimes	
		Continuum	Non-continuum
Standard DSMC	1,1071,858	DSMC	DSMC
CFD,slip	100,000	CFD	CFD
LD-DSMC	234,256	LD	DSMC

Table 5.2: Simulation cases of N_2 hypersonic flow over a sphere.

A hybrid mesh is used in which a structured grid is employed along the fore body surface while an unstructured grid is used elsewhere in the flow field (Figure 5.1). For the structured grid, cell stretching is employed to provide enough particles per cell near the stagnation point. This is a useful technique in axisymmetric simulations, where it is often difficult to achieve a sufficiently large number of particles per cell near the axis.

5.1.2 Comparing DSMC, LD-DSMC, and CFD

Three simulations are performed: (1) a standard DSMC simulation, (2) a CFD simulation solving the Navier-Stokes equations; and (3) a LD-DSMC simulation. The simulation cases are summarized in Table 5.2

At LD-DSMC simulation startup, the entire flow field is assigned to the DSMC domain. A continuum breakdown parameter based on density, temperature and velocity gradients is then periodically evaluated in all cells within the computational grid. Breakdown parameter values are compared with a cutoff value to determine whether each cell should be assigned to DSMC or LD domains; when the parameter value is larger than 0.05 in a given cell, continuum breakdown is assumed and the cell is assigned to the DSMC domain.

Figure 5.2 shows continuum breakdown domain boundaries based on the maximum gradient length Knudsen number, $Kn_{GLL,max}$, from Equation (3.2). The upper half is from DSMC and the lower half is from the LD-DSMC hybrid simulation. The LD domain includes near-equilibrium regions in the freestream and aftershock, whereas

the DSMC domain comprises the remaining portions of the bow shock and wake where a high degree of nonequilibrium is observed. The initially designated cells are extended using a smoothing procedure and extra cells are employed to manipulate domain boundaries.

Figures 5.3 and Figures 5.4 show the velocity contours from DSMC, LD-DSMC hybrid, and CFD. Streamlines show generally expected trends with bending at the shock front. The flow separates from the rear surface, and a wake forms. In Figures 5.3, the upper half is simulated by the standard DSMC scheme and the lower half is simulated by the LD-DSMC hybrid method. Very good agreement is observed between standard DSMC and the LD-DSMC hybrid results. For example, the shock standoff distance and shock shapes are nearly identical in the solutions. In the hybrid method, the detached bow shock is simulated in the DSMC domain, and the boundary layer near the sphere surface is also assigned to DSMC. The flow in the wake of a hypersonic blunt body involves highly rarefied conditions, so this region is also assigned as a DSMC domain. The freestream and high density post shock regions are assigned to the LD domain. In Figures 5.4, the upper half is simulated by the LD-DSMC hybrid method and the lower half is simulated by CFD with slip boundary condition. Generally, since DSMC is a particle method with accuracy in both the continuum and the rarefied regimes, it is assumed in this study that the DSMC result is the most accurate. At the global Knudsen number of 0.002, the flow is expected to be well within the continuum regime. Therefore, CFD should have no problem to accurately simulate this flow. This is verified by Figures 5.4 especially near the forebody.

The wake stagnation point for axisymmetric flows is the location along the wake symmetry axis where the velocity is zero. The effect of rarefaction on the location of the wake stagnation point is shown in Figures 5.5. Two arrows indicate the size of the recirculation region for DSMC, LD-DSMC and CFD. The recirculation region exists

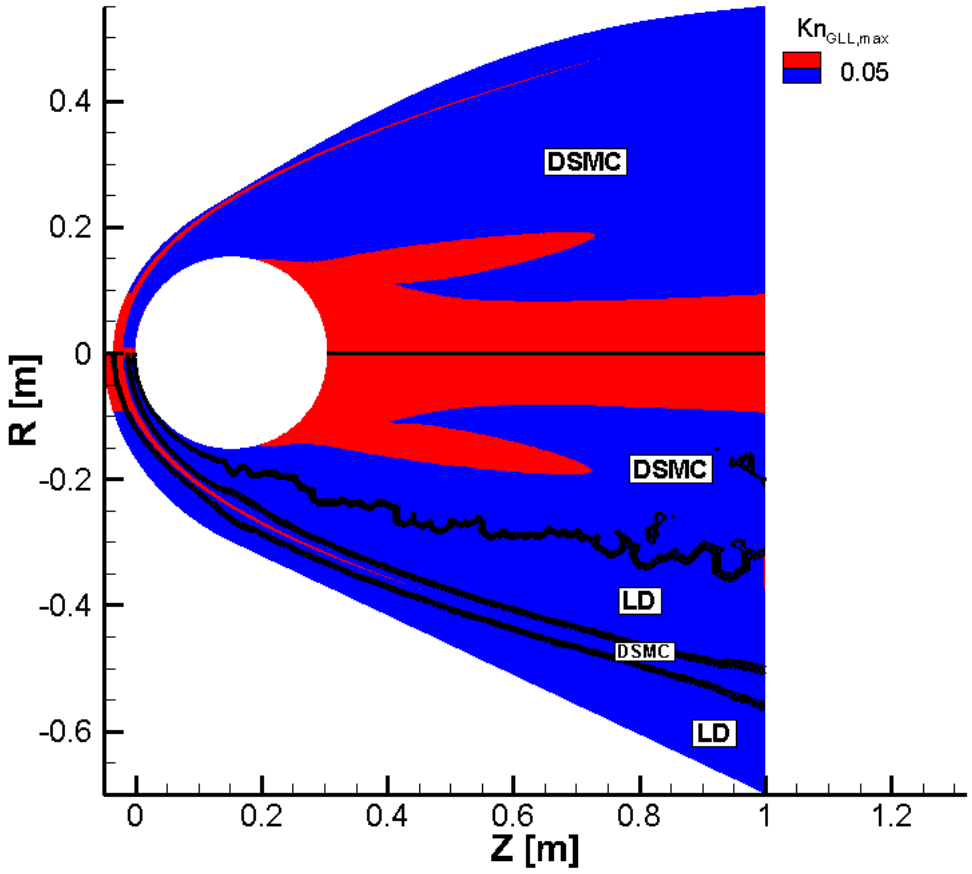

Figure 5.2: Contours of maximum gradient length local Knudsen number, $Kn_{GLL,max}$, and domain decomposition region (upper: DSMC, lower: LD-DSMC hybrid).

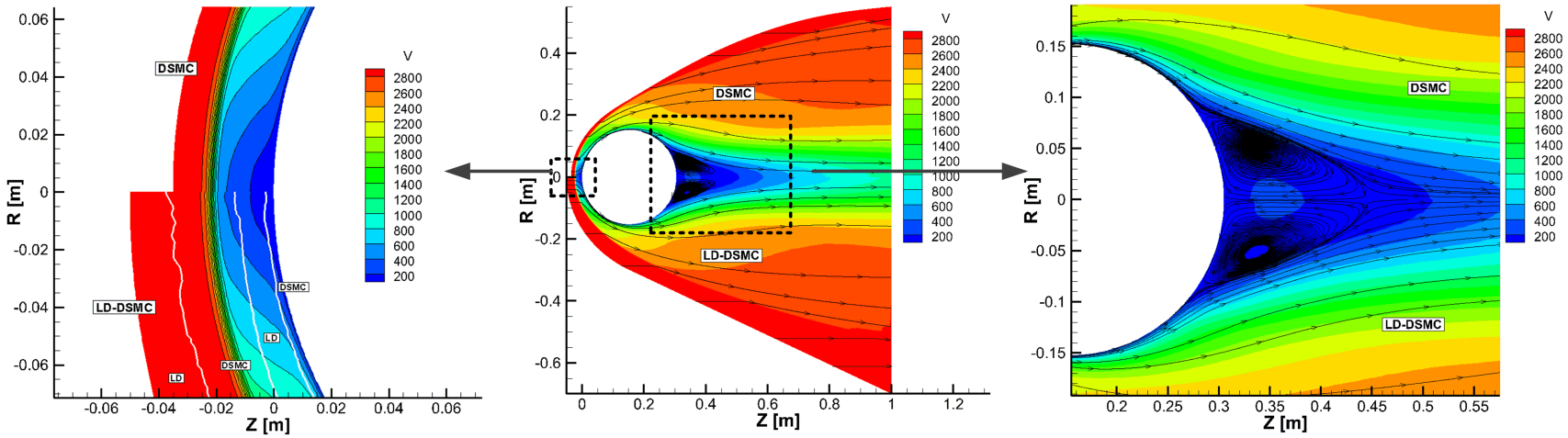

Figure 5.3: Velocity contours and recirculation region from DSMC (upper) and LD-DSMC (lower) $[m/s]$.

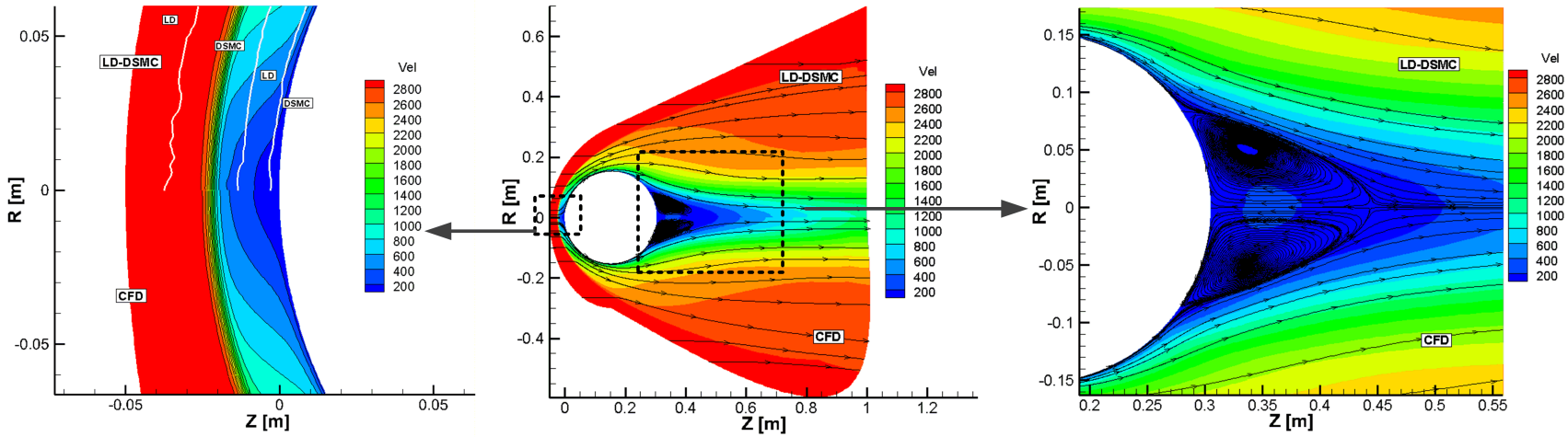

Figure 5.4: Velocity contours and recirculation region from LD-DSMC (upper) and CFD (lower) $[m/s]$.

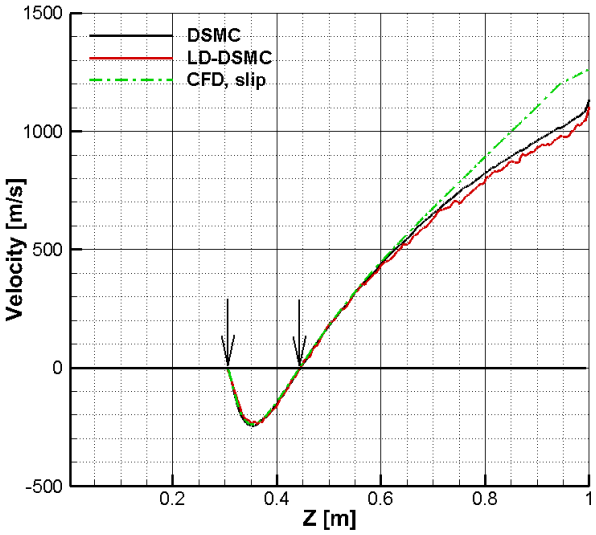

Figure 5.5: Velocity profiles along the wake axis (black solid line: DSMC, red solid line: LD-DSMC, green dash line: CFD, slip).

between 0.3014m and 0.4433m, and all 3 cases have almost the same recirculation size. This implies that there exists a large stable vortex behind the sphere at Mach 10 and Knudsen number 0.002 flow conditions. However, CFD may be inaccurate in the wake where a highly rarefied region exists. To see this, the effect of rarefaction on wake structure will be discussed later.

Pressure contours are shown in Figure 5.6. Figure 5.6(a) represents results from the DSMC simulation and LD-DSMC. Throughout the entire computational domain, the two simulations are nearly indistinguishable within the resolution of the figure. Figure 5.6(b) represents results from the LD-DSMC simulation and CFD. Distinct differences are observed in the wake region. In Figure 5.7, mass density contours for the overall the computational domain are compared. A narrow region of increased density along the shock is observed, arising from post-shock compression. For the DSMC and LD-DSMC solutions, shown in Figure 5.7(a), very good agreement is observed. On the other hand, Figure 5.7(b) shows density contours of LD-DSMC and CFD. Differences are observed, especially in the wake region.

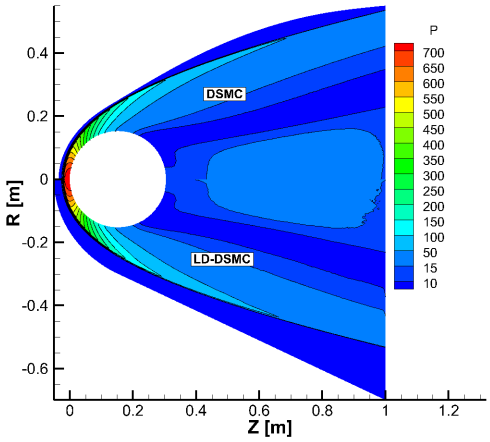

(a) upper: DSMC, lower: LD-DSMC.

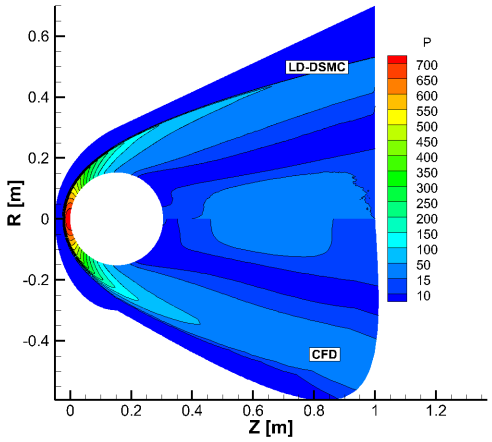

(b) upper: LD-DSMC, lower: CFD.

Figure 5.6: Pressure contours of N_2 hypersonic flow over a sphere [Pa].

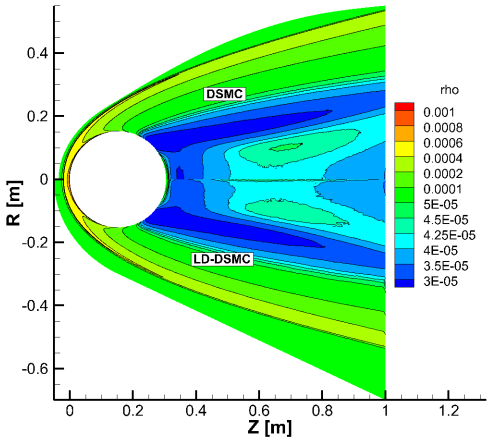

(a) upper:DSMC, lower:LD-DSMC.

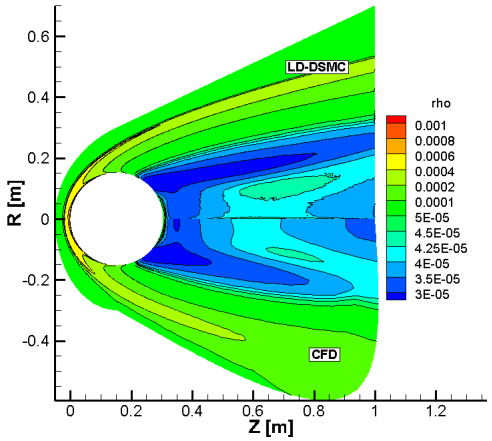

(b) upper:LD-DSMC, lower:CFD.

Figure 5.7: Density contours of N_2 hypersonic flow over a sphere $[kg/m^3]$.

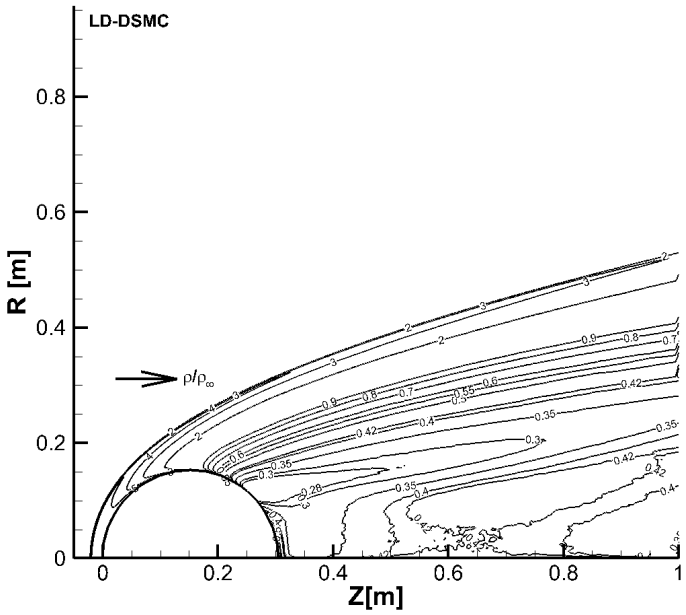

Figure 5.8: Selected contours of nondimensional density from the LD-DSMC simulation.

To see the effects of rarefaction in the wake, normalized density is shown in Figures 5.8 and 5.9. Normalized density contours (Figure 5.8) show evidence of a weak wake shock. Figure 5.9 presents radial profiles for normalized density at three axial locations: location a (Z=0.1524m) corresponds to the maximum radial dimension of the sphere, location b (Z=0.2286m) is on the afterbody, and location c (Z=0.35m) is in the near wake. The near wake region is shadowed by the forebody ($R/R_B < 1.0$) and the density is generally less than 50% of the freestream value at locations b and c. The results from DSMC and LD-DSMC are almost identical while the CFD results cannot perfectly capture the gradient in the bow shock. CFD predicts a wider shock and less peaked density.

Contours of translational and rotational temperatures are shown in Figure 5.10. Rotational temperature is presented to demonstrate the presence of rotational-translational nonequilibrium. Very good overall agreement is obtained between the standard DSMC

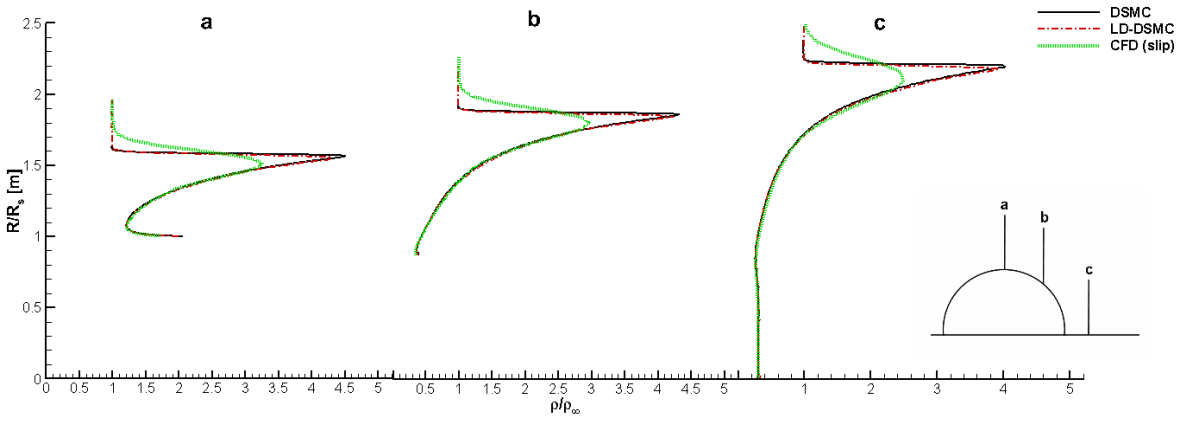

Figure 5.9: Non-dimensional density profiles of DSMC, LD-DSMC and CFD results at the wake region.

and LD-DSMC results for the translational and rotational temperature contours, as shown in Figures 5.10(a) and 5.10(c) while the CFD rotational temperatures are noticeably different in the wake. Within this region, the translational temperature of CFD is underestimated near the wake stagnation line. The disagreement of the rotational temperature between LD-DSMC and CFD stands out in the wake region where the continuum assumption breaks down.

Figure 5.11 presents a comparison of radial profiles for translational temperature at three axial locations of the after body. These are the same locations used with Figure 5.9. Radial translational temperature profiles show good agreement between DSMC and LD-DSMC, as expected. CFD profiles show the same trends as Figure 5.9. The bow shock is too wide and a noticeable difference is observed in location c of the wake region. This discrepancy clearly indicates that the Navier-Stokes formulation becomes inaccurate in the wake, where the flow is very rarefied.

Figure 5.12 shows comparisons of translational, rotational, and vibrational temperatures in the wake. When the flow meets the shock, both the translational and rotational temperatures suddenly increase while the vibrational temperature stays near zero. Translational-rotational equilibrium is reached in the bow shock, where

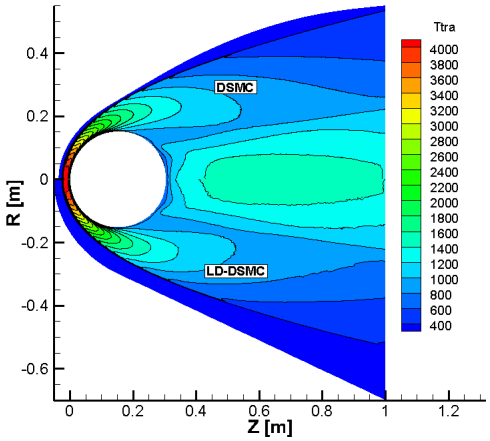

(a) Translational temperature (upper:DSMC, lower:LD-DSMC).

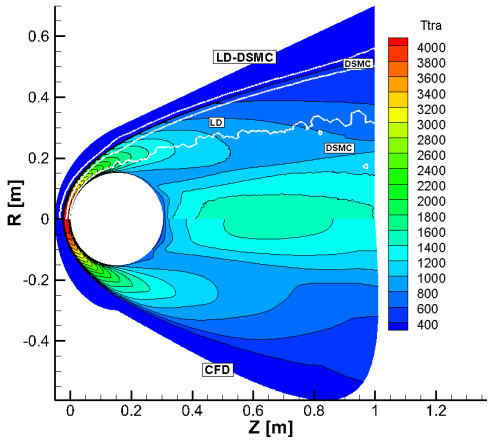

(b) Translational temperature (upper:LD-DSMC, lower:CFD).

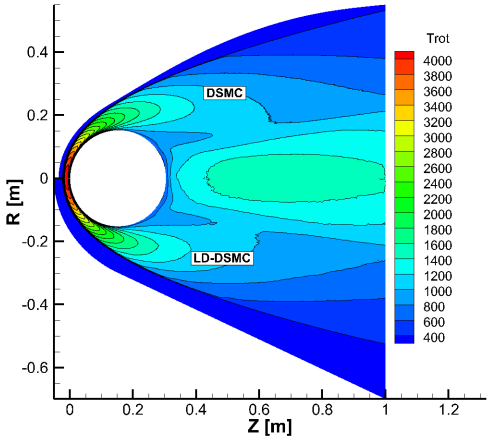

(c) Rotational temperature (upper:DSMC, lower:LD-DSMC).

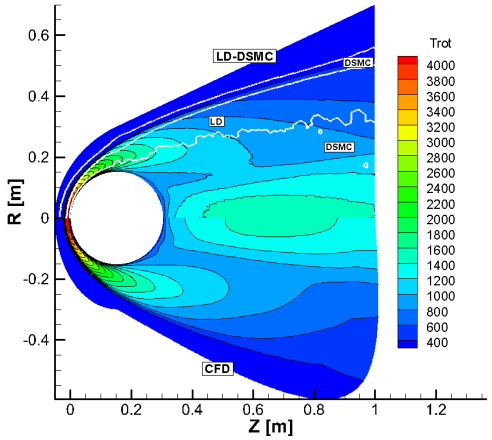

(d) Rotational temperature (upper:LD-DSMC, lower:CFD).

Figure 5.10: Temperature contours of N_2 hypersonic flow over a sphere [K].

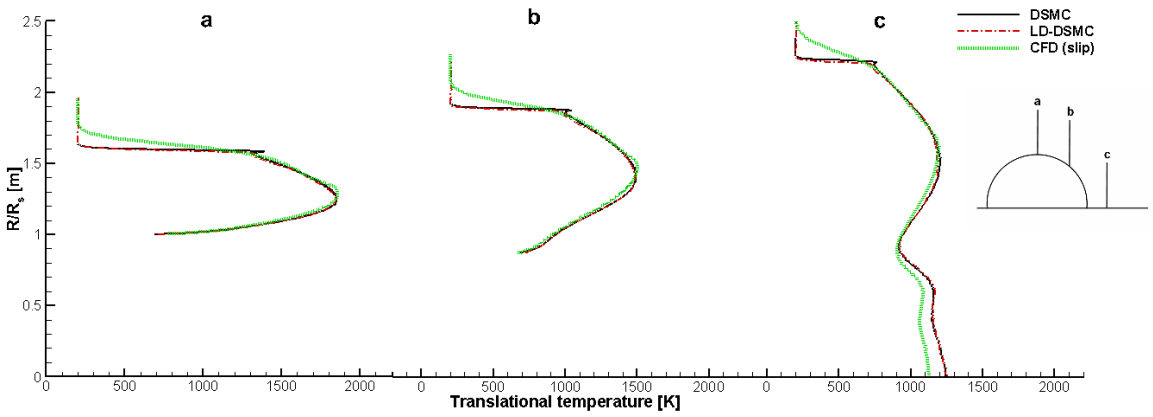

Figure 5.11: Translational temperature profiles of DSMC, LD-DSMC and CFD results near the wake region.

the intermolecular collision frequency is sufficiently high to prevent any significant rotational temperature lag. On the other hand, the flow is in a state of weak thermal-nonequilibrium near the wake. The local maximum translational temperature approaches 4700 K. For this flow condition, the vibrational energy mode of N_2 is not fully excited. It is shown as the green lines in Figures 5.12(a) and 5.12(b).

Figure 5.13(a) shows contours of the number of particle per cell and Figure 5.13(b) shows contours of weight scaling factor. For DSMC, constant weight scaling factor bands are used while adaptive weight scaling factors are used in the LD-DSMC hybrid simulation. This procedure is explained in Chapter 3.4.2. Based on the adaptive weight scaling factors, the number of particles per cell is effectively retained around 30 over most of the computational domain.

The high temperature region is focused near the forebody which has a more severe flow condition. This region is considered as key to the design of an effective and survivable entry probe. Since the physical properties are most severe at the stagnation point, it is useful to investigate the profiles along the stagnation streamline. Profiles of the temperature, bulk velocity and mass density along the stagnation streamline are shown in Figure 5.14. The vertical dotted line denotes the boundaries of the

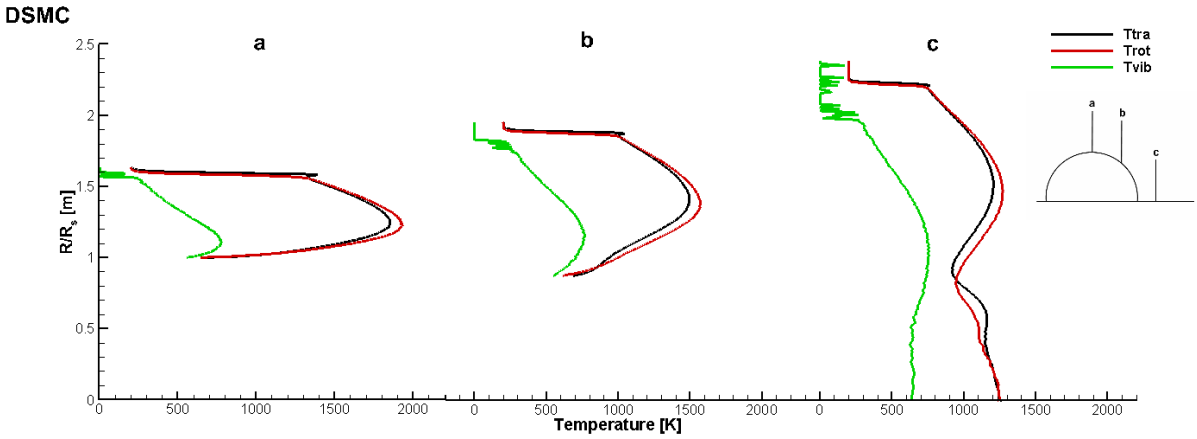

(a) Wake temperature profiles of DSMC

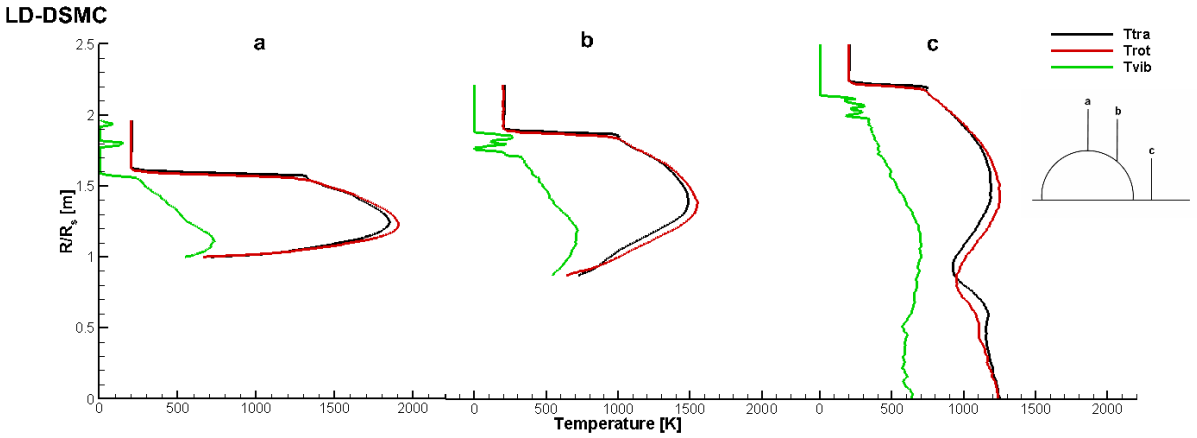

(b) Wake temperature profiles of LD-DSMC

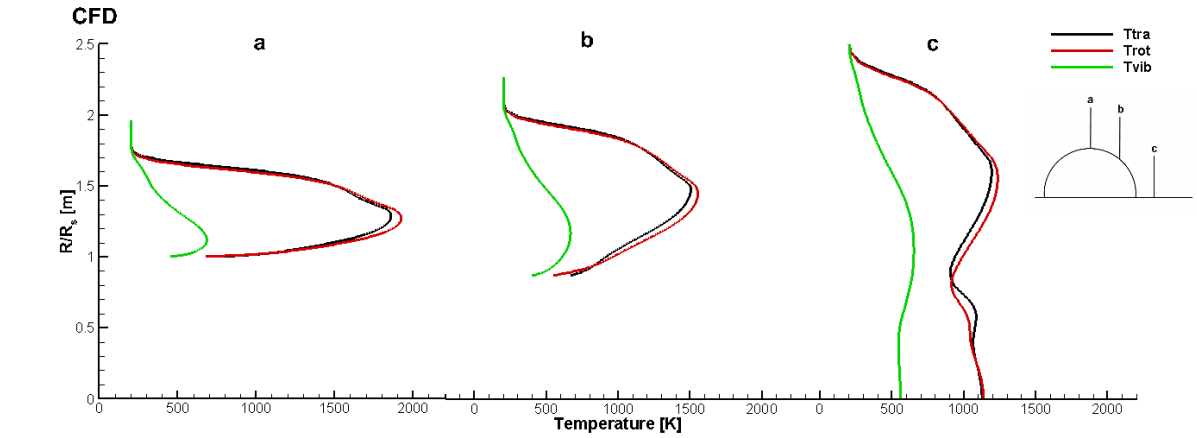

(c) Wake temperature profiles of CFD

Figure 5.12: Vertical temperature profiles in the wake.

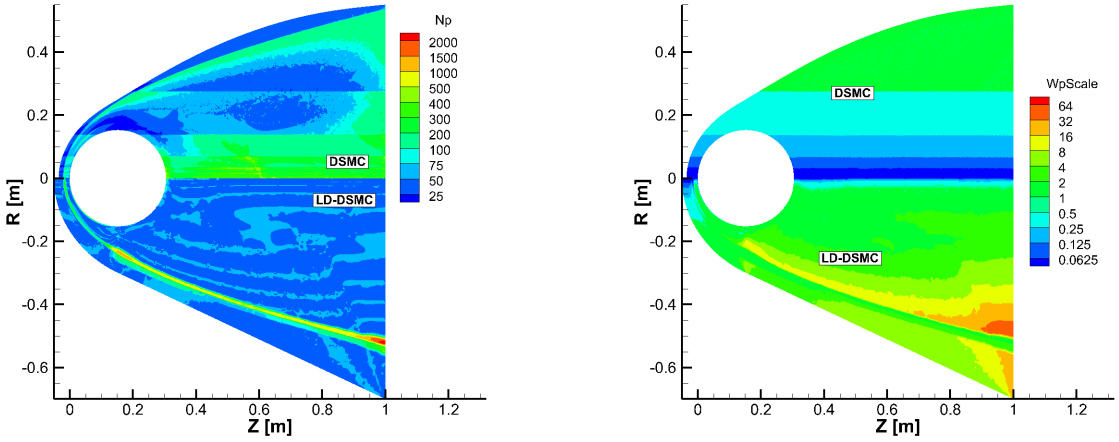

(a) Number of particles per cell (upper: DSMC, lower: LD-DSMC).

(b) Wieght scaling factor (upper: DSMC, lower: LD-DSMC).

Figure 5.13: Number of particles per cell and weight scaling factor.

LD and DSMC regions. As expected, the DSMC domain of the hybrid simulation includes high gradient regions within the shock and near the sphere surface. Excellent agreement is obtained between the DSMC and LD-DSMC simulations, while CFD cannot perfectly capture the strong gradient in the bow shock. The shock is predicted to be slightly thicker in the DSMC and LD-DSMC solutions in comparison to CFD, and the CFD solution predicts a lower peak translational temperature in the shock.

Figures 5.15 and 5.16 show profiles of temperature, bulk velocity and mass density along lines inclined at 60° and 120° from the freestream direction. Similar to the profiles along the stagnation line, the DSMC and LD-DSMC results agree well while the CFD results have significant discrepancies.

Accurate prediction of surface properties is often the most important aspect of these types of computations for hypersonic vehicle design. Figure 5.17 shows profiles along the sphere surface of heat flux and pressure, respectively. Black and red solid lines represent DSMC and LD-DSMC, respectively, and dotted lines denote CFD results. The maximum gradient length local Knudsen number, $Kn_{GLL,max}$, is also shown along the sphere surface. After 90 degrees, $Kn_{GLL,max}$ increases, which means

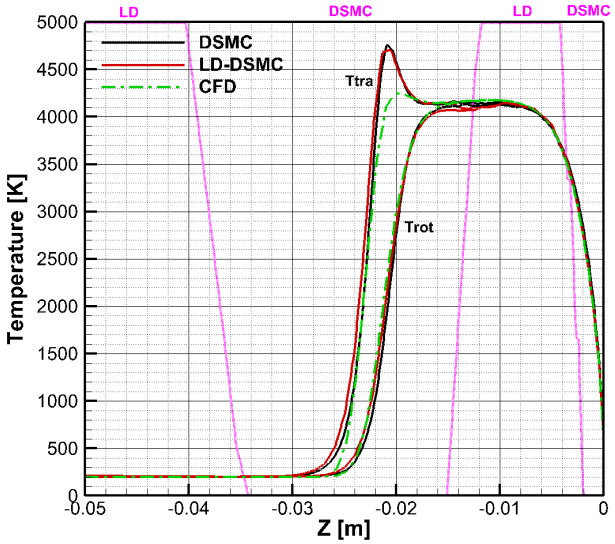

(a) Profiles of temperatures along the stagnation line.

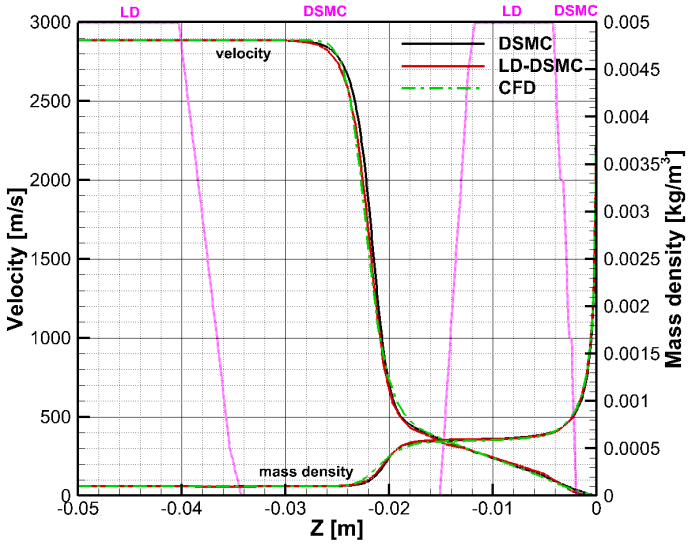

(b) Profiles of bulk velocity and mass density along the stagnation line.

Figure 5.14: Profiles along the stagnation line: black solid and red solid lines represent DSMC and LD-DSMC hybrid results, respectively. Dotted green lines denote CFD results.

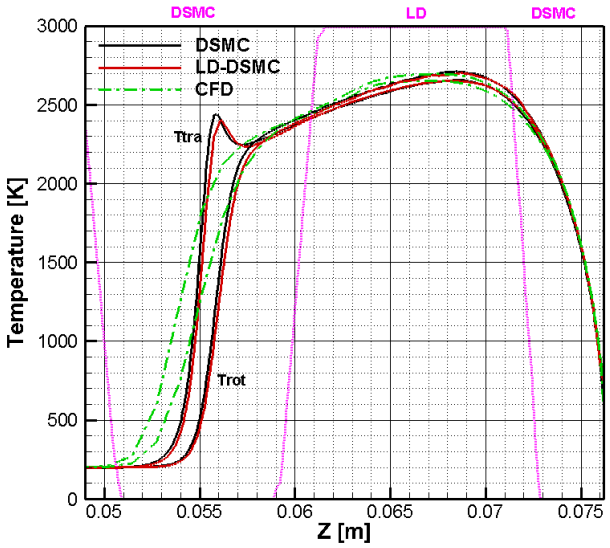

(a) Profiles of temperatures along an extraction line inclined 60° from the freestream direction.

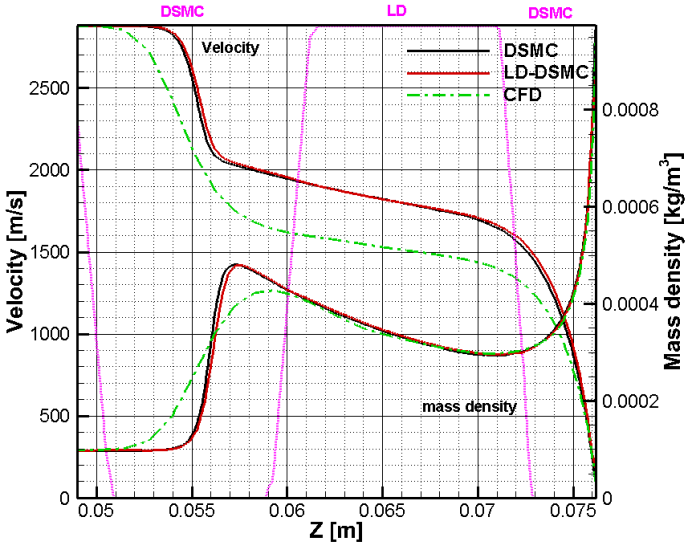

(b) Profiles of bulk velocity and mass density along an extraction line inclined 60° from the freestream direction.

Figure 5.15: Profiles along an extraction line inclined 60° from the freestream direction: black solid and red solid lines represent DSMC and LD-DSMC hybrid results, respectively. Dotted green lines denote CFD results.

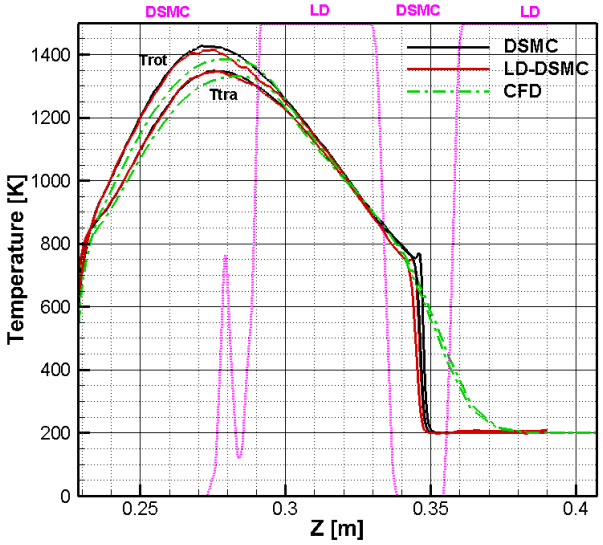

(a) Profiles of temperatures along an extraction line inclined 120° from the freestream direction.

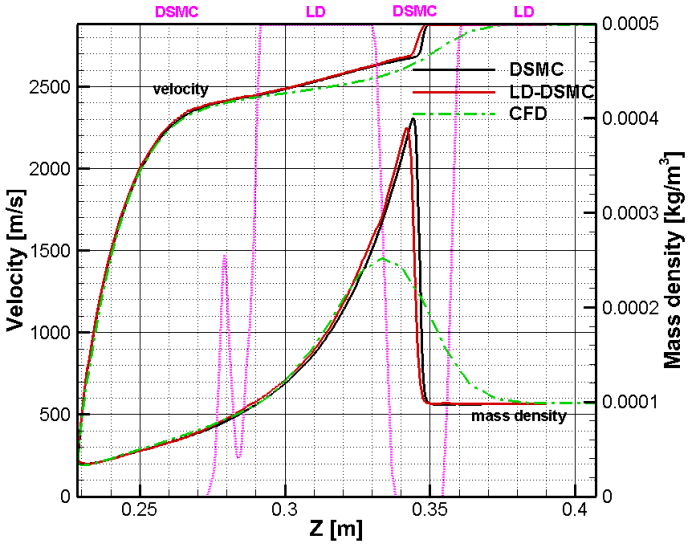

(b) Profiles of bulk velocity and mass density along an extraction line inclined 120° from the freestream direction.

Figure 5.16: Profiles along an extraction line inclined 120° from the freestream direction: black solid and red solid lines represent DSMC and LD-DSMC hybrid results, respectively. Dotted green lines denote CFD results.

continuum breakdown occurs. The CFD results show obvious differences where the continuum assumption fails, i.e. in the low-density recirculation region. The DSMC and the LD-DSMC hybrid methods show excellent agreement. The heat flux results contain scatter near the stagnation point. To reduce the statistical noise, the stagnation point heat flux is averaged over the first ten cells along the surface. The stagnation point heat transfer coefficient and total drag coefficient are calculated according to Equations (5.1).

$$C_D = \frac{2D}{\rho V_\infty^2 S}$$
$$C_H = \frac{2q}{\rho V_\infty^3} \tag{5.1}$$

In Table 5.3, peak heating, heat flux coefficient, total drag, and drag coefficients are compared. The LD-DSMC hybrid method agrees with DSMC to within 5%. In general, the use of a cutoff value of the continuum breakdown parameter of 0.05 aims to provide agreement between DSMC and the Navier-Stokes equations to within 5%, so the level of agreement achieved here is considered more than acceptable.

	Standard DSMC	LD-DSMC hybrid	CFD, slip
q, W/m^2	115000	116000 (0.862%)	113000 (-1.74%)
C_H	0.0974	0.0976 (0.205%)	0.0951 (-2.36%)
Drag, N	29.0	29.0 (0.00%)	28.9 (-0.345%)
C_D	0.968	0.967 (-0.103%)	0.965 (-0.310%)

Table 5.3: Comparison of surface properties.

Figure 5.18 shows percent errors of the LD-DSMC and CFD solutions in comparison to DSMC along the surface. As mentioned above, the DSMC result is considered the most accurate and CFD (Navier-Stokes formulation) becomes inaccurate in the wake where the flow is very rarefied which explains the significant differences (30%) in those results. The LD-DSMC hybrid simulation agrees with standard DSMC within

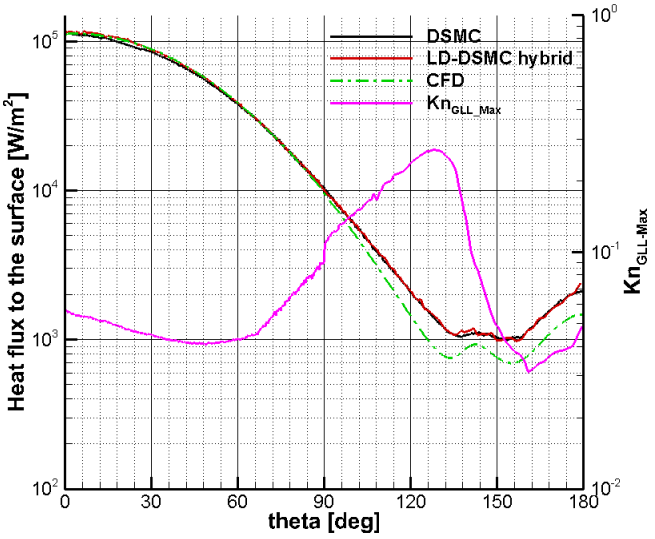

(a) Heat flux to the surface and $Kn_{GLL_{Max}}$.

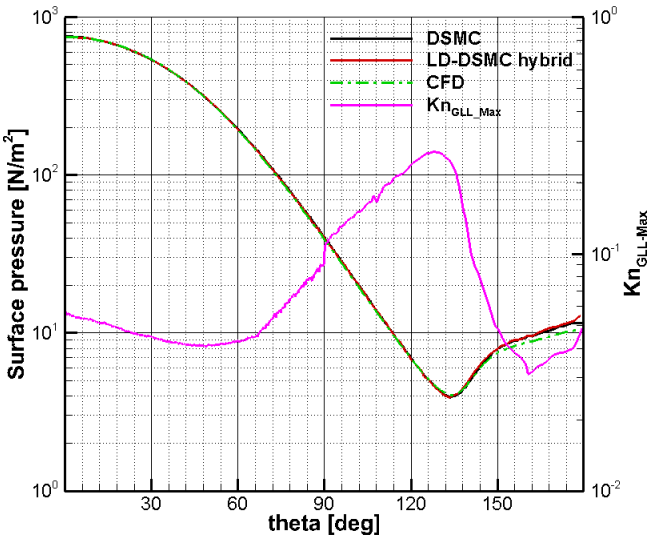

(b) Surface pressure and $Kn_{GLL_{Max}}$.

Figure 5.17: Profiles along the sphere surface from DSMC, LD-DSMC, and CFD.

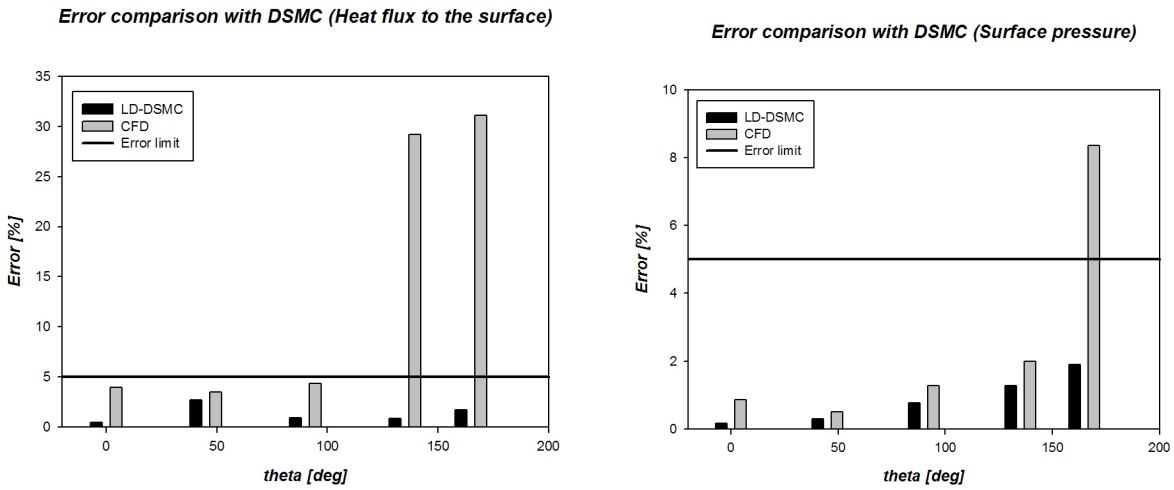

(a) Error comparison of heat flux to the surface.

(b) Error comparison of surface pressure.

Figure 5.18: Error comparisons of DSMC, LD-DSMC, and CFD for surface properties of N_2 hypersonic flow over a sphere.

the target error limit of 5%.

5.1.3 Study of Viscous Effects in the LD region

In Chapter 3.3.1, a viscous modification of the LD method is discussed. A finite volume discretization of the viscous term in the compressible Navier-Stokes equations is integrated into the LD particle method procedures, so that the method may be applied to low Knudsen number flows that include boundary layers, or other regions involving large transverse gradients. In this Chapter, the results of the LD-DSMC hybrid simulation which does not consider the viscous effects is compared to ascertain the importance of the viscous modification.

Figures 5.19 and 5.20 show the mass density, and translational and rotational temperature contours. The upper half is simulated with the standard LD-DSMC hybrid method, and the lower half is simulated with the LD-DSMC hybrid method ignoring the viscous effect. Significant differences are observed in the wake region. The discrepancy is detailed in profiles along several extraction lines in Figures 5.21, 5.22, and 5.23.

Figure 5.21 shows profiles along the stagnation line. Differences are observed in the LD region after the shock. The difference extends to the boundary layer where the DSMC method is designated as the simulation method. In these results, some disagreement is observed between the translational and rotational temperature profiles from the two simulations near the downstream edge of the shock, with a particularly large discrepancy in the post-shock LD region (Figure 5.21(a)). These differences may be related to viscous transport calculations in the LD method. Also, the differences are significant in bulk velocity but mass density still agrees quite well (Figure 5.21(b)). Generally, mass density is a less sensitive variable in the sampling process.

Figures 5.22 and 5.23 show profiles along extraction lines inclined at 60° and 120° from the freestream direction, respectively. Differences are observed near the LD/DSMC domain boundaries and they are perpetuated into the DSMC region. When the viscous effect is not considered in the LD region, the discrepancy affects the flow where the DSMC method is designated as the simulation method. Figures 5.24(a) and 5.24(b) show profiles along the sphere surface. Significant differences are observed in the heat flux to the surface while surface pressures agree quite well. The errors are compared in Figures 5.24(c) and 5.24(d). The differences are higher than the target error limit, 5%, and reach levels as high as 18%.

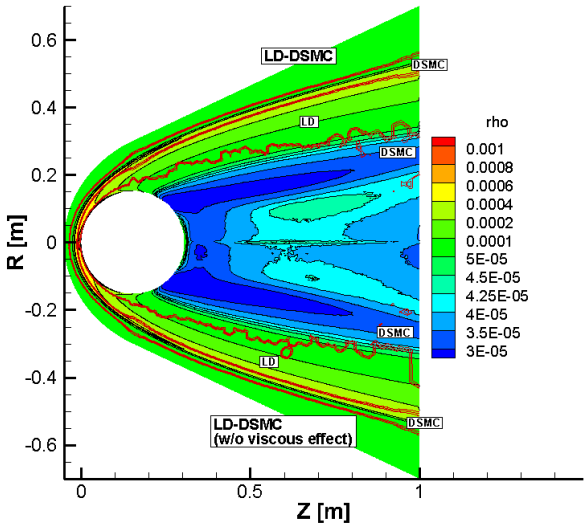

Figure 5.19: Density contours from LD-DSMC with and without viscous effects $[kg/m^3]$.

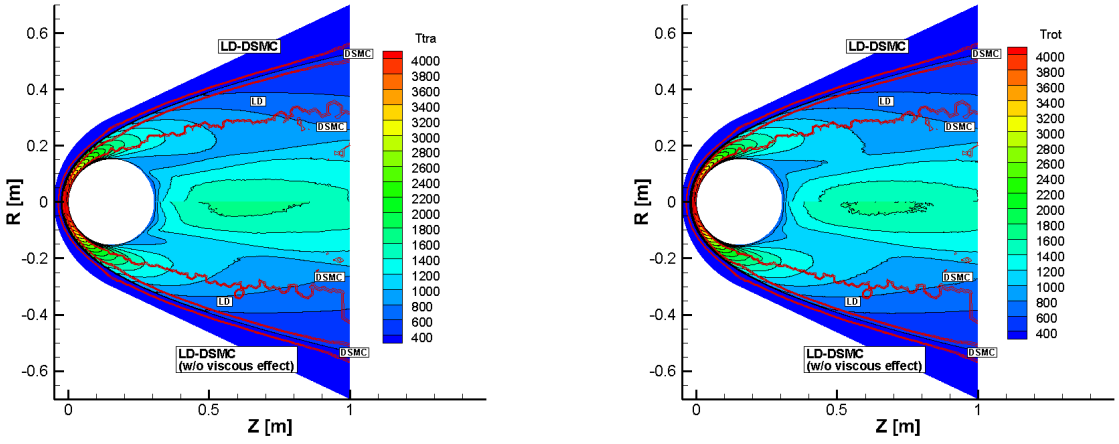

(a) Translational temperature.

(b) Rotational temperature.

Figure 5.20: Temperature contours with and without viscous effects [K].

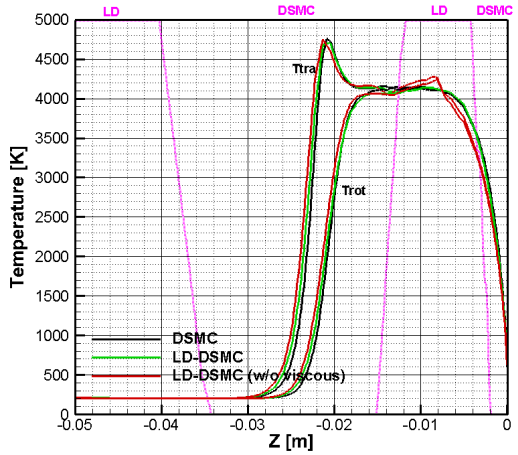

(a) Profiles of temperature along the stagnation line.

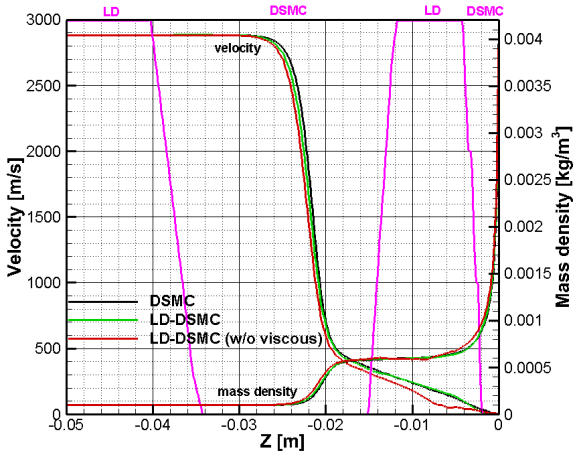

(b) Profiles of bulk velocity and mass density along the stagnation line.

Figure 5.21: Profiles along the stagnation line: black line represents DSMC, green and red lines represent LD-DSMC with and without viscous effects, respectively.

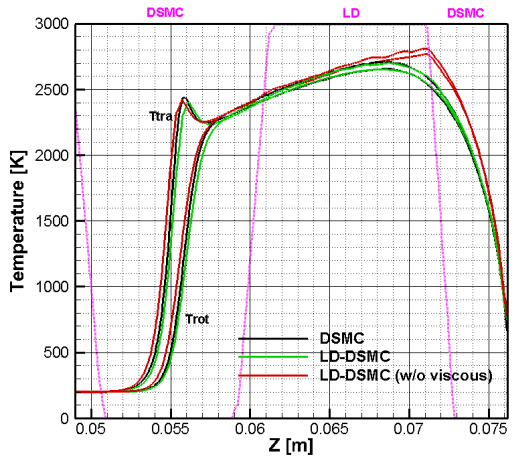

(a) Profiles of temperatures along an extraction line inclined 60° from the freestream direction.

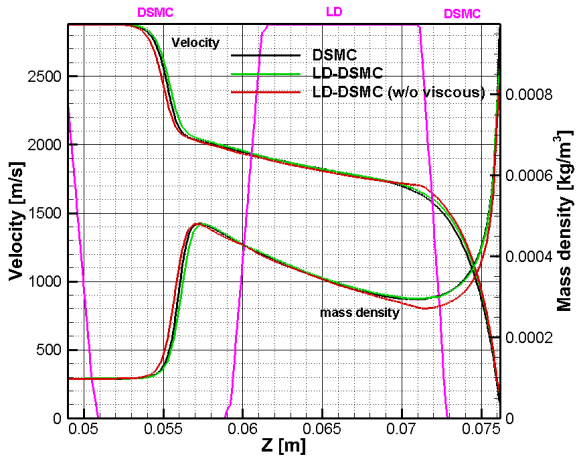

(b) Profiles of bulk velocity and mass density along an extraction line inclined 60° from the freestream direction.

Figure 5.22: Profiles along an extraction line inclined 60° from the freestream direction: black line represents DSMC, green and red lines represent LD-DSMC with and without viscous effects, respectively.

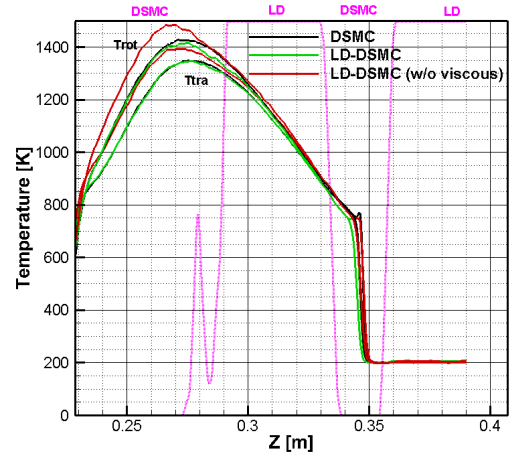

(a) Profiles of temperatures along an extraction line inclined 120° from the freestream direction.

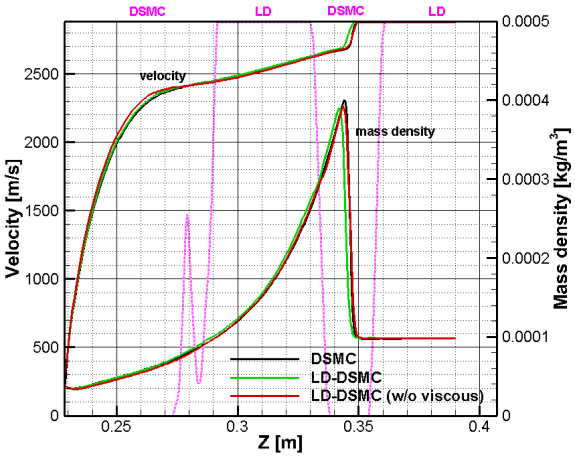

(b) Profiles of bulk velocity and mass density along an extraction line inclined 120° from the freestream direction.

Figure 5.23: Profiles along an extraction line inclined 120° from the freestream direction: black line represents DSMC, green and red lines represent LD-DSMC with and without viscous effects, respectively.

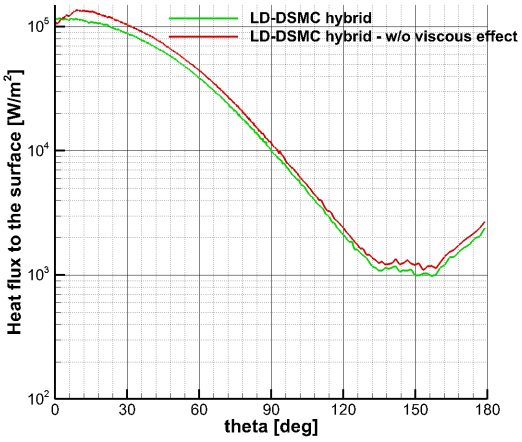

(a) Heat flux to the surface.

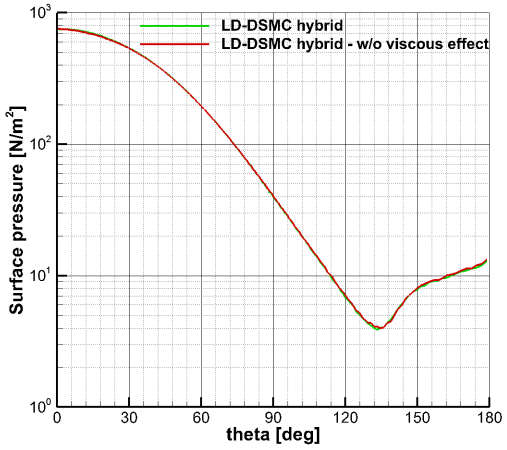

(b) Surface pressure.

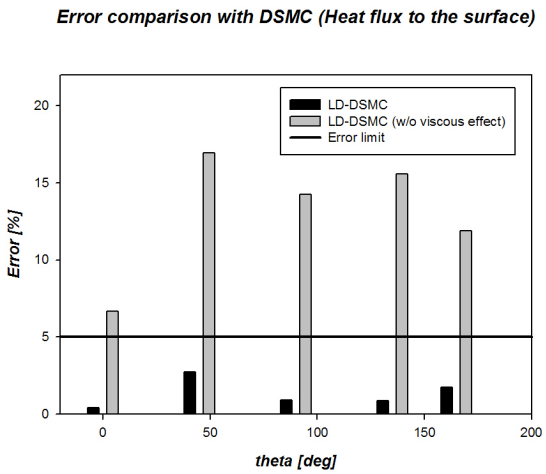

(c) Error comparison of heat flux to the surface

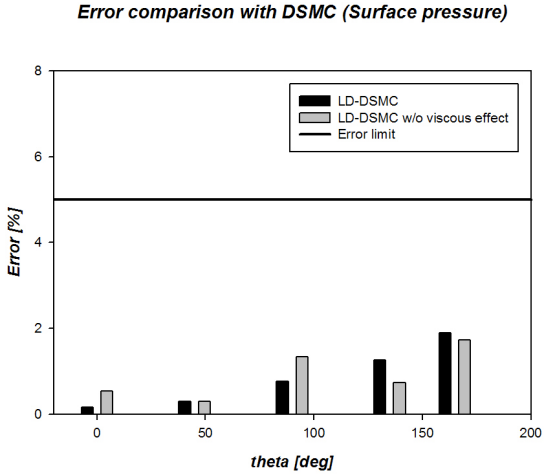

(d) Error comparison of surface pressure

Figure 5.24: Profiles along the sphere surface and error comparisons of LD-DSMC when the viscous effect is not considered in the LD region.

5.1.4 Computational Performance

In Reference [37], the computational performance of the LD-DSMC hybrid method is discussed. The hybrid method does not show any computational expense reduction over simulations performed using standard DSMC on the same mesh. Therefore, the hybrid simulation is performed on a coarser mesh that provides grid independence in the LD calculations, but is considerably less refined than necessary to meet DSMC guidelines to reduce the computational expense. During collision selection routines as part of DSMC calculations, each cell in the DSMC domain is divided into a number of subcells, with subcell dimensions set to approximately half the local mean free path.

A coarser mesh (total number of cells: 234,256) is employed for the hybrid LD-DSMC calculation while a denser mesh (total number of cells: 1,071,858) is employed for the standard DSMC calculation. The enlarged cells do not violate any underlying approximations in the LD method, and can satisfy DSMC guidelines through the use of sub-cells.

Generally, the total number of particles is one of the main factors affecting the computational performance. In DSMC, with an adaptive weight scaling factor, each cell is controlled to have between 20 and 30 particles by updating the weight scaling factor. The total number of particles is 16 M and 73 M for LD-DSMC and DSMC, respectively.

The DSMC and LD-DSMC simulations are considered to have reached steady-state when the total number of simulation particles no longer varies appreciably. In

	Standard DSMC	LD-DSMC hybrid	CFD, slip
Total number of cells	1,071,858	234,256	100,000
Total number of particles	73 M	16 M	
Total CPU hours	1880 hours	1520 hours	320 hours
Relative cost	1	0.8	0.2

Table 5.4: Computational efficiency study of DSMC, LD-DSMC, and CFD for the sphere case

this way, steady state is found to occur after 150,000 time steps and the simulation is then continued to build up a large sample size for an additional 150,000 time steps.

All simulations are performed in parallel on a cluster at the University of Michigan. The LD-DSMC hybrid method shows computational expense reduction over simulations performed using standard DSMC. Total simulation times are approximately 1880 hours for the standard DSMC (Table 5.4). The computational cost of the LD-DSMC simulation is about 1520 hours; this is 20% less than the standard DSMC calculation. CFD requires about one quarter of the cost of LD-DSMC.

5.2 Hypersonic Flow over a Mars Entry Spacecraft

Standard DSMC and the LD-DSMC calculations are performed for carbon-dioxide hypersonic flow over the Mars Pathfinder entry capsule. The purpose of this study is to investigate the numerical sensitivity of the LD-DSMC hybrid simulation. First, the hybrid results are compared with standard DSMC, then, the sensitive numerical factors are discussed.

5.2.1 Flow Conditions and Grid Configurations

The Mars Pathfinder (MPF) configuration and dimensions as used in the current calculations are given in Figure 5.25. The freestream conditions listed in Table 1.1 were generated for a nominal entry trajectory. The atmospheric entry is initiated at 130 km with a relative velocity of 7460 m/s. The degree of rarefaction is expressed in terms of the overall freestream Knudsen number, Kn_∞. The atmosphere of Mars consists of about 95% carbon dioxide, 3% nitrogen, 1.6% argon and contains traces of oxygen and water. The flow is simplified as 100% carbon dioxide and the computations are performed at 65 km altitude where the Knudsen number is 1.96×10^{-3}. The free stream temperature is 137 K, and the free stream velocity is 7450 m/s. Molecular collisions are simulated using the variable hard sphere (VHS) molecular

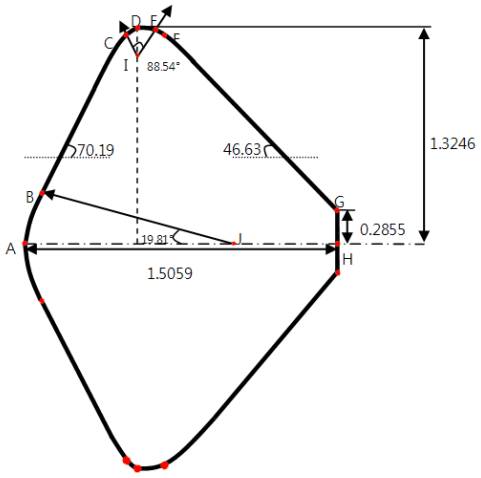

Location	x	y	s
A	0.0000	0.0000	0.0000
B	0.0393	0.2250	0.2295
C	0.4196	1.2808	1.3518
D	0.4820	1.3246	1.4330
E	0.5028	1.3213	1.4541
F	0.5386	1.3094	1.4919
G	1.5059	0.2855	2.9000
H	1.5059	0.0000	3.1859

Figure 5.25: Mars Pathfinder configuration (dimensions in meter) [46].

model [8]. Energy exchange between kinetic and internal modes is controlled by the Larsen-Borgnakke statistical model [10]. The solutions are obtained without chemical reactions and parameters used to define the VHS model are a reference temperature 273 K and a viscosity temperature exponent of 0.93 [8]. The surface boundary conditions assume the gas surface interaction to be diffuse with full thermal accommodation to a specified surface temperature, 1100 K.

The MPF capsule has a 70.1° spherically blunted forebody followed by a 46.6° conical afterbody within a maximum diameter of 2.65 m. Because of Pathfinder's aft center-of-gravity location, it is statically unstable for the free molecular and much of the transitional flow regime, that is, the flow regime bounded by free molecular and continuum flow [46]. The configuration of MPF is detailed in Figure 5.25.

The computational domain for the simulation is extended to a location 3.5m downstream of the nose of the MPF. The computational mesh used to obtain the DSMC solution consists of 815,428 quadrilateral and triangular cells while 205,700 cells are used to obtain the LD-DSMC hybrid solutions. For both DSMC and the LD-DSMC hybrid scheme, a hybrid mesh is used in which a structured grid is employed along the forebody surface while an unstructured grid is used everywhere else in the flow field (Figure 5.26).

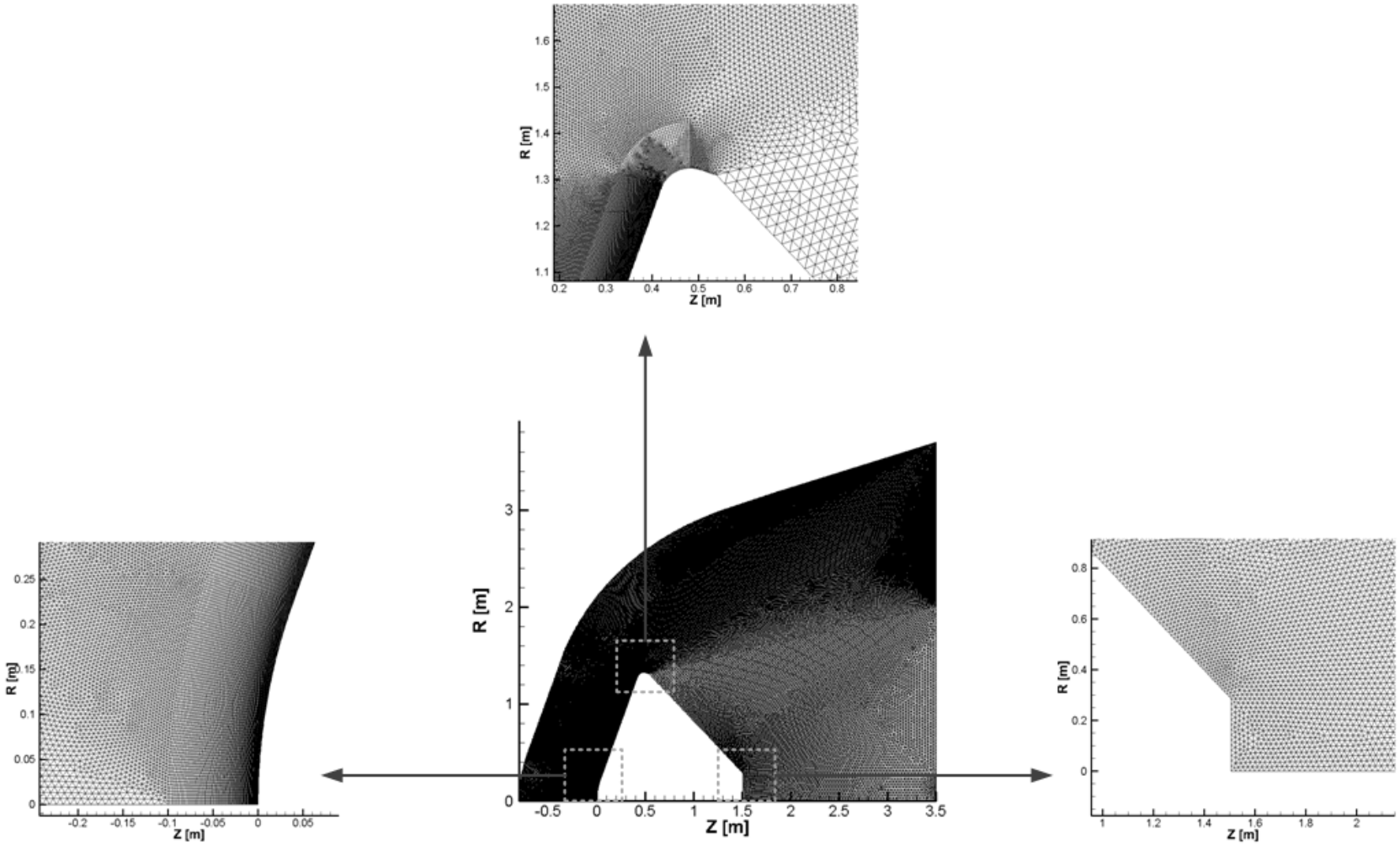

Figure 5.26: Grid configuration over the Mars Pathfinder.

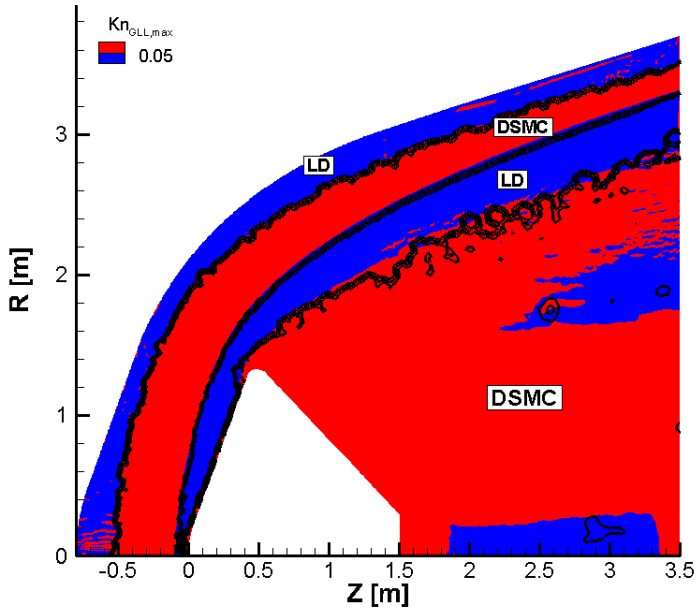

Figure 5.27: Maximum gradient length local Knudsen number, $Kn_{GLL,max}$, and domain decomposition region contours.

5.2.2 Comparing DSMC and LD-DSMC simulations

Figure 5.27 shows the continuum breakdown domain boundaries based on the maximum gradient length Knudsen number, $Kn_{GLL,max}$. The DSMC region is assigned when the $Kn_{GLL,max}$ is larger than the cutoff value of 0.05, while elsewhere is assigned as LD. As expected, the DSMC domain includes the bow shock region and the wake where a high degree of nonequilibrium is observed.

Figure 5.28 shows the velocity and mass density contours from DSMC and LD-DSMC. The upper half is simulated by standard DSMC and lower half is simulated by LD-DSMC. Good agreement is observed, especially in shock standoff distance and shock shapes. Figure 5.29 presents radial profiles for non-dimensional density at three axial locations: location a (Z = 0.4820 m) corresponds to the maximum radial dimension of the probe, location b (Z = 1.0 m) is on the afterbody, and location c (Z = 2.5 m) is in the near wake. Under rarefied flow conditions, the flow in the

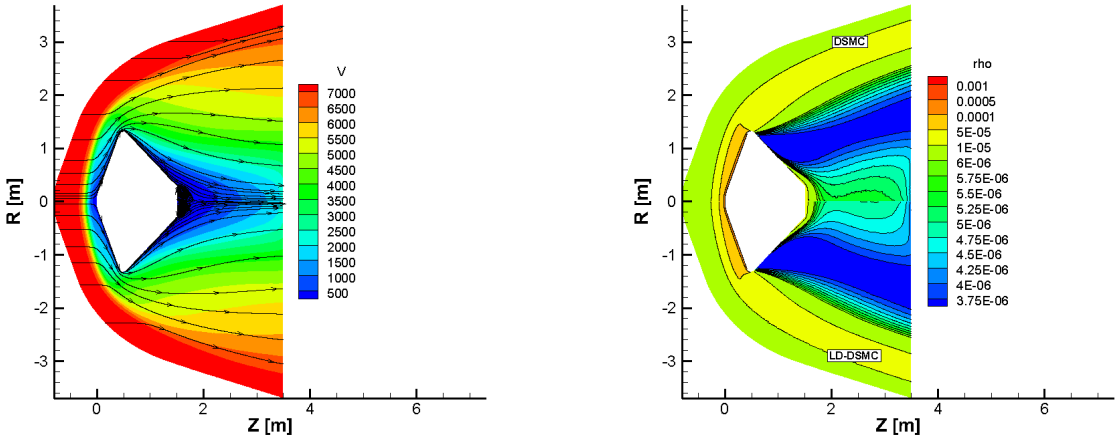

(a) Velocity contours (m/s). (b) Mass density contours (Kg/m^3).

Figure 5.28: Flowfield properties over the Mars Pathfinder.

wake of blunt bodies is even more rarefied than the rest of the flowfield. The impact of rarefaction is observed, for example, the density is generally less than 50% of the freestream value at locations b and c.

Figure 5.30 shows contours of translational and rotational temperature from DSMC and LD-DSMC. Good agreement is observed in the forebody while slight differences are observed in the wake. Comparisons of results for temperature in the wake are shown in Figure 5.31(a). The radial translational temperature profiles show good agreement between the DSMC and LD-DSMC results. The agreement becomes less favorable at location c although it still lies within acceptable errors. Comparisons of translational, rotational, and vibrational temperatures in the wake are shown in Figures 5.31(b) and 5.31(c). It can be seen from these figures that the flow is in a highly thermal-nonequilibrium state. Also, the temperature jump is significant along the afterbody surface.

Figure 5.32 shows profiles of the temperature, bulk velocity and mass density along the stagnation streamline. The vertical dotted lines are the boundaries of the LD and DSMC regions. As expected, the DSMC domain of the hybrid simulation includes

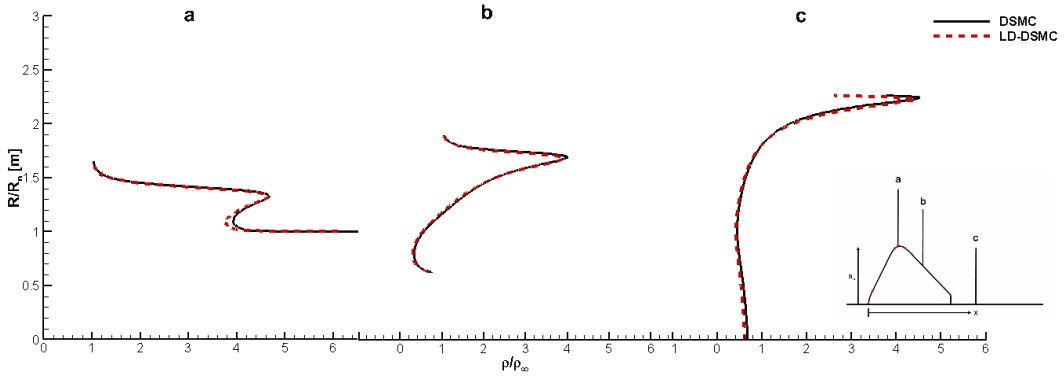

Figure 5.29: Non-dimensional density profiles of DSMC and LD-DSMC results at the wake region.

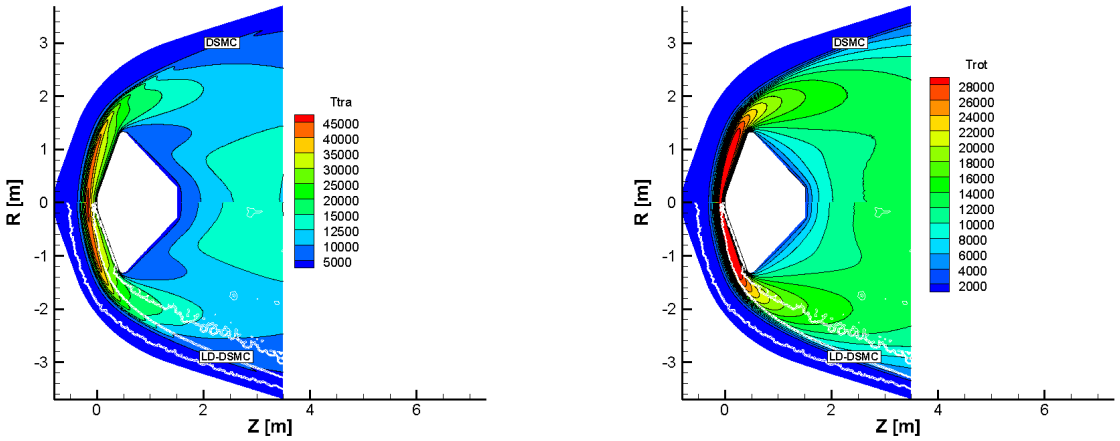

(a) Translational temperature contours.

(b) Rotational temperature contours.

Figure 5.30: Temperature contours [K].

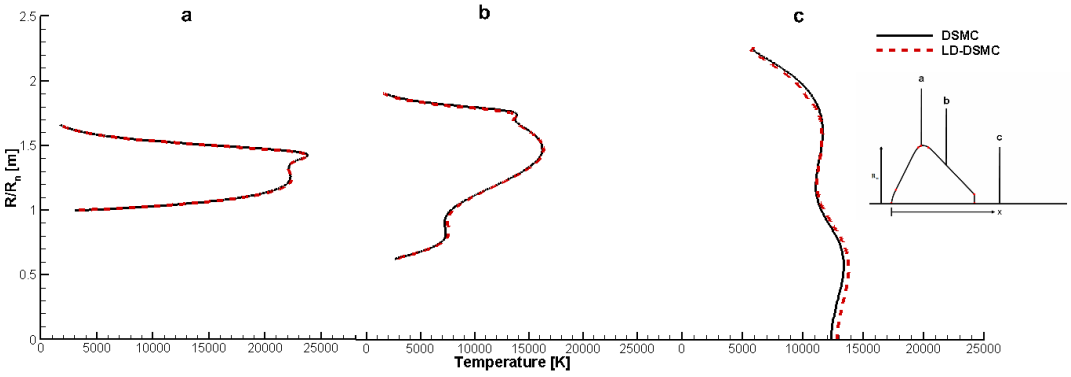

(a) Translational temperature profiles of DSMC and LD-DSMC.

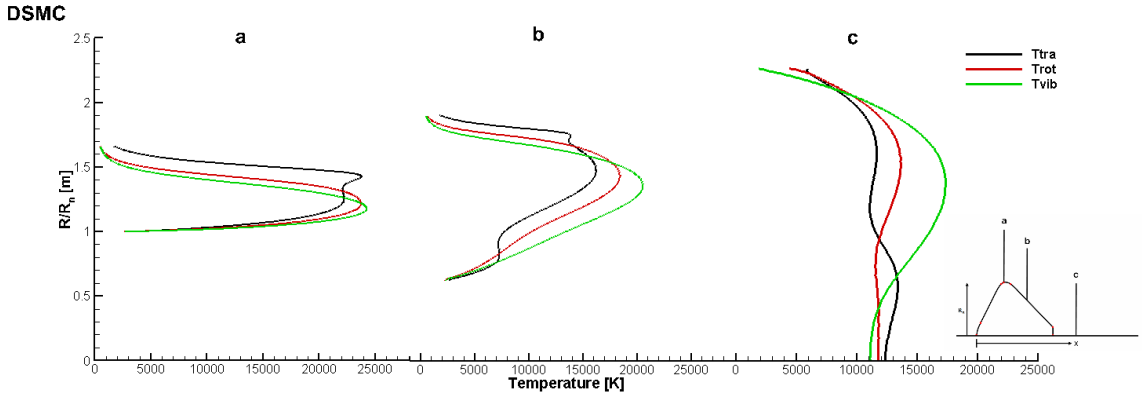

(b) Wake temperature profiles of DSMC.

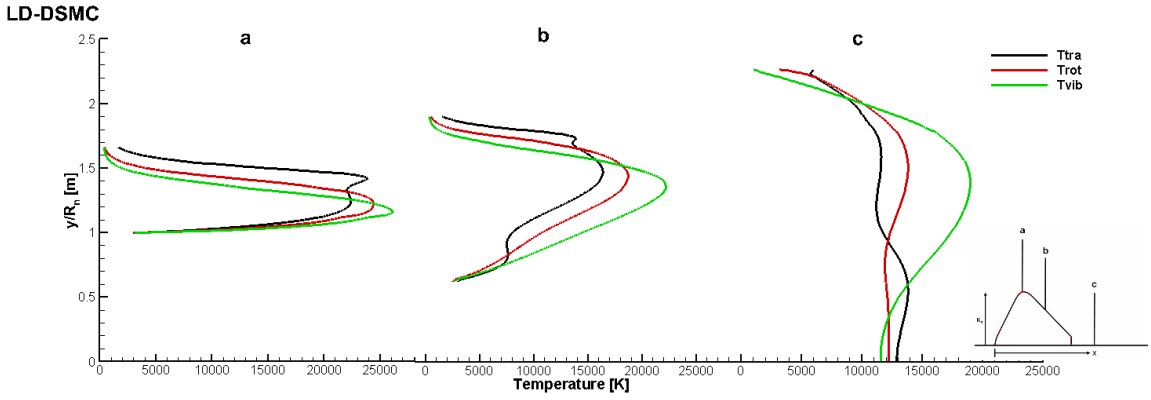

(c) Wake temperature profiles of LD-DSMC.

Figure 5.31: Vertical temperature profiles in the near wake.

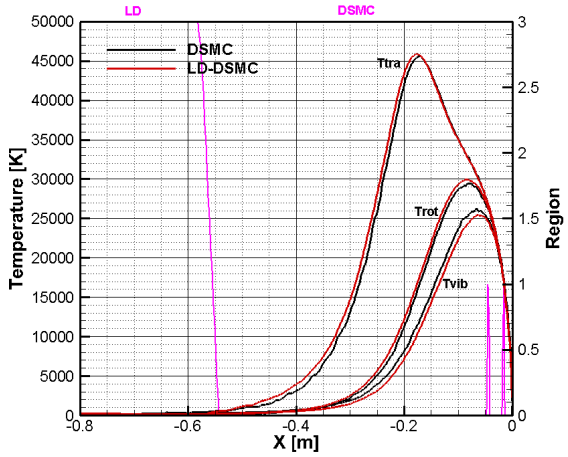

(a) Profiles of temperatures along the stagnation line.

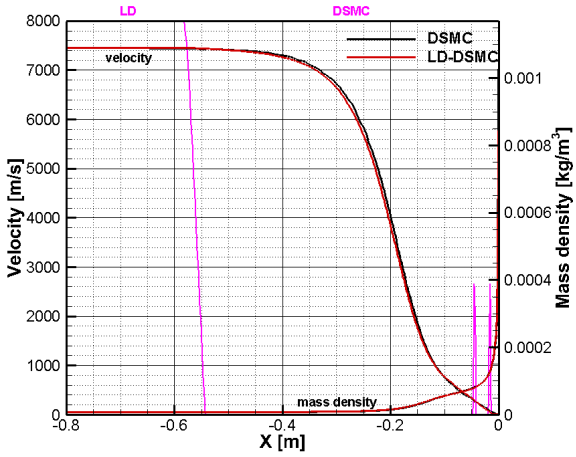

(b) Profiles of bulk velocity and mass density along the stagnation line.

Figure 5.32: Profiles along the stagnation line: black and red lines represent DSMC and LD-DSMC hybrid results, respectively.

high gradient regions within the shock, near the MPF surface, and in the highly rarefied region within the wake. Good agreement is observed in the mass density and bulk velocity while acceptable differences are observed in the temperatures.

Figure 5.33(a) presents profiles of heat flux and pressure along the MPF surface. Both the stagnation-point heating rate and heating rate coefficient, C_H, values are listed in Table 5.5. The heat flux to the surface peaks at 418 kW/m^2 on the forebody, and then decreases down to 4.4 kW/m^2 at the location Z=0.5478 m, which is just beyond location F in Figure 5.25. The aerothermal loads along the afterbody are quite small compared to the forebody. For example, the maximum heating rate adjacent to location D is just 10.8 % of the forebody stagnation point value. Along the afterbody base plane, the maximum heating is near location G, having a value of 1.9 % of the forebody stagnation point value. The surface pressure distribution is shown in the Figure 5.33(b) and both the total drag and total drag coefficient, C_D, values are listed in Table 5.5. The profile is similar to that for the heat flux. It stays at about 400 N/m^2 along the forebody then rapidly decreases to 6 N/m^2 at location F. In

Figure 5.33, good agreement is observed between the DSMC and LD-DSMC profiles within the error limit, 5%. The error is compared at 5 locations in Figure 5.33(c).

	Standard DSMC	LD-DSMC hybrid
q, W/m^2	4.19×10^5	4.13×10^5
C_H	0.255	0.251 (1.57%)
Drag, N	1.97×10^3	1.92×10^3
C_D	1.62	1.58 (2.47%)

Table 5.5: C_H at the stagnation point, and C_D over the Mars Pathfinder.

Table 5.6 shows the computational times of DSMC and LD-DSMC for Mars Pathfinder. All simulations are performed in parallel on 24 processors in a cluster at the University of Michigan. The hybrid simulation is performed on a coarser mesh that provides grid independence in LD calculations, but is considerably less refined than necessary to meet DSMC guidelines. The LD-DSMC hybrid method is a factor of 2 faster than standard DSMC.

	Standard DSMC	LD-DSMC hybrid
Total number of cells	815,428	205,700
Total number of particles	35 M	9 M
Total CPU hours	2283 hours	1128 hours
Relative cost	1	0.5

Table 5.6: Computational efficiency study of DSMC and LD-DSMC for the Mars Pathfinder.

5.2.3 Sensitivity of LD-DSMC to Numerical Parameters

The LD-DSMC hybrid simulation is very sensitive to several numerical parameters. The numerical parameters affecting the LD-DSMC hybrid simulation are classified as (1) relaxation factor for DSMC buffer cell properties, (2) factors which determine the domain size, and (3) Courant number.

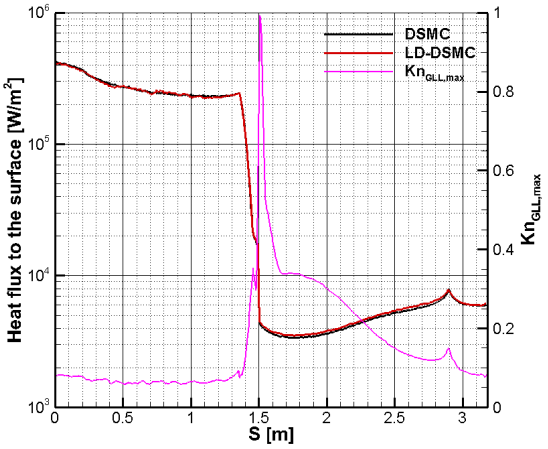

(a) Heat flux to the surface.

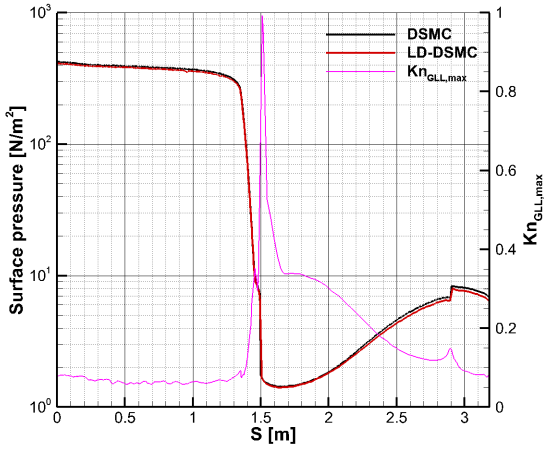

(b) Surface pressure.

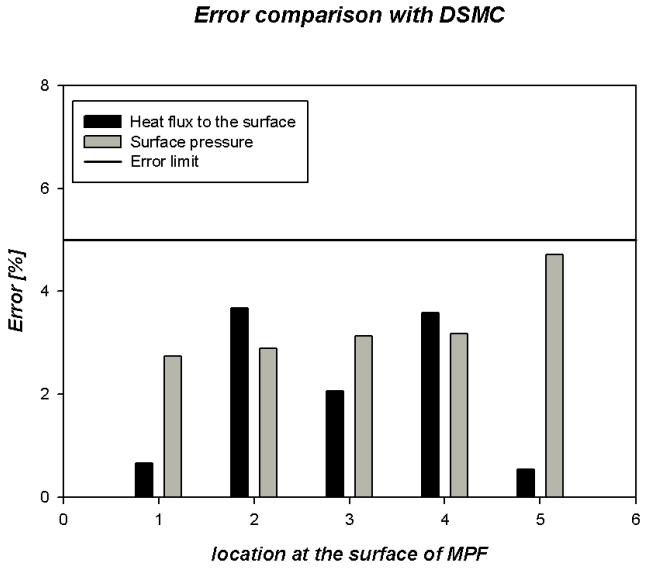

(c) Error comparison of DSMC and LD-DSMC

Figure 5.33: Profiles along the MPF surface.

Relaxation factor for DSMC buffer cell properties

In Chapter 3.2.1, the flow properties in buffer cells are discussed. In Equation (3.5), the relaxation factor, θ, is used for the DSMC buffer cell properties. For larger θ, the time lag in averaged values is reduced, but the scatter associated with instantaneous fluctuations in cell averaged quantities increases. The LD-DSMC hybrid simulation crashes when θ is too large. Usually, a value smaller than 0.01 is used but it needs to be decreased when the flow conditions are severe or the simulation crashes. In the MPF case presented in section 5.2.2, 0.001 is used as the relaxation factor for DSMC buffer cell properties.

Parameters affecting the domain boundaries

Based on $Kn_{GLL,max}$, the LD/DSMC domain boundaries are determined. First, the region where $Kn_{GLL,max}$ is larger than 0.05 is assigned to DSMC, and all other regions are assigned to LD. Then, several iterations of a smoothing procedure are performed. Finally, domain boundaries are determined based on two input parameters: 'number of extra LD cells within the continuum breakdown region' and 'number of extra DSMC cells beyond the continuum breakdown region'. Figure 5.34 shows an example of determining a domain boundary based on continuum breakdown. When the number of extra DSMC cells beyond the continuum breakdown region is 3, and the number of extra LD cells within the continuum breakdown region is 2, the continuum region is extended by 2 cells in all directions and then the DSMC region is extended by 5 cells.

Figure 5.27 shows almost identical contours between predicted continuum breakdown boundaries and the actual domain boundaries. In this simulation, 3 is used for both DSMC and LD extra cells. Meanwhile, Figure 5.2 shows obvious differences between the predicted continuum breakdown boundaries and actual domain bound-

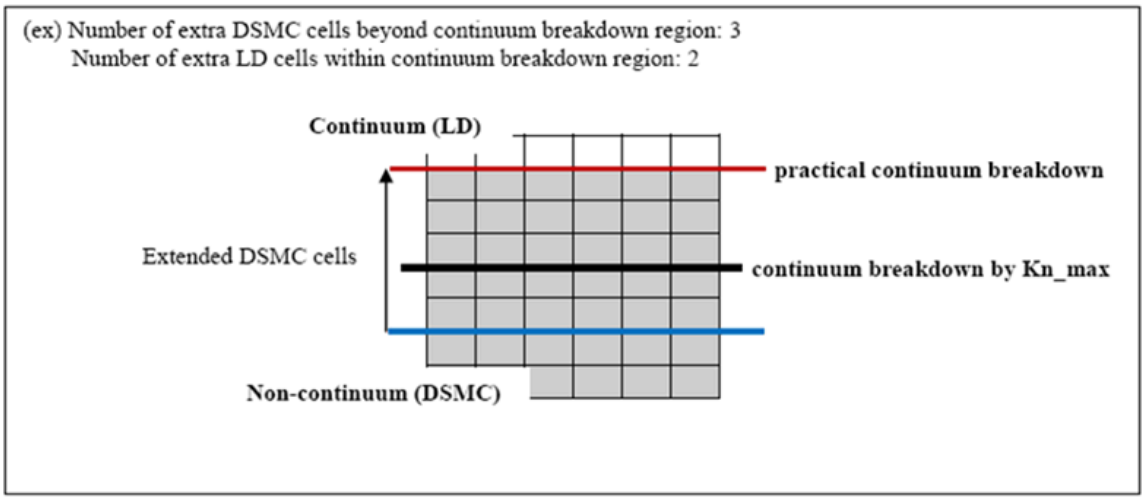

Figure 5.34: Determination of a domain boundary based on the continuum breakdown.

aries. In this simulation, 12 extra DSMC cells and 1 extra LD cells are used. The actual domain boundaries are mainly based on $Kn_{GLL,max}$, but they are also affected by the number of extra DSMC and LD cells.

In a buffer cell, the Kn_{GLL} calculation is used to determine the LD-DSMC domain boundaries based on exponential moving averages for cell-averaged flow quantities like density, bulk velocity, and thermal speed [67]. These values may be influenced by statistical scatter if the relaxation parameter, θ, is not small enough, that may lead to an unphysical increase in the gradients based on these quantities. As Kn_{GLL} values are based on gradients, the ultimate effect of statistical scatter may be to increase Kn_{GLL}. Due to this effect, the required size of the DSMC domain is overestimated at least a little during hybrid calculations.

The time-averaged bulk velocity, density, and thermal speed scale used in these calculations may also be affected by biasing errors, due to the fact that the contribution of instantaneous cell values for a particular time step are not functions of the number of particles in the cell. For example, if there are 10 particles in a cell during one time step, with an average velocity of V_1, and 20 particles in this cell during the

next time step, with an average velocity of V_2, the time-averaged velocity is effectively calculated as $(V1 + V2)/2$, not as $(10 \times V1 + 20 \times V2)/30$.

The magnitude of this overestimate is reduced by reducing the relaxation parameter, θ, involved in time-averaging for determination of bulk velocity, density and thermal speed scale values. It may also be reduced by increasing the number of simulated particles.

Maximum allowable Courant number for LD face operations

To avoid instabilities associated with large time step size in the LD domain, subcycles base on the CFL criterion are used. The number of subcycles is determined based on the CFL numbers in the LD domain cells as:

$$N_{sub} = 1 + \left| \frac{CFL_{LD,max}}{CFL_{allowable,max}} \right| \tag{5.2}$$

where $CFL_{LD,max}$ is defined as:

$$CFL_{LD,max} = \frac{\Delta t}{\Delta x} \times \left[\left\langle \vec{U}_{b,i} \right\rangle + \beta + 5 \frac{1}{\Delta x} \frac{\mu_{cell}}{\beta_{cell}} \right] \tag{5.3}$$

where $\left\langle \vec{U}_{b,i} \right\rangle$ is the cell bulk velocity, β is the most probable thermal speed at equilibrium, μ_{cell} is the dynamic viscosity in the cell, and ρ_{cell} is the mass density in the cell.

Subcycling is used for momentum and energy transport to avoid numerical instabilities. Recall that the net momentum and energy transfer across Lagrangian cell faces is used to reassign particle velocities and temperatures. The maximum allowable Courant number for LD face operations, $CFL_{allowable,max}$, should be smaller than 1. Usually, 0.8 is used but the value must be decreased whenever the LD-DSMC hybrid simulation crashes. For the MPF case, the value must be reduced to 0.2 or smaller.

Maximum allowable CFL number in any cell

For the case which uses adaptive, varying time step size, which is discussed in section 3.4.2, the time step in each LD cell is determined as the maximum allowable CFL number, CFL_{max}. In Figure 3.7, the time step size of the LD cell is determined as:

$$\Delta t = \Delta t_{ref} \times \Delta t^* \times \frac{CFL_{max}}{CFL_{new}} \tag{5.4}$$

where Δt_{ref} is the reference time step, Δt^* is the time step scaling factor, and CFL_{new} is the CFL number for each cell at each time step.

Usually, CFL_{max} is around 0.1, but it needs to be reduced when the simulation crashes. A value of 0.05 is used in the current simulation. For the DSMC type cell, 0.2 is used as maximum ratio of DSMC time step to the mean collision time.

5.3 LD-DSMC Initialized with a Navier-Stokes solution

In Chapter IV, the LD-DSMC hybrid scheme initialized with a Navier-Stokes (NS) solution was discussed. In this Chapter, LD-DSMC initialized with a NS solution is validated by comparing with the conventional LD-DSMC hybrid method. The simulation is performed for nitrogen hypersonic flow over the 12 inch diameter sphere. At the end of the Chapter, computational efficiency is discussed.

5.3.1 Initialization with Navier-Stokes solution

In the DSMC simulation, the most important restriction to decide each cell size is mean free path. The cell size should be smaller than the mean free path. To overcome this strict restriction, subcells and mean collision separation are introduced. If the cell size is larger than the mean free path, it is subdivided into several subcells. This approach improves particle collisions in the cell by promoting nearest neighbor collisions. In this case, the restriction for the DSMC simulation is that the mean

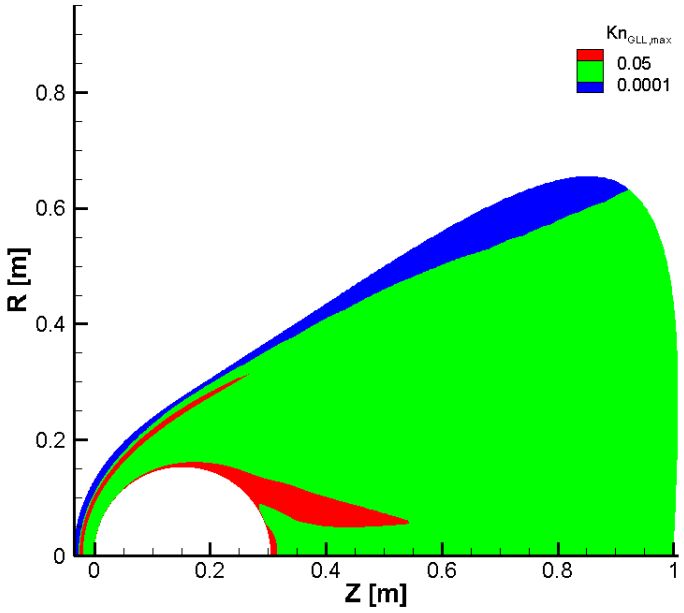

Figure 5.35: Initial domain decomposition based on Navier-Stokes solution.

collision separation should be smaller than the mean free path.

In the LD-DSMC simulation, the cells in the non-continuum region are still restricted by DSMC guidelines, but the cells in the LD region are independent from it. Generally, the mesh for the LD-DSMC hybrid simulation is generated to have slightly larger cells than DSMC cell restrictions to increase computational efficiency. It means several cells may be too large to satisfy DSMC guidelines in the DSMC region, but this problem is alleviated by the subcell utility.

The LD-DSMC hybrid simulation initialized with CFD begins from the CFD solution. Figure 5.35 shows contours of maximum gradient length local Knudsen number, $Kn_{GLL,max}$. The red contour indicates the region where $Kn_{GLL,max}$ is larger than 0.05. That is simulated with DSMC, and the other regions are simulated with LD from the beginning of the simulation. To be used for particle simulation, the initial CFD mesh must be refined, as discussed in section 4.3.

In this simulation, the mesh refinement is performed based on the value of $Kn_{GLL,max}$

Simulation method	Total number of cells
Standard DSMC	1,071,858
LD-DSMC hybrid	234,256
CFD	100,000
LD-DSMC hybrid initialized with CFD	161,221

Table 5.7: Total number of cells according to the simulation method.

of 0.0001. The cells where $Kn_{GLL,max}$ is larger than 0.0001 are refined based on the cell-centered value of mean free path. A maximum refinement factor is restricted to 5 to avoid excessive refinement which may decrease computational efficiency. Figure 5.36 shows the number of refinements of each CFD cell. More refined cells exist along the shock and the wake region. Figure 5.37 shows a final mesh for the LD-DSMC hybrid simulation. Smaller cells are distributed along the shock and the wake region. The total number of cells for various meshes are listed in Table 5.7. The total number of cells for LD-DSMC initialized with CFD is smaller than LD-DSMC because mean free path based refinement helps to avoid large numbers of small cells.

5.3.2 Comparing LD-DSMC and LD-DSMC initialized with CFD

The same flow condition described in section 5.1.1 is used around the 12 inch diameter sphere. Figure 5.38 shows continuum breakdown domain boundaries based on $Kn_{GLL,max}$. As expected, the LD domain includes high-density near-equilibrium regions in the freestream and aftershock regions, whereas the DSMC domain comprises the remaining portions of the bow shock region and the wake. The bow shock dissipates eventually under the rarefied flow condition, and the whole bow shock is not captured in the DSMC region especially far away from the sphere.

Figure 5.39 compares flow properties between LD-DSMC initialized with NS solution and the conventional LD-DSMC hybrid method. The upper half represents the initialization case and the lower half represents standard LD-DSMC. Every property

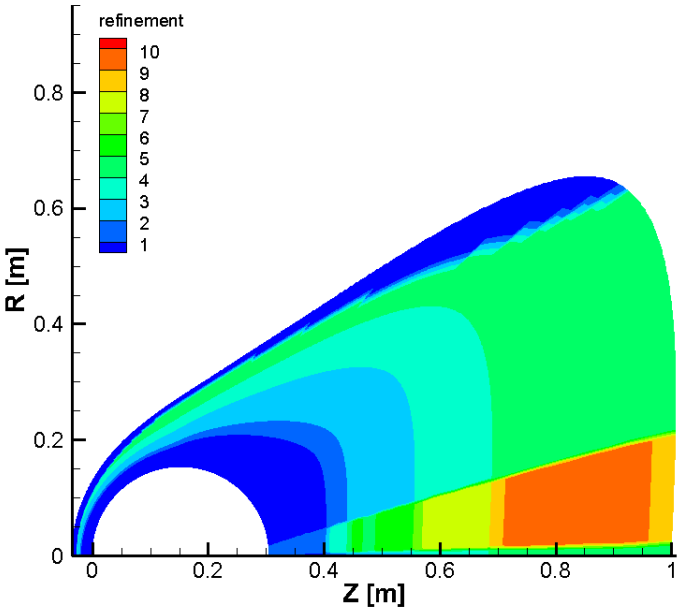

Figure 5.36: Number of refinements of each CFD cell.

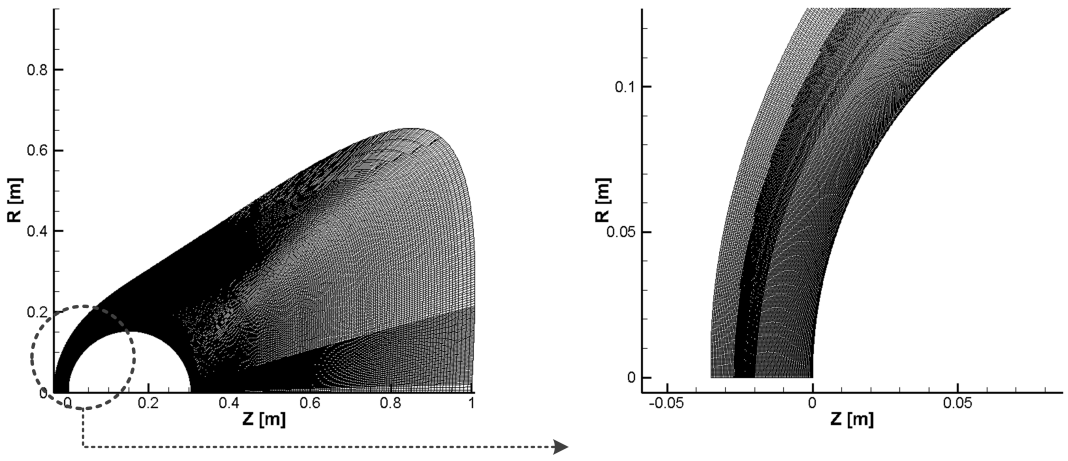

Figure 5.37: Refined mesh based on Navier-Stokes solution.

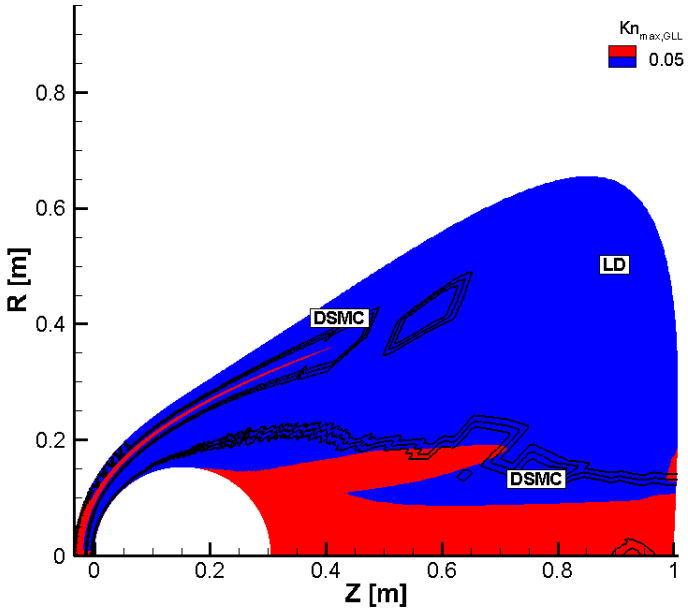

Figure 5.38: Maximum gradient length local Knudsen number and domain decomposition of LD-DSMC initialized with Navier-Stokes solution.

agrees well in the overall flowfield, while rotational temperature contours have a small discrepancy near the sphere shoulder (Figure 5.39(d)).

The flowfield properties are detailed in Figure 5.40 that shows profiles of flow properties along extraction lines inclined at 60° and 120° from the freestream line, respectively. Overall good agreement is observed, while some discrepancy is observed in Figure 5.40(c) in which the translational and rotational temperatures are underestimated near the sphere shoulder.

Figure 5.41 shows profiles along the stagnation streamline. The LD-DSMC hybrid initialized with NS solution case agrees well with the other two simulations. Figures 5.42(a) and 5.42(b) show surface properties. Detailed quantative analysis is provided in Table 5.8 and Figure 5.42(c). Over the entire sphere surface, the error is within the limit of 5% while the error becomes larger in the wake region. Table 5.8 lists peak heating and heat coefficient at the stagnation point, and total drag and

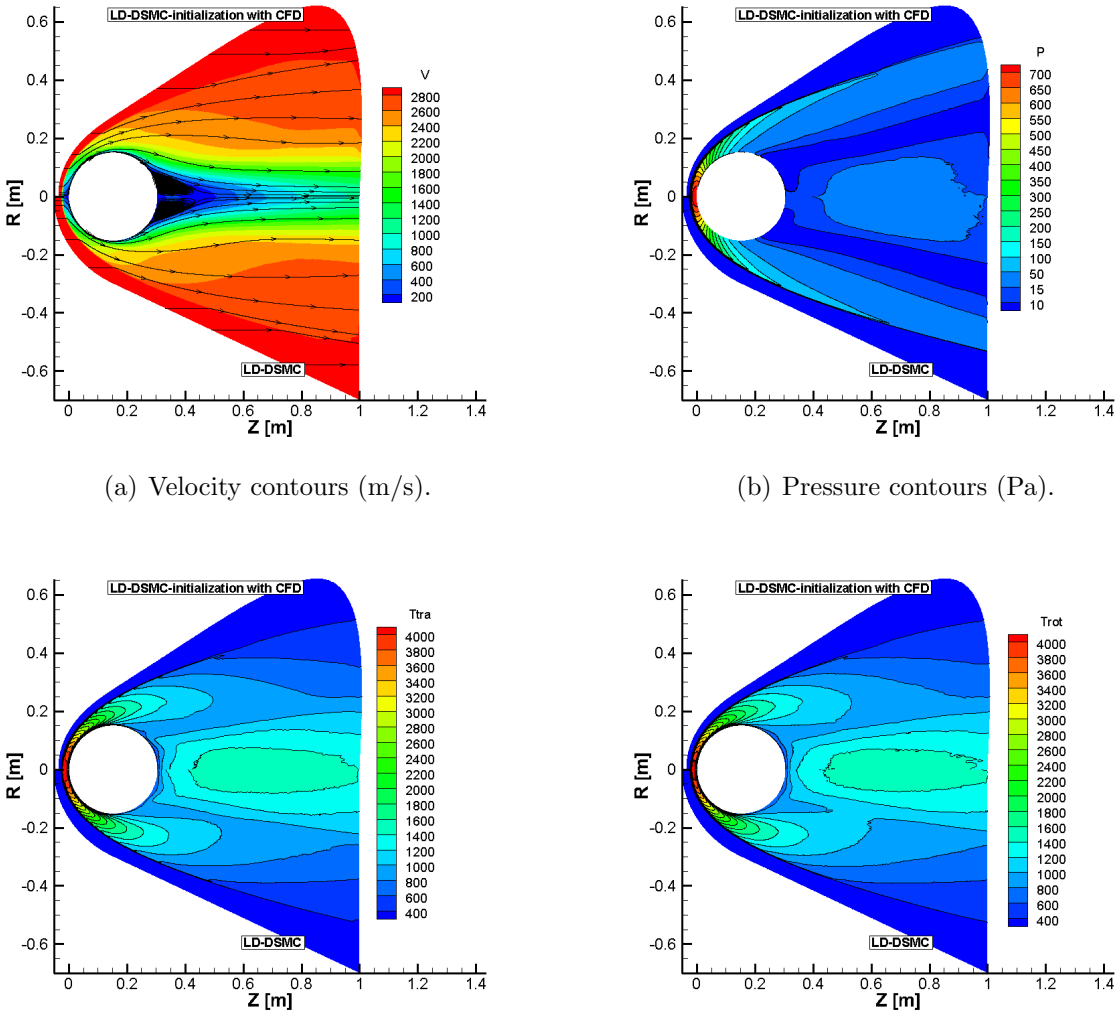

(a) Velocity contours (m/s).

(b) Pressure contours (Pa).

(c) Translational temperature (K).

(d) Rotational temperature (K).

Figure 5.39: Comparing flow properties between LD-DSMC initialized with Navier-Stokes solution (upper) and conventional LD-DSMC (lower).

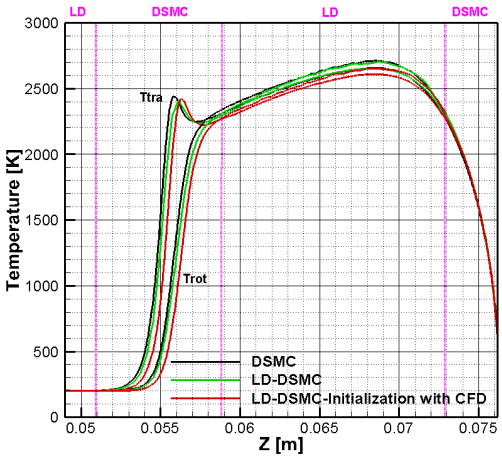

(a) Profiles of temperatures along an extraction line inclined 60° from the freestream direction.

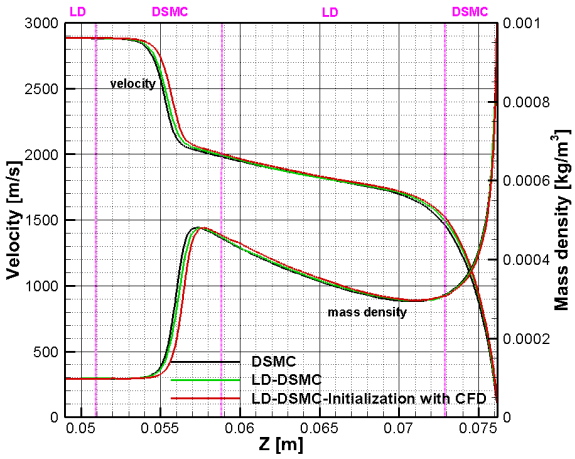

(b) Profiles of bulk velocity and mass density along an extraction line inclined 60° from the freestream direction.

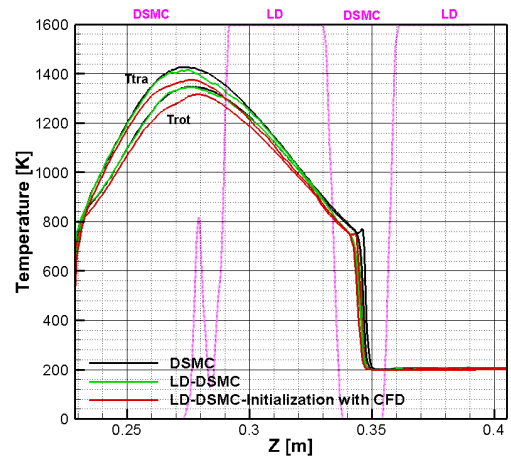

(c) Profiles of temperatures along an extraction line inclined 120° from the freestream direction.

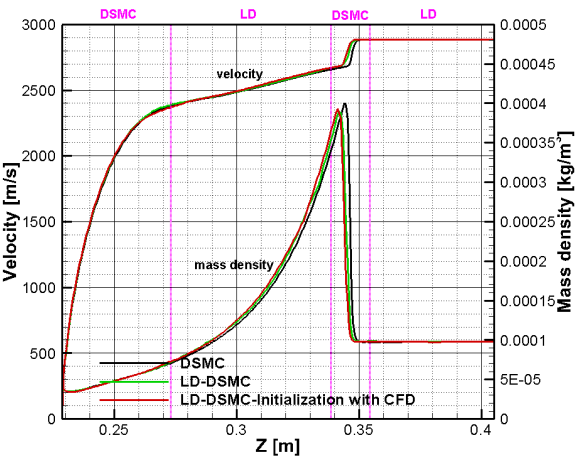

(d) Profiles of bulk velocity and mass density along an extraction line inclined 120° from the freestream direction.

Figure 5.40: Profiles along an extraction line inclined at 60° and 120° from the freestream direction: black and green lines represent standard DSMC and the conventional LD-DSMC hybrid, respectively. Red lines are LD-DSMC hybrid simulation initialized with Navier-Stokes solution.

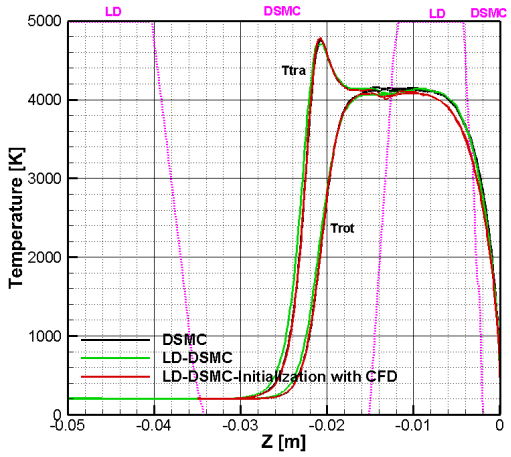

(a) Profiles of temperature along the stagnation line.

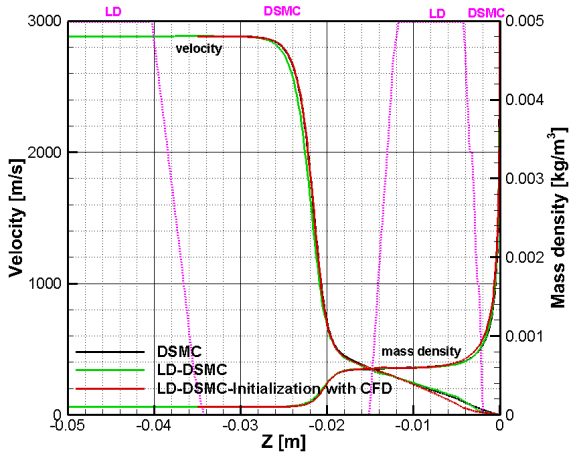

(b) Profiles of bulk velocity and mass density along the stagnation line.

Figure 5.41: Profiles along the stagnation line: black and green lines represent standard DSMC and the conventional LD-DSMC hybrid, respectively. Red lines are the LD-DSMC hybrid simulation initialized with Navier-Stokes solution.

drag coefficient overall the sphere. Again, LD-DSMC initialization with NS solution agree very well within the error limit of 5%.

5.3.3 Computational Performance

The goal of the LD-DSMC hybrid simulation initialized with NS solution is to accurately reproduce the results of the conventional LD-DSMC simulation in less time using less memory. The main advantages of the LD-DSMC hybrid simulation initialized with NS solution comes from the fact that the LD-DSMC hybrid simulation

	Standard DSMC	LD-DSMC hybrid	LD-DSMC hybrid-initialization with CFD
q, W/m^2	115000.0	116000.0 (0.862%)	113000.0 (-1.74%)
C_H	0.0974	0.0976 (0.205%)	0.0955 (-1.95%)
Drag, N	29.0	29.0 (0.00%)	28.6 (-1.38%)
C_D	0.968	0.967 (-0.103%)	0.954 (-1.45%)

Table 5.8: C_H at the stagnation point, and C_D over a surface.

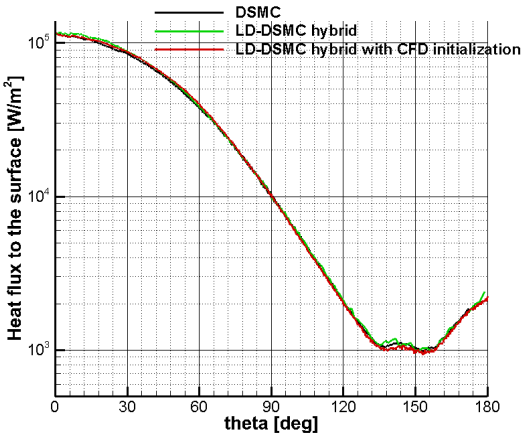

(a) Heat flux to the surface.

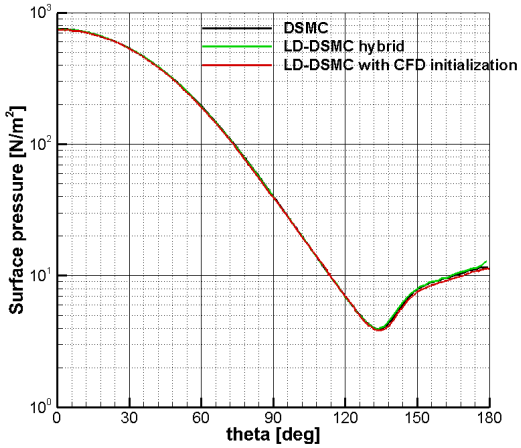

(b) Surface pressure.

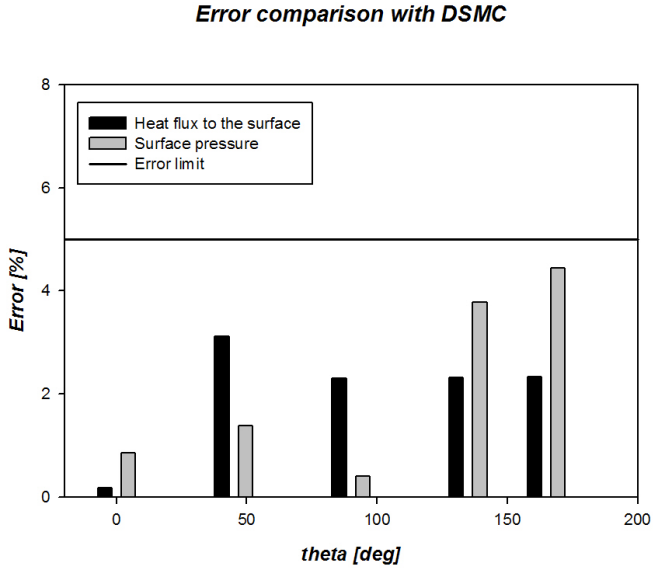

(c) Error comparison of the LD-DSMC hybrid initialized with Navier-Stokes solution with standard DSMC.

Figure 5.42: Profiles along the sphere surface and error comparisons of DSMC, LD-DSMC and LD-DSMC initialized with Navier-Stokes solution.

starts up from the beginning, and from adaptively generated cell size based on the mean free path. Both DSMC and LD-DSMC simulations have two distinct stages: the time required for the flow to reach a steady-state, followed by the time required to sample molecular information to reduce statistical scatter in macroscopic flowfield properties and surface properties. Steady state is reached when the particles have filled the entire computational domain and all flow features have developed to steady state. When the total number of simulation particles levels off and no longer varies, the simulation is considered to have reached steady state. Steady state is found to occur in 150,000 time steps with a reference time step size of 10^{-8} sec. In order to obtain the same level of statistical scatter in the final solution, all simulations are sampled for 150,000 timesteps after reaching steady state.

In Table 5.9, computational efficiencies of the three cases are compared. The total number of cells for LD-DSMC initialized with NS solution is 161,211 and the total number of particles is 9.5 M. The average numbers of particles per cell are 68 and 56 for LD-DSMC and LD-DSMC initialized with NS, respectively. For a fair comparison, an identical average number of particles per cell should be used. However, average number of particles per cell depends on the size of cells and number of subcells. In every simulation, the desired number of particles per cell is set to 30. The reason why the actual average number of particles per cell is larger than 30 is due to the subcell utility. Each subcell has a desired number of particles per subcell (set to 4). If some cells are much larger than mean free path, they may have large number of subcells and a larger number of particles than 30. The computational cost per particle per iteration of LD is 1.19×10^{-6} sec and 2.61×10^{-7} sec for DSMC. The LD method has the largest computation cost per particle per iteration among the methods. This means that the LD method requires more computational expense than DSMC, although it is useful and simple to hybridize with the DSMC method. When the LD-DSMC simulation is initialized with a NS solution, the LD-DSMC hybrid simulation requires 56% of

the cost of the conventional LD-DSMC simulation and less than half of the cost of standard DSMC.

	standard DSMC	LD-DSMC hybrid	LD-DSMC initialized with NS solution
Total number of cells	1,071,858	234,256	161,221
Number of DSMC cells (LD cells)		100,525 (133,731)	101,819 (59,402)
Total simulation particles	73 M	16 M	9.5 M
Computational cost/particle/iteration	2.61×10^{-7}	7.02×10^{-7}	7.30×10^{-7}
Total CPU hours	1880 hours	1520 hours	852 hours
Relative cost	1	0.8	0.45

Table 5.9: Computational efficiency study of standard DSMC, LD-DSMC, and LD-DSMC initialized with a Navier-Stokes solution.

CHAPTER VI

Summary and Conclusion

In this concluding chapter, a summary of the dissertation including major contributions to the field of all-particle multiscale computation of hypersonic rarefied flow as well as recommendations for future research are presented.

6.1 Summary

The present dissertation began with the motivation and introduction to the LD method. In planetary exploration missions, one of the most challenging parts is the EDL sequence including hypersonic entry. The entry vehicle may encounter extreme flow conditions: high velocity and multiscale flow including both high and low Knudsen number. Such multiscale flows can be simulated using a hybrid scheme termed as an 'all particle' hybrid scheme that employs DSMC type particles throughout the whole simulation domain. In this method, a continuum particle method was used as a means for simulation of low Knudsen number gas flow. A large number of representative particles were tracked through a grid in such a way that every particle maintains a constant relative position within a network of Lagrangian cells. Particles followed the macroscopic motion of Lagrangian cells, and moved along trajectories that closely approximate the gas streamlines. Thus, the random particle motion associated with thermal energy was greatly suppressed. The method employed here

significantly reduces both numerical diffusion effects and statistical scatter relative to existing DSMC-based continuum particle methods, and was termed the low diffusion (LD) method.

Chapter II detailed the microscopic level behavior of gas flow. First, the mathematical background of the Boltzmann equation was explained. The difficulties involved in obtaining a deterministic solution to this equation, namely the high dimensionality of the problem, were outlined. Chapter II then discussed two different particle descriptions for equilibrium and nonequilibrium flows; DSMC and LD. The DSMC approach resorted to a statistical description in terms of probability distributions. The LD method is basically similar to the DSMC technique. Both LD and DSMC divided the computational domain into a large number of grid cells and representative particles are tracked through the cells. The main difference between LD and DSMC was in dealing with the particle collisions. Chapter II provided details of the computational approximations, the procedures of each simulation, and the physical models.

The LD-DSMC hybrid method employed the DSMC method in the nonequilibrium region and the LD method in the equilibrium regions. In Chapter III, the various components required by the hybrid LD-DSMC method were completely detailed. The LD-DSMC hybrid method began by calculating the gradient length local Knudsen number, Kn_{GLL}, as an indicator of continuum breakdown to allocate cells to LD and DSMC domains. After assigning LD/DSMC domains, information needed to be transferred across each domain boundary through buffer cells. Chapter III also described the physical models of LD that are consistent with DSMC in order to minimize information loss across the domain boundaries. Viscous modification, models for rotational and vibrational nonequilibrium, and diffusive transport in the LD method were fully detailed. Finally, efforts to increase efficiency of the LD-DSMC hybrid method were described. In the LD-DSMC hybrid simulation, cells in the LD

domain do not need to satisfy the guideline of DSMC that the cell size should be smaller than the mean free path; a subcell utility was introduced to optimize the constraint of DSMC. Numerical weight and time step adaptation may also help to increase computation efficiency.

Prior to this work, the LD-DSMC hybrid method had been initialized with standard DSMC until the first evaluation of continuum breakdown. After the first continuum breakdown, the computational domain was decomposed into LD and DSMC regions, and the hybrid simulation started. The main alternative to hybrid LD-DSMC simulation is CFD-DSMC hybrid simulation that is significantly faster in part because it initialized the method decomposition by evaluating breakdown based on an initial CFD solution. In Chapter IV, a Navier-Stokes solver was introduced to initialize the LD-DSMC hybrid simulation increasing computational efficiency. First, domain decomposition based on $Kn_{GLL,max}$ to classify continuum or non-continuum cells was performed on the initial NS solution. Then, mesh refinement on the DSMC domain was performed to satisfy the DSMC calculation guide line based on the cell-centered value of mean free path. The NS solution also helped to assign effective cell sizes for each LD and DSMC region.

In Chapter V, the above-mentioned LD-DSMC hybrid algorithm was evaluated through its application to hypersonic blunt body flow problems. First, Mach 10 flow of nitrogen about a sphere geometry (where the global Knudsen number was 0.002) was performed. The LD-DSMC hybrid solution was compared to CFD and DSMC solutions. For these hypersonic blunt body flows, $Kn_{GLL,max}$ (using a cutoff value of 0.05) was shown to predict regions of continuum breakdown. This parameter was also shown to provide an accurate prediction for the magnitude of the error in CFD and LD-DSMC solutions compared to the DSMC solution. Comparisons were provided of various flow properties, including a detailed study near the stagnation point where the highest temperature exists. Surface properties were mainly used for

quantitative validations of LD-DSMC with other solutions. The wake region was also investigated to see the rarefaction effects. The viscous effects in the LD region were highlighted through the LD-DSMC hybrid calculation without viscous effect in the LD region. The LD-DSMC hybrid solution agrees well with the standard DSMC solution (within 5% error limit), while significant discrepancies were shown compared to CFD. The LD-DSMC hybrid solution was able to increase computational efficiency by 20% in comparison to DSMC. Then, in Chapter V, the numerical sensitivity of the LD-DSMC hybrid method was investigated through its application to the Mars Pathfinder entry vehicle. The LD-DSMC hybrid solution was very sensitive to several numerical parameters such as the relaxation factor for DSMC buffer cell properties, factors which determine the domain size, and the Courant number in any cell in LD face operations. The importance of these numerical parameters was detailed. Finally, the LD-DSMC hybrid solution initialized with a Navier-Stokes solution was validated by comparing standard DSMC and the conventional LD-DSMC hybrid solution. The initialized solution agreed well with the other two methods and required only 56% of the cost of the conventional LD-DSMC simulation.

6.2 Conclusions and Contributions

The new particle technique, the low diffusion (LD) method, to describe equilibrium gas, and the LD-DSMC hybrid algorithm for analysis of multiscale flow, were originally developed by Burt et al [17, 16]. The LD-DSMC hybrid method allows for very strong coupling between the two flow regimes as well as simpler code development. Then, the LD-DSMC hybrid algorithm was extended to include the viscous modification, internal energy nonequilibrium, and diffusive transport of the LD method for accurate solution [18, 20, 19, 21]. Also, the subcell utility, numerical weight, and time step adaptation were implemented to increase computational efficiency.

The first goal of this dissertation was to validate the accuracy and efficiency of

the LD-DSMC hybrid simulation. LD-DSMC can reproduce full-DSMC at a fraction of the cost. The LD-DSMC hybrid method was applied to two kinds of axisymmetric hypersonic, blunt body flow problems: sphere (Mach 10), and Mars Pathfinder (Mach 40) where the global Knudsen number was 0.002. The method successfully described flow characteristics within 5% errors compared with standard DSMC as a reference. Also, the LD-DSMC hybrid solution showed much higher accuracy than the CFD solution. In addition, the LD-DSMC hybrid method decreased computational cost by up to 50%.

The LD-DSMC hybrid method was found to be highly sensitive to numerical parameters used to assign the LD and DSMC domains with buffer cells along the domain boundary and allowable Courant numbers for cells. Choice of these parameters strongly affects the completion of simulation, simulation performance, and the accuracy of simulation results. The sensitivity of these numerical parameters was investigated in this dissertation and specific values recommended for the first time in the literature.

Unique to this dissertation is the module initializing the LD-DSMC hybrid method with a Navier-Stokes solution. It is used in place of the conventional LD-DSMC hybrid algorithm to increase computational efficiency. Based on the initial CFD solution, $Kn_{GLL,max}$ is used to determine domain regimes, and then mesh refinement is performed to give proper cell size for DSMC and LD calculations in each computational domain.

In conclusion, application to sphere flows and a planetary entry probe problem clearly shows that the LD-DSMC hybrid approach is very promising for the solution of hypersonic steady state flows where a wide range of local Knudsen number is seen. The LD-DSMC hybrid method increased the computational efficiency up to 50% by using the initializing module based on a Navier-Stokes solution.

6.3 Future Research

The best type of application for a hybrid method is a very high-speed, multiscale flow where the DSMC simulation of localized non-equilibrium regions and the LD simulation of localized equilibrium regions are necessary. It is also useful to simulate flows including a wide range of length scale for either mean free path or characteristic length. For example, micro-scale flow within or around MEMS devices, supersonic flow problems for which internal structure of strong shocks is important, and rocket exhaust plumes at high altitude.

By the nature of the high-speed flow, the flow may include chemical reactions. The next step is to implement the physical routines for chemical reactions within the LD-DSMC hybrid code. One of the potential strengths of the LD-DSMC hybrid algorithm is simpler code development, as there is no need to integrate two very different simulation schemes. DSMC already contain the chemical reactions model. Thus, only the procedure for use with standard DSMC routines for chemical reactions requires further research and testing.

The LD-DSMC hybrid simulation has been found to be very sensitive to several numerical parameters that affect the completion of the simulation, solution accuracy, and efficiency of the simulation. Further investigation is needed to make the LD-DSMC hybrid algorithm more robust in terms of numerical parameters. Also, the characteristics of the LD-DSMC solutions should be compared with other all-particle based hybrid simulations to study the strengths and weaknesses.

The NS solution initialization module implemented in the LD-DSMC hybrid method is only validated for an axi-symmetric sphere hypersonic flow. Further hybrid LD-DSMC computations are needed to be performed including various hypersonic blunt bodies. Because the LeMans solution is only available on a structured grid for hypersonic flow, the current version of the refinement module only includes the quadrilateral (structured) cell refinement process. The refinement process should be extended to

triangular cell refinement for the initial CFD solution on unstructured grids. The computational efficiency is mainly influenced by the total number of cells and the total number of particles. Adaptive mesh refinement, which refines the mesh just after continuum breakdown to give optimized cell size for each DSMC and LD domain, should be considered. This may help to increase computational efficiency.

The LD-DSMC hybrid algorithm can be extended for 3D simulations. For hypersonic multiscale flow, 3D DSMC simulations can require a prohibitive number of cells and enormous computational resources because the local cell size should scale with mean free path in each dimension. Such flows provide a good application for a hybrid method. MONACO and MONACO-LD are already implemented for 3D, but the most difficults will likely involve selecting numerical parameters that affect the completion of the simulation, solution accuracy, and efficiency of the simulation.

APPENDICES

APPENDIX A

Species Data

A.1 Variable Hard Sphere Coefficients

Table A.1 lists the coefficients used in the Variable Hard Sphere (VHS) collision models. These coefficients are used to calculate collision probabilities in Bird's No Time Counter (NTC) explained in section 2.2.2.

Species	ω	d_{ref} [m^2]	T_{ref} [K]
N_2	0.74	4.17×10^{-10}	273.
CO_2	0.93	5.62×10^{-10}	273.

Table A.1: Species data for VHS collision models.

A.2 Rotational Relaxation Coefficients

Table A.2 lists the coefficients used in the rotational relaxation models for each species for the rotational collision, shown in Equation (2.11). The variable probability of rotational energy relaxation can match the macroscopic form of the rotational relaxation given by Parker and shown in Equation (A.1) when the energy distribution

of colliding particles can be considered equilibrium [48].

$$Z_{rot} = \frac{Z_{rot}^{\infty}}{1 + \frac{\pi^{3/2}}{2}\left(\frac{T_s}{T_{tra}}\right)^{1/2} + \left(\frac{\pi^2}{4} + \pi\right)\left(\frac{T_s}{T_{tra}}\right)} \tag{A.1}$$

where Z_{rot}^{∞} is the maximum rotational collision number and T_s is the reference temperature for rotational energy exchange model [48].

Species	Z_{rot}^{∞}	T_s [K]
N_2	18.1	91.5
CO_2	0.93	195.0

Table A.2: Species data for rotational relaxation models.

A.3 Vibrational Relaxation Coefficients

Table A.3 lists the coefficients used in the vibrational relaxation models. Experimental investigations by Millikan and White give the following correlation between vibrational relaxation time and temperature [44]:

$$p\tau_v = exp\left(\frac{A_{MW}}{T_{tra}^{1/3}} + B_{MW}\right) \tag{A.2}$$

where p is the pressure, T_{tra} is the translational temperature, A_{MW} and B_{MW} are evaluated from molecular properties as:

$$\begin{aligned} A_{MW} &= 1.16 \times 10^{-3}\mu^{1/2}\theta_v^{4/3} \\ B_{MW} &= -0.015\mu^{1/2}A_{MW} \end{aligned} \tag{A.3}$$

Species	$\theta_v[K]$	A_{MW}	B_{MW}	σ_{PARK} [m^2]
N_2	3395.	220.	13.3	5.81×10^{-21}
CO_2	945.	50.	8.53	5.81×10^{-21}

Table A.3: Species data for vibrational relaxation models.

BIBLIOGRAPHY

BIBLIOGRAPHY

[1] http://solarsystem.nasa.gov/index.cfm.

[2] http://www.nasa.gov.

[3] B.J. Alder and T.E. Wainwright. Studies in Molecular Dynamics. 1. General Method. *Journal of Chemical Physics*, Vol. 31(No. 2):pp. 459–466, 1959.

[4] J.D. Anderson Jr. *Modern Compressible Flow with Historical Perspective*. McGraw-Hill, 1990.

[5] T.J. Bartel, T.M. Sterk, J. Payne, and B. Preppernau. DSMC Simulation of Nozzle Expansion Flow Fields. Colorado Springs, CO, USA, June 1994. presented at the 6th Joint Thermophysics and Heat Transfer Conference.

[6] G.A. Bird. Monte Carlo Simulation of Gas Flows. *Annual Review of Fluid Mechanics*, Vol. 10(No. 1):pp. 11–31, 1978.

[7] G.A. Bird. Monte Carlo Simulation in an Engineering Context. *Progress in Astronautics and Aeronautics*, Vol. 74:pp. 239–255, 1981.

[8] G.A. Bird. *Molecular Gas Dynamics and the Direct Simulation of Gas Flows*. Oxford University Press, 1994.

[9] G.A. Bird. Sophisticated DSMC. Santa Fe, September, 2007. Notes from DSMC07 meeting.

[10] C. Borgnakke and P.S. Larsen. Statistical Collision Model for Monte Carlo Simulation of Polyatomic Gas Mixture. *Journal of Computational Physics*, Vol. 18(No. 4):pp. 405–420, 1975.

[11] I.D. Boyd. Particle Computations of Hypersonic Shock Interaction Flows. Technical report, DTIC Document, 2004.

[12] I.D. Boyd. Direct Simulation Monte Carlo for Atmospheric Entry. 1: Theoretical Basis and Physical Models. *notes for VKI Shortcourse, Nonequilibrium Gas Dynamics: From Physical Models to Hypersonic Flights*, 2008.

[13] I.D. Boyd. Direct Simulation of Rotation and Vibration Nonequilibrium. In *AIAA Paper 1989-1880*, Buffalo, NY, USA, June 1989. presented at 20th AIAA Fluid Dynamics, Plasma Dynamics and Laser Conference.

[14] I.D. Boyd, G. Chen, and G.V. Candler. Predicting Failure of the Continuum Fluid Equations in Transitional Hypersonic Flows. *Physics of fluids*, Vol. 7:pp. 210, 1995.

[15] K.S. Breuer, E.S. Piekos, and D.A. Gonzales. DSMC Simulations of Continuum Flows. In *AIAA Paper 1995-2088*, San Diego, CA, USA, 1995. presented at the 30th AIAA Thermophysics Conference.

[16] J.M. Burt and I.D. Boyd. A Low Diffusion Particle Method for Simulating Compressible Inviscid Flows. *Journal of Computational Physics*, Vol. 227(No. 9):pp. 4653–4670, 2008.

[17] J.M. Burt and I.D. Boyd. A Hybrid Particle Approach for Continuum and Rarefied Flow Simulation. *Journal of Computational Physics*, Vol. 228(No. 2):pp. 460–475, 2009.

[18] J.M. Burt and I.D. Boyd. Extension of a Multiscale Particle Scheme to Near-Equilibrium Viscous Flows. *AIAA Journal*, Vol. 47(No. 6):pp. 1507–1517, 2009.

[19] J.M. Burt and I.D. Boyd. Application of a Multiscale Particle Scheme to High Altitude Rocket Exhaust Flows. In *AIAA 2009-1567*, Orlando, FL, USA, Jan 2009. presented at 47th AIAA ASM.

[20] J.M. Burt and I.D Boyd. A Hybrid Particle Scheme for Simulating Multiscale Gas Flows with Internal Energy Nonequilibrium. In *AIAA Paper 2010-820*, Orlando, FL, USA, Jan 2010. presented at 48th AIAA ASM.

[21] J.M. Burt and I.D. Boyd. Rotational and Vibrational Nonequilibrium in a Low Diffusion Particle Method for Continuum Flow Simulation. In *AIAA Paper 2009-3743*, San Antonio, Texas, USA, June 2009. presented at 41st AIAA Thermophysics Conference.

[22] D.R. Chapman and K.A. Fiscko. Hypersonic Shock Structure with Burnett Terms in the Viscous Stress and Heat Flux. In *AIAA Paper 1988-2733*, volume 1, San Antonio, TX, USA, June 1988. presented at AIAA, Thermophysics, Plasmadynamics and Lasers Conference.

[23] HK Cheng and G. Emanuel. Perspective on Hypersonic Nonequilibrium Flow. *AIAA Journal*, Vol. 33(No. 3):pp. 385–400, 1995.

[24] H.K. Cheng and E.Y. Wong. A Shock-Layer Theory Based on Thirteen-Moment Equations and DSMC Calculations of Rarefied Hypersonic Flows. In *AIAA Paper 1991-0783*, Reno, NV, USA, Jan 1991. presented at 29th AIAA ASM.

[25] S.Y. Chou and D. Baganoff. Kinetic Flux-Vector Splitting for the Navier-Stokes Equations. *Journal of Computational Physics*, Vol. 130(No. 2):pp. 217–230, 1997.

[26] K. Fiscko and D. Chapman, S. Comparison of Burnett, Super-Burnett and Monte Carlo Solutions for Hypersonic Shock Structure. *Rarefied gas dynamics: Theoretical and computational techniques*, Vol. 118:pp. 374–395, 1989.

[27] P.A. Gnoffo. Planetary-Entry Gas Dynamics 1. *Annual Review of Fluid Mechanics*, Vol. 31(No. 1):pp. 459–494, 1999.

[28] T.I. Gombosi. *Gaskinetic Theory*. Number 9. Cambridge Univ Press, 1994.

[29] H. Grad. On the Kinetic Theory of Rarefied Gases. *Communications on Pure and Applied Mathematics*, Vol. 2(No. 4):pp. 331–407, 1949.

[30] H. Grad. The Profile of a Steady Plane Shock Wave. *Communications on Pure and Applied Mathematics*, Vol. 5(No. 3):pp. 257–300, 2006.

[31] B.L. Haas and MA Fallavollita. Flow Resolution and Domain Influence in Rarefied Hypersonic Blunt-Body Flows. *Journal of Thermophysics and Heat Transfer*, Vol. 8(No. 4):pp. 751–757, 1994.

[32] D.B. Hash and H.A. Hassan. Assessment of Schemes for Coupling Monte Carlo and Navier-Stokes Solution Methods. *Journal of Thermophysics and Heat Transfer*, Vol. 10(No. 2):pp. 242–249, 1996.

[33] D.B. Hash and H.A. Hassan. A Hybrid DSMC/Navier-Stokes Solver. In *AIAA Paper 1995-0410*, Reno, NV, USA, Jan. 1995. presented at 33rd AIAA ASM.

[34] D.B. Hash and H.A. Hassan. A Decoupled DSMC/Navier–Stokes Analysis of a Transitional Flow Experiment. In *AIAA Paper 1996-0353*, Reno, NV, USA, Jan 1996. presented at 34th AIAA ASM.

[35] G.S. Hubbard. The Exploration of Mars; Historical Context and Current Results. In *AIAA Paper 2004-3*, Reno, NV, USA, Jan 2004. presented at 42nd AIAA ASM.

[36] M.S. Ivanov and S.F. Gimelshein. Computational Hypersonic Rarefied Flows. *Annual Review of Fluid Mechanics*, Vol. 30(No. 1):pp. 469–505, 1998.

[37] E. Jun, J.M. Burt, and I.D. Boyd. All-Particle Multiscale Computation of Hypersonic Rarefied Flow. In *AIAA Paper 2010-822*, volume 822, Orlando, FL, USA, Jan 2010. presented at 48th AIAA ASM.

[38] V.I. Kolobov, R.R. Arslanbekov, V.V. Aristov, A.A. Frolova, and S.A. Zabelok. Unified Solver for Rarefied and Continuum Flows with Adaptive Mesh and Algorithm Refinement. *Journal of Computational Physics*, Vol. 223(No. 2):pp. 589–608, 2007.

[39] K. Koura and H. Matsumoto. Variable Soft Sphere Molecular Model for Air Species. *Physics of Fluids*, Vol. 4:pp. 1083–1085, 1992.

[40] M.N. Macrossan. The Equilibrium Flux Method for the Calculation of Flows with Non-Equilibrium Chemical Reactions. *Journal of Computational Physics*, Vol. 80(No. 1):pp. 204–231, 1989.

[41] M.N. Macrossan. A Particle-Only Hybrid Method for Near-Continuum Flows. *American Institute of Physics*, Vol. 585:pp. 388–395, 2001.

[42] M.N. Macrossan, M.V. Metchnik, and P.A. Pinto. Hypersonic Flow over a Wedge with a Particle Flux Method. *AIP*, Vol. 762:pp. 650, 2005.

[43] J.B. Marion and S.T. Thornton. *Classical Dynamics of Particles and Systems*. Saunders College Pub., 1995.

[44] R.C. Millikan and D.R. White. Systematics of Vibrational Relaxation. *The Journal of Chemical Physics*, Vol. 39:pp. 3209, 1963.

[45] J.N. Moss, R.C. Blanchard, R.G. Wilmoth, and R.D. Braun. Mars Pathfinder Rarefied Aerodynamics: Computations and Measurements. *Journal of Spacecraft and Rockets*, Vol. 36(No. 3):pp. 330–339, 1999.

[46] J.N. Moss, R.G. Wilmoth, and J.M. Price. DSMC Simulations of Blunt Body Flows for Mars Entries: Mars Pathfinder and Mars Microprobe Capsules. In *AIAA Paper 1997-2508*, Atlanta, GA, USA, 1997. presented at 32nd AIAA Thermophysics Conference.

[47] C. Park. Problems of Rate Chemistry in the Flight Regimes of Aeroassisted Orbital Transfer Vehicles. In *AIAA Paper 1984-1730*, Snowmass, CO, USA, 1984. presented at 19th AIAA Thermophysics Conference.

[48] J.G. Parker. Rotational and Vibrational Relaxation in Diatomic Gases. *Physics of Fluids*, Vol. 2:pp. 449, 1959.

[49] P.S. Prasanth and J.K. Kakkassery. Direct Simulation Monte Carlo (DSMC): A Numerical Method for Transition-Regime Flows–a Review. *Journal of the Indian Institute of Science*, Vol. 86:pp. 169–192, 2006.

[50] D.I. Pullin. Direct Simulation Methods for Compressible Inviscid Ideal-Gas Flow. *Journal of Computational Physics*, Vol. 34(No. 2):pp. 231–244, 1980.

[51] M. Rasmussen, M.L. Rasmussen, and Rasmussen. *Hypersonic Flow*. Wiley, 1994.

[52] J.M. Reese, M.A. Gallis, and D.A. Lockerby. New Directions in Fluid Dynamics: Non-Equilibrium Aerodynamic and Microsystem flows. *Philosophical Transactions of the Royal Society of London*, Vol. 361(No. 1813):pp. 2967–2988, 2003.

[53] R. Roveda, D.B. Goldstein, and P.L. Varghese. Hybrid Euler/Particle Approach for Continuum/Rarefied Flows. *Journal of Spacecraft and Rockets*, Vol. 35(No. 3):pp. 258–265, 1998.

[54] S.S. Sazhin and V.V. Serikov. Rarefied Gas Flows: Hydrodynamic versus Monte Carlo Modelling. *Planetary and Space Science*, Vol. 45(No. 3):pp. 361–368, 1997.

[55] L.C. Scalabrin. *Numerical Simulation of Weakly Ionized Hypersonic Flow over Reentry Capsules*. PhD thesis, The University of Michigan, 2007.

[56] L.C. Scalabrin and I.D. Boyd. Development of an Unstructured Navier-Stokes Solver for Hypersonic Nonequilibrium Aerothermodynamics. In *AIAA Paper 2005-5203*, volume Vol. 5203, Toronto, Ontario, Canada, June 2005. presented at 38th AIAA Thermophysics Conference.

[57] L.C. Scalabrin and I.D. Boyd. Numerical Simulation of Weakly Ionized Hypersonic Flow for Reentry Configurations. In *AIAA Paper 2006-3773*, volume 3773, San Francisco, CA, June 2006. presented at 9th AIAA/ASME Joint Thermophysics and Heat Transfer Conference.

[58] T.E. Schwartzentruber. *A Modular Particle-Continuum Numerical Algorithm for Hypersonic Non-Equilibrium Flows*. PhD thesis, The University of Michigan, 2007.

[59] TE Schwartzentruber and I.D. Boyd. A Hybrid Particle-Continuum Method Applied to Shock Waves. *Journal of Computational Physics*, Vol. 215(No. 2):pp. 402–416, 2006.

[60] T.E. Schwartzentruber, L.C. Scalabrin, and I.D. Boyd. A Modular Particle-Continuum Numerical Method for Hypersonic Non-Equilibrium Gas Flows. *Journal of Computational Physics*, Vol. 225(No. 1):pp. 1159–1174, 2007.

[61] T.E. Schwartzentruber, L.C. Scalabrin, and I.D. Boyd. Hybrid Particle-Continuum Simulations of Non-Equilibrium Hypersonic Blunt Body Flow Fields. In *AIAA Paper 2006-3602*, San Francisco, CA, USA, June 2006. presented at 9th AIAA/ASME Joint Thermophysics and Heat Transfer Conference.

[62] T.E. Schwartzentruber, L.C. Scalabrin, and I.D. Boyd. Hybrid Particle-Continuum Simulations of Low Knudsen Number Hypersonic Flows. In *AIAA Paper 2007-3892*, Miami, FL, USA, June 2007. presented at 39th AIAA Thermophysics Conference.

[63] R.W. Shane, DFG Rault, and RH Tolson. Mars Global Surveyor Aerodynamics for Maneuvers in Martian Atmosphere. In *AIAA Paper 1997-2509*, Atlanta, GA, 1997. presented at 32nd AIAA Thermophysics Conference.

[64] B.D. Shizgal. *Rarefied Gas Dynamics: Experimental Techniques and Physical Systems*, volume 1, pp. 174. AIAA, 1994.

[65] D.A. Spencer, R.C. Blanchard, R.D. Braun, P.H. Kallemeyn, and S.W. Thurman. Mars Pathfinder Entry, Descent, and Landing Reconstruction. *Journal of Spacecraft and Rockets*, Vol. 36(No. 3):pp. 357–366, 1999.

[66] H. Struchtrup. Failures of the burnett and Super-Burnett Equations in Steady State Processes. *Continuum Mechanics and Thermodynamics*, Vol. 17(No. 1):pp. 43–50, 2005.

[67] Q. Sun and I.D. Boyd. Evaluation of Macroscopic Properties in the Direct Simulation Monte Carlo Method. *Journal of Thermophysics and Heat Transfer*, Vol. 19(No. 3):pp. 329–335, 2005.

[68] E.V. Titov, M.I. Zeifman, and D.A. Levin. Application of the Kinetic and Continuum Techniques to the Multi-Scale Flows in MEMS Devices. In *AIAA Paper 2005-1399*, page 2005, Reno, NV, USA, Jan 2005. presented 43rd AIAA ASM.

[69] S. Tiwari and A. Klar. An Adaptive Domain Decomposition Procedure for Boltzmann and Euler Equations. *Journal of Computational and Applied Mathematics*, Vol. 90(No. 2):pp. 223–237, 1998.

[70] W.G. Vincenti and C.H. Kruger. *Introduction to Physical Gas Dynamics*. Krieger Publishing Company, 1965.

[71] D.C. Wadsworth and D.A. Erwin. One-Dimensional Hybrid Continuum/Particle Simulation Approach for Rarefied Hypersonic Flows. In *AIAA Paper 1990-1690*, Seattle, WA, USA, June 1990. presented at 5th AIAA/ASME Joint Thermophysics and Heat Transfer Conference.

[72] W.L. Wang and I.D. Boyd. Predicting Continuum Breakdown in Hypersonic Viscous Flows. *Physics of Fluids*, Vol. 15:pp. 91, 2003.

[73] F.M. White. *Viscous Fluid Flow*. McGraw-Hill, 1991.

[74] C.R. Wilke. A Viscosity Equation for Gas Mixtures. *The Journal of Chemical Physics*, Vol. 18(No. 4):pp. 517, 1950.

[75] H. Xue, Q. Fan, and C. Shu. Prediction of Micro-Channel Flows using Direct Simulation Monte Carlo. *Probabilistic Engineering Mechanics*, Vol. 15(No. 2):pp. 213–219, 2000.

[76] S.M. Yen. Numerical Solution of the Nonlinear Boltzmann Equation for Nonequilibrium Gas Flow Problems. *Annual Review of Fluid Mechanics*, Vol. 16(No. 1):pp. 67–97, 1984.

[77] X. Zhong and G.H. Furumoto. Augmented Burnett-Equation Solutions over Axisymmetric Blunt Bodies in Hypersonic Flow. *Journal of Spacecraft and Rockets*, Vol. 32(No. 4):pp. 588–595, 1995.